PHOTODEGRADATION OF PESTICIDES IN WATER USING METAL DOPED MULTI-COMPONENT HETEROJUNCTION PHOTOCATALYST

By

KGOETLANA CHARLIE MOLOPO

(216038516)

Dissertation in fulfilment of the requirement for the degree

MASTER OF SCIENCE

In

CHEMISTRY

In the

FACULTY OF SCIENCE

of the

UNIVERSITY OF JOHANNESBURG

Supervisor	:	**DR L.N. DLAMINI**
Co-supervisor	:	**DR S.P. MALINGA**

DECLARATION

I hereby declare that this dissertation, which I herewith submit for the research qualification

MASTER OF SCIENCE DEGREE IN CHEMISTRY

to the University of Johannesburg, Department of Applied Chemistry, is, apart from the recognized assistance of my supervisors, my own work and has not previously been submitted by me to another institution to obtain a research diploma or degree.

Mr. Charlie Molopo Kgoetlana　　　　　on this __12__ day of __June 2019____
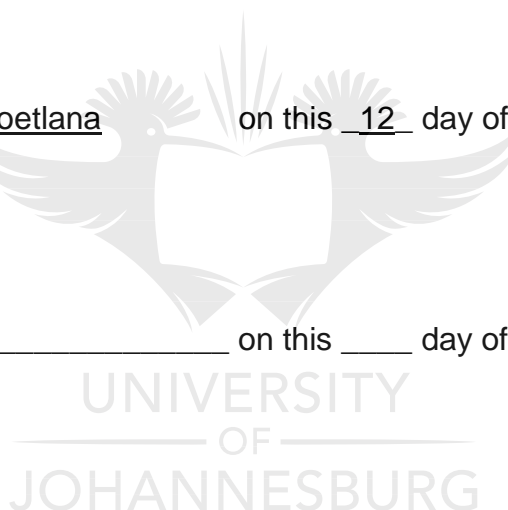　　　*(Candidate)*

_____ on this _____ day of _____
(Supervisor)

_____ on this _____ day of _____
(Co-supervisor)

DEDICATION

This work is dedicated to my mother, Erneth Mothoka Kgoetlana and my Kgoetlana family.

ACKNOWLEDGEMENTS

PUBLICATIONS AND PRESENTATIONS

_____

The work presented in this dissertation has been presented at national and international conferences.

Conferences and symposium presentations

- ❖ <u>C.M. Kgoetlana</u>, S.P. Malinga, L.N. Dlamini. Synthesis and characterization of Mn-doped multi-component WO_3/SnS_2 heterojunction photocatalyst. Oral presentation. 8th International Conference on Pure and Applied Chemistry, Chemistry for a Clean and Healthy Planet (8th ICPAC2018), Sofitel Mauritius L'Imperial Resort and Spa, Mauritius on 2nd – 6th July 2018.

- ❖ <u>C.M. Kgoetlana</u>, S.P. Malinga, L.N. Dlamini. Fabrication of a multicomponent Mn-WO_3/SnS_2 system with the potential of having improved photocatalytic properties. Annual Postgraduate Research Conference, Bunting Road Campus, University of Johannesburg, South Africa, 19 October 2018.

Publications

- ❖ C.M. Kgoetlana, S.P. Malinga, L.N. Dlamini. Fabrication of a multicomponent Mn-WO_3/SnS_2 system with the potential of having improved photocatalytic properties submitted for publication in a peer-reviewed journal.

- ❖ C.M. Kgoetlana, S.P. Malinga, L.N. Dlamini. Photodegradation of chlorpyrifos using Mn-doped Multi-component WO_3/SnS_2 heterojunction photocatalyst in water. Manuscript in preparation for publication in a peer-reviewed journal.

ABSTRACT

For many years now, South Africa has been facing water crisis. Availability of clean water is lacking, and human population increases every year. Available water is contaminated with variety of pollutants such as microbials, organic and inorganic pollutants. This is because of increased industrial and agricultural practices to satisfy the growing population demand.

Organic pollutants are prominent due to high agricultural production whereby pesticides and fertilizers are applied to optimize product output. Pesticides are of huge concern due to their persistence and toxic behaviour in the environment. They are found in rivers and ground water streams after application in the field via run-off or seep into ground.

Chlorpyrifos is an organophosphate pesticide widely used to control pest. Chlorpyrifos has been detected at high levels in water in Western Cape of South Africa. Department of Agriculture in South Africa banned its use as an ingredient in domestic products and pesticides in 2010 but it is still detected in the environment. Chlorpyrifos is an endocrine disrupting chemical, nerve agent and causes dizziness. This pollutant can enter human body by ingestion, dermal adsorption or inhalation. The WHO limit of chlorpyrifos in water is 30 μg/L.

Several methods have been used to remove chlorpyrifos and other pollutants in water such as biological treatment and advanced oxidation processes. Advanced oxidation processes are regarded as safe and efficient pollutant removal, removing a variety of pollutants in water. This is due to utilization of highly reactive species such as hydroxyl and superoxide radicals, known for their rapid and indiscriminative behaviour towards organic compounds resulting in a complete mineralization. Photocatalysis which is a semiconductor-based method emerged as a promising organic pollutant removal method.

Tungsten trioxide (WO_3) has been extensively studied for degradation of heavy metals and organic pollutants. But suffer from photogenerated charge

recombination. To curb that, doping has been used with metal/non-metal dopant and by formation of heterojunction with another semiconductor catalyst to name a few.

In this study, WO_3 was successfully synthesized using a hydrothermal treatment method. It was further modified with Mn^{2+} ion and SnS_2 to improve its photocatalytic activity towards chlorpyrifos degradation by formation of Mn-WO_3/SnS_2. Mn-WO_3/SnS_2 was formed with rectangular shapes confirmed through HRTEM and FESEM. A mixture of monoclinic and hexagonal phases was identified using XRD, Raman and SAED indexing.

The optical and electrochemical properties of Mn-WO_3/SnS_2 were studied using EIS, PL and UV-Vis-DRS. Low emission intensity corresponding to less charge recombination, smaller semi-circle diameter corresponding to less charge transfer impedance and high visible light absorbance wavelength (582 nm) were observed in comparison to those of WO_3 (466 nm), Mn-WO_3 (472 nm), SnS_2 (512 nm) and WO_3/SnS_2 (572 nm).

Mn-WO_3/SnS_2 displayed good stability and increased surface area (77 m^2/g) compared to WO_3 (6 m^2/g). The materials were mesoporous as determined by BET analysis with pore volumes in the range of 0.02 to 0.07. Except SnS_2 which displayed porous adsorbent properties.

The Mn-doped composite (Mn-WO_3/SnS_2) nanoparticles displayed high efficiency for the degradation of chlorpyrifos in synthetic water samples within 60 minutes. UHPLC-MS-MS was used to evaluate the concentration of chlorpyrifos and deduce the degradation pathway. Mn-WO_3/SnS_2 degraded up to 95% chlorpyrifos removal compared to 50, 65, 75, and 85% using WO_3, Mn-WO_3, SnS_2 and WO_3/SnS_2 respectively.

After optimization of conditions such as pH, initial chlorpyrifos concentration and initial photocatalyst loading, 100% chlorpyrifos removal was achieved at pH 7, 1 g of nanoparticles and 1000 ppb of chlorpyrifos concentration. The complete degradation of chlorpyrifos and its major degradation by-product TCP was achieved.

TCP was completely degraded to innocuous materials. Kinetic studies were deduced to a second order reaction at 209×10^{-3} $M^{-1}s^{-1}$.

TABLE OF CONTENTS

LIST OF FIGURES

LIST OF TABLES

LIST OF ABBREVIATIONS

AC	Alternating current
AOPs	Advanced oxidation processes
APCI	Atmospheric pressure chemical ionization
APPI	Atmospheric pressure photo-ionization
BET	Brunauer-Emmett-Teller
CB	Conduction band
CCD	Charge-coupled device
CNTs	Carbon nanotubes
COD	Chemical oxygen demand
CPF	Chlorpyrifos
DC	Direct current
DDT	Dichlorodiphenyl trichloroethane
DI	Deionized water
DRS	Diffuse reflectance spectroscopy
DSSCs	Dye-sensitized solar cells
E. coli	Escherichia coli
EDS	Energy dispersive x-ray spectroscopy
E_g	Electronic band gap energy
EIS	Electrochemical impedance spectroscopy
ELS	Electrophoretic light scattering
ESI	Electrospray ionization
ETL	Electron transport later
FESEM	Field emission scanning electron microscope

FRA	Frequency response analyzers
FTIR	Fourier transform infrared
FWHM	Full width half maximum
HRTEM	High resolution transmission electron microscope
IQ	Intelligent quotient
IR	Infrared
IS	Impedance spectroscopy
LC-MS	Liquid chromatography-mass spectroscopy
LSV	Linear sweep voltammetry
MRM	Multiple reaction monitoring
MS	Mass spectroscopy
NHE	Normal hydrogen potential
NPs	Nanoparticles
OPs	Organophosphate pesticides
PAHs	Polycyclic aromatic hydrocarbons
PBDEs	Polycyclic brominated
PCBs	Polychlorinated biphenyls
PECs	Power conversion efficiencies
PEG	Polyethylene glycol
pH	Potential hydrogen
PL	Photoluminescence
POPs	Persistent organic pollutants
Ppb	Parts per billion
PRINT	Particle replication in non-wetting templates

PS	Photosensitizer
PZC	Point of zero charge
QC	Quantum confinement
SAED	Surface area electron diffraction
STP	Standard temperature and pressure
TCP	3,5,6-trichloro-2-pyridinol
TGA	Thermo-gravimetric analysis
TOF	Time-of-flight
UV	Ultraviolet
UV-Vis	Ultraviolet-visible
VB	Valence band
V_{fb}	Flat-band potential
VOCs	Volatile organic compounds
XRD	X-ray diffraction
XPS	X-ray photoelectron spectroscopy
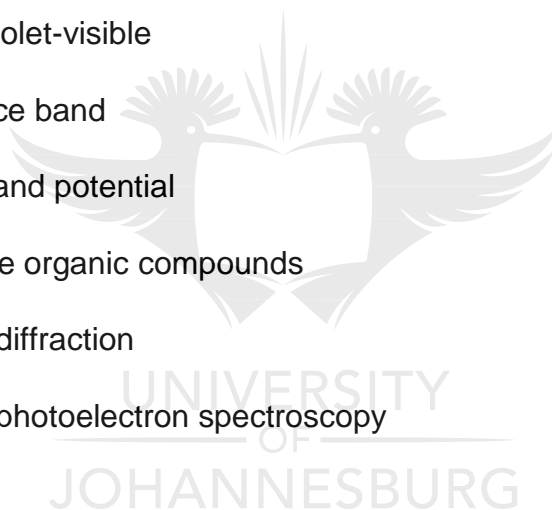
CHAPTER 1

INTRODUCTION

1.1   Problem statement

Industrial and agricultural activities are one of the main sources of water contamination globally (Yang 2014). Industries dump waste directly or indirectly into the rivers or landfills. Industrial activities include the production of chemical compounds such as pesticides, salts and dye. Agricultural activities include the use of fertilizers, pesticides and insecticides to improve crop production.

These chemicals may end up in the water streams via run-off or gets absorbed into the land seeping into underground aquifers. Most pesticides are organic and their degradation in the environment is not possible using normal conventional methods. These pesticides are persist in the environment (soil and water) and upon consumption they bioaccumulate in the ecosystem especially living cells causing toxicity (Ndlovu et al. 2014; Alharbi et al. 2018).

As a result, the exposure of pesticides led to respiratory health problems, increased ocular nasal and elevated asthma symptoms amongst women farm workers in Western Cape of South Africa (Ndlovu et al. 2014). Furthermore, in rural areas, 17.9% of males working in crop spraying in Cape Town were reported to have chronic organophosphate poisoning, leading to asthma, and chronic bronchitis (Ndlovu et al. 2014).

Persistent organic pollutants (POPs) such as polychlorinated biphenyls (PCBs), dichlorodiphenyl trichloroethane (DDT) and organophosphate pesticides (OPs) (such as aldrin, dieldrin, chlorpyrifos)(Affairs 2011) has been widely used in pests and

disease control, crop production and industries (Alharbi et al. 2018; Lockwood 2017; Dalvie et al. 2006).

Due to their persistence in the environment and bioaccumulation in the fatty tissues of animals, their effects on exposure, is either acute or chronic. The adverse effects of these compounds often lead to allergic reactions, the disruption of the endocrine system, cancer and subsequently to death (Kuo et al. 2009).

Figure 1.1 shows estimated average annual use of atrazine in different crops throughout South Africa, this is to indicate the amount of pesticides used in our agricultural production which consequently pollute our water systems. The provinces with the highest atrazine level used includes Mpumalanga, North West, Free State, Limpopo and Kwa-Zulu Natal (Dabrowski, 2015).
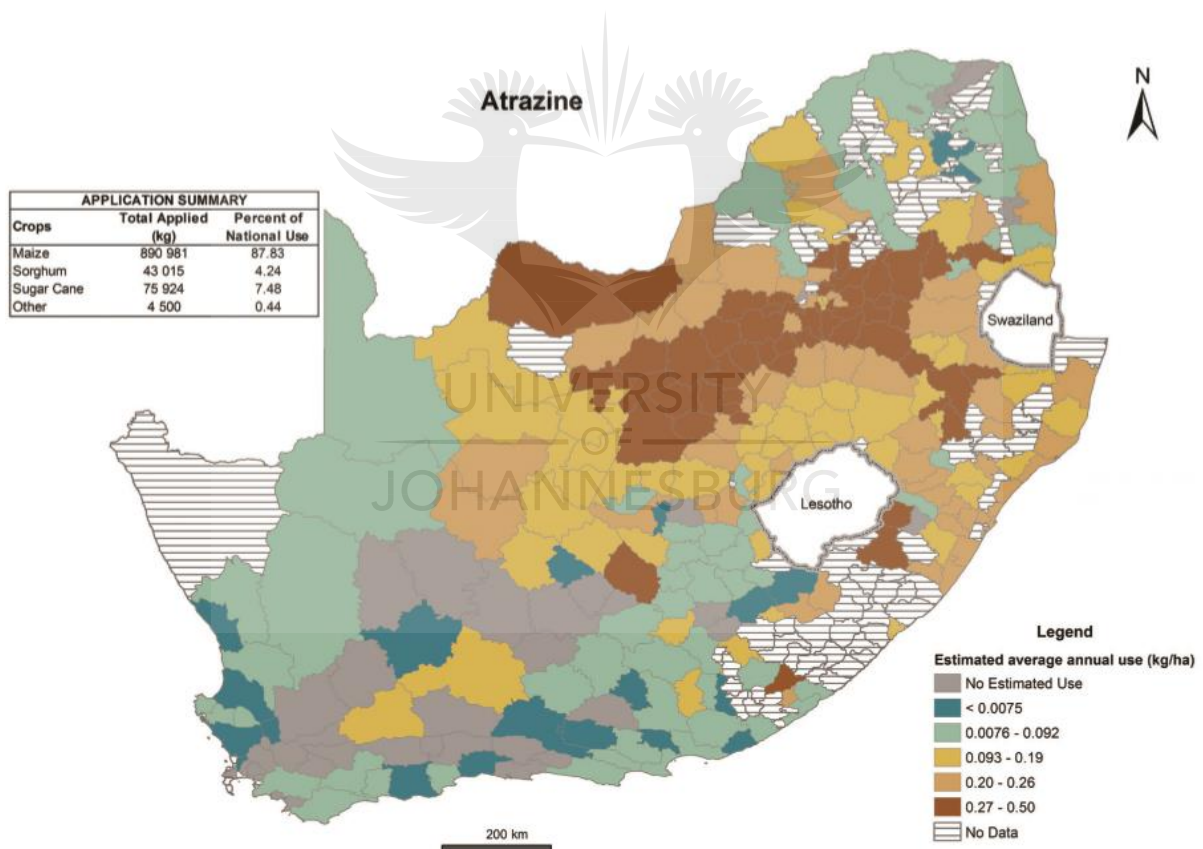
Figure 1.1: Map showing the average annual use of atrazine per hectare of agricultural land in magisterial districts of South Africa for the year 2009, estimated from pesticide sales and agricultural crop census data (Dabrowski, 2015).

A survey conducted in South Africa by Dalvie and co-workers (2006) on mapping the prevalence of pesticides "hot-spots" in the country, showed that the Western Cape Province had the highest pesticide levels (Dalvie et al. 2006). 40 establishments in the rural areas were found containing 9 tons of unwanted pesticides with different active ingredients. The active ingredients include 127.3 kg of DDT, 151 kg of and 141 kg of chlorpyrifos. Consequently, the residents in the rural areas of the Western Cape got exposed occasionally to the pesticides through contaminated food, soil and water (Dalvie et al. 2006).

Pesticides were detected in surface and ground water from Western Cape in South Africa, especially chlorpyrifos (rainfall induced run-off sample = 0.19 g/L, sediments = 245 g/kg) and endosulfan (rainfall induced run-off sample = 0.35 g/L, sediments = 273g/kg) (Dabrowski et al. 2001; Dalvie et al. 2009). A study by Dalvie & London (2009) indicated that there were high levels of mercaptothion (1.95 mg/kg), permethrin (0.448 mg/kg) and chlorpyrifos (0.08 mg/kg) pesticides in South African raw wheat and raw wheat imported from other countries compared to EU, WHO and SANS permissible levels (Dalvie & London 2009). The acceptable limit for chlorpyrifos in drinking water is 30 µg/L (WHO 2004).

Chlorpyrifos is one of the organophosphates that has a wide spectrum use for pest control in the agricultural practices and at homes for lawns (Ruan et al. 2012). It can be found in water bodies after it has been applied and washed into the water from the agricultural sector. Humans can be exposed to chlorpyrifos through consumption of chlorpyrifos contaminated water, food and soil.

Children are most likely to get affected by this pesticide due to its high affinity to colloidal matter. Health effects related to chlorpyrifos are neurotoxicity, cholinesterase inhibitor and imparts on the reproductive system of male (Meeker et al. 2004).

The conventional water and wastewater treatment methods that are currently employed such as coagulation and chlorination are failing to degrade organic pollutants in water and wastewater. Because these pollutants are present in small quantities and the conventional methods cannot remove pollutants in minute

concentrations, therefore leading to unsafe water for drinking. These pollutants are being detected in the effluent of the treated wastewater, therefore posing health threat to human beings and other animals due to their toxicity.

1.2   Justification

Due to continued wide application of pesticides in the agricultural sector to control pest and to increase production yield. These chemicals continue to prevail in the rivers, soil and air due to their persistence (Alharbi et al. 2018). Therefore find their way into human and animal bodies whereby they cause neurotoxicity and can lead to death (Kuo et al. 2009).

Advanced oxidation processes (AOPs) have recently been applied for decomposition of organic pollutants (Quiroz et al. 2011). The AOPs includes Fenton reactions, dye sensitizers and photocatalysis (Samet et al. 2012). These AOPs use active oxygen species such as hydroxyl and superoxide radical as their main powerful oxidizing agent.

Photocatalysis is a promising tool for the degradation of organic pollutants. There are many photocatalysts that have been used to degrade organic compounds as single catalyst or as a heterojunction to another catalyst or non-metal. These include TiO_2, ZnO, Fe_2O_3, CdS, GaI, WO_3, SnS_2 and ZnS and are known as semiconductor photocatalyst (Teoh et al. 2012; Xu et al. 2014).

These photocatalysts were associated with high efficiency in degradation of a wide variety of organic pollutants into biodegradable compounds or less toxic molecules, therefore mineralizing them into non-poisonous CO_2 and H_2O (Ayoub et al. 2010; Du et al. 2011). This was alluded to their smaller size which makes them easy to interact with low organic pollutant concentrations.

Tungsten trioxide (WO_3) nanoparticles are visible light absorbing, stable in aqueous environments under different pH conditions and can be applied in variety of

applications such as gas sensing and photoelectrocatalytic decomposition of organic pollutants.

The decomposition of organic pollutants using WO_3 nanoparticles is due to its more positive potential than the H_2O/O_2 oxidation potential ($E_0(O_2/HO_2\bullet)=0.05V$ vs NHE) which enable the production of hydroxyl radical for oxidation of organic pollutants (Baalousha et al. 2008). The pristine WO_3 suffer from high photogenerated charge recombination rate leading to reduced photoactivity. To mitigate the high recombination rate, methods such as doping, photosensitization and formation of heterojunction are used. Therefore, this project thus aimed to use doping ($Mn-WO_3$) and formation of heterojunction ($Mn-WO_3/SnS_2$) to degrade organophosphate pollutant (chlorpyrifos). The formed heterojunction will have high charge separation due to electron trapping by Mn ion and formation of interface between WO_3 and SnS_2 to allow easy movement of photogenerated charges throughout the composite.

1.3   Aim

To synthesize highly effective composite Mn-doped WO_3/SnS_2 nanoparticles for efficient photocatalytic degradation of chlorpyrifos and its major degradation by product in water.

1.4   Objectives:

- ➢ To synthesize WO_3, SnS_2, $Mn-WO_3$, WO_3/SnS_2 and Mn-doped WO_3/SnS_2 nanoparticles via a hydrothermal method.

- ➢ To characterize the as-synthesized nanoparticles using X-Ray diffractometer (XRD), High Resolution Transmission Electron Microscopy (HR-TEM), Field Emission Scanning Electron Microscopy (FE-SEM), Brunauer-Emmett-Teller (BET), Raman Spectroscopy, Photoluminescence spectroscopy (PL), Fourier transform infrared spectroscopy (FTIR), Thermogravimetric analysis (TGA), Ultraviolet-Visible spectroscopy (UV-Vis)-Diffuse Reflectance spectroscopy (DRS) and Electrochemical Impedance Spectroscopy (EIS).

- ➢ To study the photodegradation by-products of chlorpyrifos using hyphenated

analytical technique such as LC-MS/MS.

➢ To understand the kinetics and mechanistic degradative pathways of chlorpyrifos.

1.5   Dissertation outline

This work is outlined in the following pattern:

Chapter 1 introduces the reader to the topic with a set of problems that will be addressed, how they are going to be addressed and to state why the study was conducted.

Chapter 2 reviews the relevant literature related to the work documented in this dissertation on the development and applicability of nanomaterials to degrade pollutants. It also discusses the theory of the characterization and analytical techniques used in this project.

Chapter 3 states the materials/resources used and the detailed procedure of how the research was conducted from synthesis of materials, to characterization of material instrument settings and photocatalytic application.

Chapter 4 illustrates the attained results of the conducted research on the synthesis and characterization of the nanomaterials, trends and developments explained, supported by relevant theories and backed up by other literature findings.

Chapter 5 displays and discusses the efficiency of the nanoparticles when applied for the degradation of chlorpyrifos in water and deduced mechanistic pathway.

Chapter 6 draws conclusion based on the results and discussions obtained in chapter 4 and 5, it further points out the gaps identified during the study for future work.

Appendices displays the additional data obtained during the study.

1.6   References

Affairs, D. 2011. Western Cape IWRM Action Plan: Status Quo Report. *Western Cape IWRM Action Plan: Status Quo Report*, (c), pp.186–209.

Alharbi, O. M. L., Basheer, A. A., Khattab, R. A. & Ali, I. 2018. Health and environmental effects of persistent organic pollutants. *Journal of Molecular Liquids*, 263(2018), pp.442–453.

Ayoub, K., Hullebusch, E. D., Cassir, M. & Bermond, A. 2010. Application of advanced oxidation processes for TNT removal: A review. *Journal of Hazardous Materials*, 178(1–3), pp.10–28.

Baalousha, M., Manciulea, A., Cumberland, S., Kendall, K. & Lead, J. R. 2008. Aggregation and surface properties of iron oxide nanoparticles: Influence of pH and natural organic matter. *Environmental Toxicology and Chemistry*, 27(9), pp.1875–1882.

Dabrowski, J. M., Peall, S., Reinecke, A. 2001. Runoff-related pesticide input into the Lourens river, South Africa: Basic data for exposure assessment and risk mitigation at the catchment scale. *Water, Air, & Soil Pollution,* 135(1-4), pp.265–283.

Dabrowski, J. M. 2015. Development of pesticide use maps for South Africa. *South African Journal of Science*, 111(1/2), pp. 1-7.

Dalvie, M. A., Africa, A. & London, L. 2006. Disposal of unwanted pesticides in Stellenbosch, South Africa. *Science of the Total Environment*, 361(1-3), pp.8–17.

Dalvie, M. A., Cairncross, E. & London, L. 2009. Pesticide exposure and blood endosulfan levels after first season spray amongst farm workers in the Western Cape, South Africa. *Journal of Environmental Science and Health B*, 44(3), pp.271-277.

Dalvie, M. A. & London, L. 2009. Risk assessment of pesticide residues in South African raw wheat. *Crop Protection*, 28(10), pp.864–869.

Du, J., Yuan, Y., Sun, J., Peng, F., Jiang, X., Qiu, L., Xie, A., Shen, Y. & Zhu, J. 2011. New photocatalysts based on MIL-53 metal – organic frameworks for the decolorization of methylene blue dye. *Journal of Hazardous Materials*, 190(1–3), pp.945–951.

Kuo, Y., Sepúlveda, M. S., Hua, I., Ochoa-Acuña, H. G. & Sutton, T. M. 2009.

Bioaccumulation and biomagnification of polybrominated diphenyl ethers in a food web of Lake Michigan. *Ecotoxicology*, 19(4), pp.623-634.

Meeker, J. D., Singh, N. P., Ryan, L., Duty, S. M., Barr, B. B., Herrick, R. F., Bennett, D. H. & Hauser, R. 2004. Urinary levels of insecticide metabolites and DNA damage in human sperm. *Human Reproduction*, 19(11), pp.2573–2580.

Ndlovu, V., Dalvie, M. A. & Hons, M. 2014. Asthma Associated With Pesticide Exposure Among Women in Rural Western Cape of South Africa. *American Journal of Industrial Medicine*, 57, pp.1331–1343.

Lockwood, D. 2017. Persistent organic pollutants, made by nature. *Journal of Chemical and Engineering news Global Enterprise*, 95(42), pp.13–15.

Quiroz, M. A., Bandala, E. R. & Martínez-huitle, C. A. 2011. Advanced Oxidation Processes (AOPs) for Removal of Pesticides from Aqueous Media. *Pesticides - Dormulations, Effects, Fate*, pp.686-730.

Ruan, Q., Ju, J., Li, Y., Li, X., Liu, R., Liang, G., Zhang, J., Pu, Y., Wang, D. & Yin, L. 2011. Chlorpyrifos exposure reduces reproductive capacity owing to a damaging effect on gametogenesis in the nematode Caenorhabditis elegans. *Journal of Applied Toxicology*, 32(7), pp.527–535.

Samet, Y., Hmani, E. & Abdelhédi, R. 2012. Fenton and solar photo-Fenton processes for the removal of chlorpyrifos insecticide in wastewater. *Water SA*, 38(4), pp.537–542.

Teoh, W.Y., Scott, J.A. & Amal, R. 2012. Progress in heterogeneous photocatalysis: From classical radical chemistry to engineering nanomaterials and solar reactors. *Journal of Physical Chemistry Letters*, 3(5), pp.629–639.

World Health Organization (WHO). 2004. Chlorpyrifos in Drinking-water, Background document for development of WHO Guidelines for Drinking-water Quality.WHO/SDE/WSH/03.04/87.

Xu, H., Ouyang, S., Liu, L., Reunchan, P., Umezawa, N. & Ye, J. 2014. Recent advances in TiO_2-based photocatalysis. *Journal of Materials Chemistry A*, 2(32), pp.12642.

Yang, C. 2014. Persistent organic pollutants in lacustrine environments. PhD (Chemistry) thesis submittedat University of Birmingham. (Accessed@ https://www.etheses.bham.ac.uk>Yang14PhD on 24 October 2018)

CHAPTER 2

LITERATURE REVIEW

2.1 Introduction

Water scarcity is and has been a worldwide problem due to low annual rainfall and water pollution. Amongst other countries, South Africa is one of the countries which recently experienced water shortage in Western Cape province with reports indicating water levels in dams below 37% because of low annual rainfall (DWA 2011).

Water shortage may be due to two factors, i.e. Low annual rainfall which result in low levels of water in dams and surface water. The available water is polluted or rather not safe for human and animal consumption which may be found in wastewater treatment plant, surface water or underground aquifers. The reclamation of pure water from polluted water is a viable solution as this can be human controlled.

Pollutants in water range from microbial, inorganic and organic pollutants which may originate from domestic, industrial and agricultural practices. These sources of pollution may result in one or variety of pollutants indirectly or directly introduced to water bodies. Microbial pollutants may be bacteria (*E. coli*), fungi and protozoa which are associated with diseases such as diarrhea (Awotiwon et al. 2016). In 1997 a case was reported by the department of water affairs whereby diarrhea was responsible for 20% deaths for children aging between 1 to 5 years old and an annual estimate of 43 000 deaths. 3 million incidences of illness that cost approximately R3.4 billion in treatment were observed (DWA 2011).

Inorganic pollutants usually found in water are cationic or anionic species (Okonkwo & Mothiba 2005). Amongst the recently reported inorganic pollutants found in water bodies are heavy metals such as Cd, Pb and Ni. The detected high concentrations are 0.044 mg/L (Cd), 0.035 mg/L (Pb) and 1.777 mg/L (Ni) found in Tyume river Eastern Cape province above the admissible value (Cd=10 µg/L (SA and WHO), Pb=5 µg/L (SA) and 3 µg/L (WHO) and Ni=150 µg/L (SA) and 20 µg/L (WHO)) (Songca et al. 2013; Awofolu et al. 2005). Heavy metals cause various health effects such as cancer and skin infections. For example, lead (Pb) concentration above 0.1 mg/L cause problems with neurological development to foetus and children.

Organic pollutants have been detected in the environment in their broad classes which are pesticides, pharmaceuticals, and volatile organic compounds such as polycyclic aromatic hydrocarbons (Benzene, Xylene and Ethylene glycol) (Kharagpur Web Course n.d.). South Africa is rich in agricultural products which implies that in order to obtain maximum production, the use of pesticides and insecticides is high to eradicate product pests (Glynnis et al. 2012). Pesticides can be washed off into rivers and some can enter ground water, consequently contaminating the water. Most pesticides persist in the environment as a result of bioaccumulation.

There are variety of pesticides in existence in different classes which are carbamates (such as carbosulfan), pyrethroids (such as felvalerate and deltamethrin), organochlorine (such as endosulfan) and organophosphate (such as Aldrin, dieldrin and chlorpyrifos) (Marigoudar et al. 2018; Buckley 2003). These pesticides are associated with various health impacts such as weakness, dizziness, nausea, diarrhea, disorder, and to some extent even death (Alharbi et al. 2018).

Conventional methods have been employed to eradicate or rather remove these pollutants in water bodies including removal in wastewater treatment plant. Most pesticides occur in trace amount, which then lead to failure of conventional methods to remove the pesticides in water. Methods such as advanced oxidation processes (AOPs) showed great potential for the removal of pesticides even in their low levels.

Advanced oxidation processes include photocatalysis and Fenton process (Samet et al. 2012; Ayoub et al. 2010).

Recently, the research focus has shifted to the use of semiconductor photocatalysts for photocatalytic degradation of pesticides which showed great potential (Fadaei & Kargar 2013). Photocatalysis reactions require knowledge of photocatalyst properties such as electronic structure, charge separation and light absorbance to evaluate its eligibility for photodegradation of targeted pollutant under suitable conditions.

2.2 Water pollutants

Water pollutants are those pollutants found in water bodies, either surface or ground water. These pollutants accumulate in water and render the water unfit for animal and human consumption (EAP Task Force, 2007).

An increase in water pollutants is the results of crowding of major cities by both people and industries to advance the standards of living thereby causing an increase in domestic and industrial waste. Water pollutants sources are oil spills, leakage of fertilizers, drainage from metal electroplating and steel works, by-products of industrial processes and combustion of fossil fuels (Dong et al. 2015; Saini & Kumar 2016).

In the major cities reclamation of water is the major route to obtaining portable drinking water as a viable method to combat water scarcity. This require removal of pollutants, because they pose health threats resulting from anthropogenic activities, faecal decomposition and land uses. Some pollutants result from agricultural activities such as pesticides and insecticides (Mojsak & Kaczy 2018).

2.2.1 Microbial pollutants

Microbial water pollution is defined as a form of water pollution caused by microorganisms. Microorganisms may enter into the water system via sewage discharge or from wastewater from industries such as slaughter houses. Microbes such as viruses and bacteria may lead to water borne diseases such as cholera, typhoid, polio and infectious hepatitis in human (Awotiwon et al. 2016).

2.2.2 Inorganic pollutants

Inorganic pollutants include heavy metals and non-metals which are geological and anthropogenic by nature which pollute drinking water. Anthropogenic sources of heavy metals include manufacturing processes and chemical industries.

The highest contributors of heavy metal pollution are the mining industries in South Africa (Edokpayi et al. 2016; Okonkwo & Mothiba 2005; Fatoki & Awofolu 2003). This is evidenced by the introduction of these heavy metals through acid mine water streams and run-offs entering drinking water streams. Other sources of inorganic pollutants such as agricultural run-offs consist of heavy metals-containing fertilizers used in the agricultural fields. Some elements are essential in living organisms such as zinc (Zn) and iron (Fe) in trace amounts (Mohiuddin et al. 2011).

Heavy metals have a high chemical stability, are non-degradable, and bio-accumulation in the environment. These metals accumulate in the living organisms including humans leading to high concentrations in cells over a long period of time which have adverse effects on health such as the cause of cancer (Radulescu et al. 2014). Low levels of toxic metals can also result in health issues such as reduced growth and development, and destruction of vital organs. These heavy metals are exposed to human through contaminated water consumption.

Research on heavy metals, concerning their presence, effects and behavior in drinking water has gained attention. Heavy metals such as cadmium, arsenic, chromium, cobalt and nickel have been studied and found to be amongst the harmful pollutants commonly found in water (Radulescu et al. 2014; Binning & Baird 2001).

Inorganic pollutants such as nitrogen, fluoride, sulphate and phosphate are the commonly detected in water and wastewater in high concentrations. These pollutants result from untreated sewage, detergents and fertilizers. Their introduction in water bodies may result fast growth of plants and algae which use up oxygen causing depletion of oxygen and death of aquatic organisms in a process called eutrophication (Hill et al. 2015).

2.2.3 Organic pollutants

Organic pollutants have been found to play a negative role in the environment. They are the most detected type of water pollutants. They are a result of industrial, pharmaceuticals and agricultural application. These pollutants may be man-made or naturally occurring or rather transform in the environment. Over the years, most organic pollutants have been studied and some are classified as emerging pollutants due to their behavior and lack of knowledge in the environment (Nousiainen et al. 2013).

There are many organic pollutants in the environment and have different chemistry of breakdown and half-lives. Some organic pollutants are classified as persistent organic compounds because they exist in the environment for a very long period of time and thus, lead to environmental distress (Alharbi et al. 2018). Organic pollutants detected so far in the environment include DDT, PCBs and organophosphate compounds (Chlorpyrifos, Aldrin) (Weldon et al. 2011). They are associated with environmental concerns affecting aquatic life and human.

2.3 Persistent organic pollutants (POPs)

These organic pollutants are classified according to their half-lives in the environment. Persistent organic pollutants are basically man-made organic chemicals that are present in the environment for a long period without changing their chemistry or physical properties which is the result of resistance to various degradation processes such as biological and chemical degradation (Nousiainen et al. 2013; Lockwood 2017).

Consequently, the pollutant ends up accumulating in the tissues of living organisms. This type of pollutants may even move to regions they were never used before because they are easy to transport which is made possible by their semi-volatility property, hence high chances of impact on human health and environment.

Persistent organic pollutants are introduced into the environment in two ways which are

➢ Chemicals which have been produced for applications in agriculture, disease control, manufacturing or industrial processes, which includes Polychlorinated biphenyls (PCBs). These pollutants are widely applied as hydraulic and heat exchange fluids in electrical transformers and large capacitors. Dichlorodiphenyl trichloroethane (DDT) was and is still in use for disease vector control of malaria in South Africa and other countries in the world (Weldon et al. 2011).

➢ Chemicals produced unintentionally such as dioxins, the chemicals may result from industrial processes as undesired compounds and from medical and municipal waste.

2.4 Organophosphate pesticides (OPs)

Organophosphate pesticides are man-made chemicals comprising of phosphorous ester group. Organophosphate insecticides were first developed in 1940 in Germany, importantly for defense against agricultural pests (Zimba & Zimudzi 2016;

Buckley 2003). They are widely used as insecticides in agricultural application and home (domestic use).

Insecticides such as diazinon, monocrotophos and chlorpyrifos damage the acetylcholinesterase, an enzyme in the body thus paralyzing/killing the insect (Hamilton et al. 2003). Organophosphate pesticides possess the same mechanism of action as nerve gases like sarin. Therefore, they are referred to as junior strength nerve agents (Yayra et al. 2016).

2.4.1 Chlorpyrifos (CPF)

2.4.1.1 Occurrence

Chlorpyrifos is a widely used organophosphate pesticide (Wang et al. 2016). It is characterized by the linkage of sulphur that is double bonded to phosphorus (**Figure 2.1**). The half-life of chlorpyrifos range from days to years in water. Hence, chlorpyrifos adsorption studies have reported half-life that ranges from hundreds of days to years.

Chlorpyrifos does not readily dissolve in water with 2 mg/L solubility, but has strong affinity to colloids such as soil particles (Mojsak & Kaczy 2018). Study reported that chlorpyrifos showed adsorption to different soil types with a strong linear relationship to soil organic matter. This is caused by the hydrophobic binding sites present in organic matter. CPF loss in water column was observed in the presence of natural colloidal matter faster than any other common pesticides under study (Kravvariti et al. 2010).

2.4.1.2 Prevalence

Chlorpyrifos is extensively applied in broad applications such as agricultural applications for pest control, on ornamental plants, and flea control in animals as

per its registration (John et al. 2015). Chlorpyrifos target pests are the chewing and sucking insects and mites found on economically important crops such as citrus fruits, bananas, vegetables, rice, coffee, potatoes, wheat and cocoa (Fang et al. 2018; Chen et al. 2016). Chlorpyrifos' wide application dominates in agricultural practices together with other organophosphate pesticides (Quintana et al. 2018).
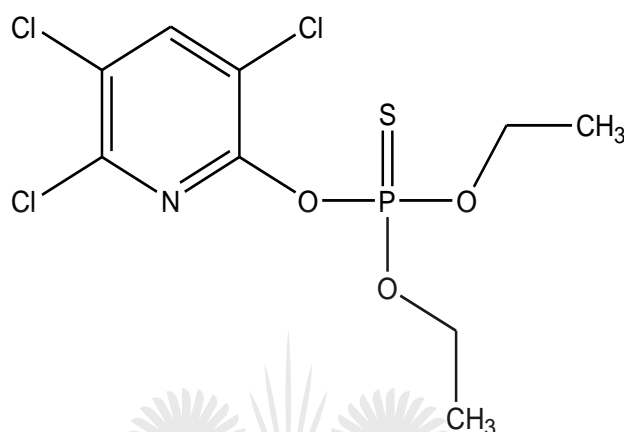
Figure 2.1: Structural formula of Chlorpyrifos (Ismail et al. 2013).

The broad application of chlorpyrifos has led to its detection in the environment whereby it resulted into serious damage to other organisms. This is due to its persistent usage and broad application in variety of pest control measures as reported on contamination on wide range of water and terrestrial ecosystem.

2.4.1.3 Health effects

Chlorpyrifos was reported to have high mammalian toxicity evidenced by negative effects on the endocrine system (endocrine disruptor), immune system, cardiovascular system, respiratory system, nervous system (by interfering with cholinesterase activities) and reproductive system (Lim et al. 2018; Glynnis et al. 2012). Chlorpyrifos is a nerve agent that attacks the chemical pathways and cause nerve breakdown inhibiting their ability to communicate. It is associated with lower IQ and developmental problems in small children (Lim et al. 2018; WHO 2008).

2.4.1.4 Mode of action

In the environment, chlorpyrifos can be broken down or rather converted to other components due to different processes undertaking in the natural environments such as biological, chemical and physical forces in the water, soil, plants and animals (Ishag et al. 2016).
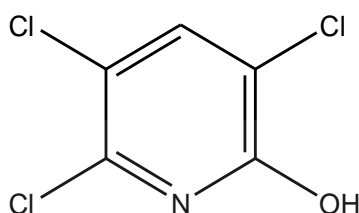
Figure 2.2: Structural formula of 3,5,6-trichloro-2-pyridinol (TCP) (Ismail et al. 2013).

In the presence of light in water, chlorpyrifos was observed to be converted to 3,5,6-trichloro-2-pyridinol (TCP) (**Figure 2.2**), known as a persistent metabolite refractory to microbial degradation (Chen et al. 2012). Accumulation of TCP in liquid medium or soil decreases the degradation rate of chlorpyrifos by preventing the increase in the number of micro-organisms involved in the degradation due to its antimicrobial properties (El Masri et al. 2014).

TCP is a major degradation by product of chlorpyrifos with high water solubility. It causes a widespread contamination of soils and aquatic environments. It results from the cleavage of the phosphorus ester bond of chlorpyrifos (Yang et al. 2017). TCP is classified as persistent and mobile with half-life from 60 to 360 days in soil, depending on soil type, climate and other conditions. In the presence of sunlight, microbial activity can degrade TCP in soils and water to carbon dioxide and organic matter (Liu et al. 2016).

Due to their persistence in the environment, chlorpyrifos and TCP are both considered pollutants in the natural environments, which include water and soil.

Many pesticides have been banned in many countries for use in the environment including chlorpyrifos, specifically in agricultural applications in 20th century, but they are still being detected in high levels in the environment to this date.

Jamieson et al. 2017 studied bioaccumulation of persistent organic pollutants (PCBs and PBDEs) in deep-sea fauna. They reported high concentrations of persistent organic pollutants which were cut-off in 1970 (Jamieson et al. 2017). Weldon et al. 2011 studied accumulation of pesticides in breastmilk of women living in urban and agricultural areas in the United States (Weldon et al. 2011). They found high concentration of chlorpyrifos (28 pg g^{-1} milk) and permethrin (103 pg g^{-1}) in breastmilk of women in agricultural areas than in urban areas (chlorpyrifos=25 pg g^{-1}, permethrin=82 pg g^{-1}).

2.4.1.5 Treatment of chlorpyrifos in water

Research has been conducted on methods to degrade or rather remove these pesticides including chlorpyrifos in the environment which include biological, chemical and physical processes. Amongst other methods, biological methods using bacterial strains isolated from different sources have been reported for degradation of chlorpyrifos, such as *Enterobacter strain B14*, *Paracoccus sp. Strain TRP*, *Bacillus pumilus strain C2A1* (Ishag et al. 2016). However, only *Bacillus pumilus strain C2A1* and *Paracoccus sp. Strain TRP* were found to be efficient for the degradation of chlorpyrifos and TCP (Fan et al. 2018).

Fungal strains have been used to study chlorpyrifos and TCP degradation using *Cladosporium Cladosporioides Hu-01.* The biodegradation resulted in fast removal of chlorpyrifos and TCP within 5 days (Chen et al. 2012). The half-lives of chlorpyrifos and TCP were reduced by 688.0 and 986.9h respectively upon fungus enhancement using inoculum.

Authors suggested fungus as a promising microbial species for bioremediation of chlorpyrifos contaminated water, soil or crops, though strict control of fungal

environment still required for optimal conditions and longer residence time for fungal growth and nurturing. However, the use of amino-substituted calixarene-based magnetic sporopollenin resulted in an excellent chlorpyrifos removal efficiency of 96% at pH 7 within 10 minutes of contact in wastewater contaminated with the pesticide.

Other methods for degradation of chlorpyrifos have been reported such as zero-valent iron incorporated in anaerobic biological treatment plant (Hou et al. 2018) whereby 95.94% removal efficiency of chlorpyrifos was obtained.

Advanced oxidation processes including Fenton processes and photocatalysis have been employed for degradation of chlorpyrifos. 90% COD removal was achieved using Photo-Fenton process under optimum conditions of pH = 3, temperature=35°C, H_2O_2 dosing rate of 120 mg/min and initial Fe^{2+} concentration of 5.0 mM. These were the dependent factor of the Fenton process (Samet et al. 2012).

Photocatalytic degradation of chlorpyrifos was achieved using TiO_2 and ZnO nanoparticles under UV light irradiation (Fadaei & Kargar 2013). Chlorpyrifos removal rate was 80% and 90% for UV/ZnO and UV/TiO_2 respectively. The reaction was conducted under optimum pH of 9 and initial photocatalyst concentration of 0.15 g/L.

Furthermore, coupled semiconductor have been used to degrade chlorpyrifos in water. The coupled photocatalyst reported was composite made of $CoFe_2O_4$@TiO_2 decorated on the reduced graphene oxide layer (Gupta et al. 2015). The degradation of chlorpyrifos achieved more than 90% using 0.4 g/L at pH 5.8 within 60 minutes.

2.5 Treatment methods for chlorpyrifos

2.5.1 Advanced oxidation processes (AOPs)

Advanced oxidation processes are hydroxyl radicals mediated set of chemical treatment processes developed to remove pollutants in water and wastewater by oxidation reactions (Stocking et al. n.d.). They are categorized in two groups such as heterogeneous processes and homogeneous processes (Ayoub et al. 2010). The heterogeneous processes involve materials in different phases (Organic pollutant being in a different phase compared to the degradation mediator).

Examples of heterogeneous processes are catalytic ozonation and photocatalysis (Quiroz et al. 2007). Whereby examples of homogeneous processes are ultraviolet radiation, and electrochemical oxidation. The most popular and most used processes are the Fenton process and photocatalysis due to their excelling pollutant degradation capabilities. They improve the biodegradability of recalcitrant water and wastewater (Ayoub et al. 2010).

The Fenton process is one of the most investigated advanced oxidation processes for water treatment. It is reported to be the most effective methods for oxidation process of organic pollutants (Quiroz et al. 2007). The Fenton process incorporate the use of hydrogen peroxide and iron species (H_2O_2/Fe^{2+}) as the Fenton reagent (Samet et al. 2012). These reagents displayed efficiency in the treatment of various water and wastewater pollutants including pesticides, aromatic compounds, and dyes (Quiroz et al. 2007).

The Fenton reagents allow high depuration levels at room temperature and pressure conditions through nontoxic and easy to handle reactants through the formation of a hydroxyl ($HO^{\bullet}$) radical and oxidation of Fe^{2+} to Fe^{3+}, illustrated in **Equation 2.1**. The disadvantages of using the Fenton process include the production of high amount of $Fe(OH)_3$ which precipitates. The precipitates causes an additional water pollution by the homogeneous catalyst used as an iron salt and the catalyst cannot

be retained in the process (Quiroz et al. 2007). Thus, other methods were explored such as photocatalysis.

$$Fe^{2+} + H_2O_2 \rightarrow Fe^{3+} + HO + HO\bullet \qquad\qquad \textbf{2.1}$$

2.5.1.1 Photocatalysis

Photocatalysis is a light induced chemical reaction on a semiconductor catalyst's surface. This is due to photogenerated charge carriers (electrons and holes) migrating to the semiconductor surface to initiate chemical reactions on the adsorbed molecules (Batzill 2011; Marschall 2014). Photocatalysts are chemically stable, potential in environmental remediation, sensors, solar energy conversion, photodegradation of organic and inorganic pollutants, and water splitting (Tang et al. 2015).

Photocatalysis reaction mechanism is easy to follow, such that light is irradiated on the surface of the photocatalyst, therefore, the incident light is absorbed by the photocatalyst, provided the energy of the incident photons is equal or larger than the semiconductor band gap energy. The electrons from the valence band (VB) get excited and occupy conduction band (CB), and holes remain in the valence band (**Figure 2.3**).

The photoexcited electrons can be used for electrochemical reduction of oxygen to oxygen radicals when the CB minimum of the semiconductor photocatalyst is positioned at a more negative potential than the electrochemical potential of oxygen reduction ($O_2/^{\bullet}O_2^{-}$ = -0.33V at pH 7) (Xu et al. 2014; Batzill 2011). The electrons in the conduction band powerful enough to directly reduce metals/metal ions considering their electrochemical reduction potential.

The holes created in the VB of the semiconductor can be used to oxidize molecular water into hydroxyl radical considering the VB minimum of the photocatalyst is more positive than the redox potential of water to hydroxyl radical (Xie et al. 2012). The

hydroxyl radicals which are powerful oxidizing agents can be used for degradation of organic pollutants.

Ex - Excitation
R - Recombination
E_g - Bandgap energy
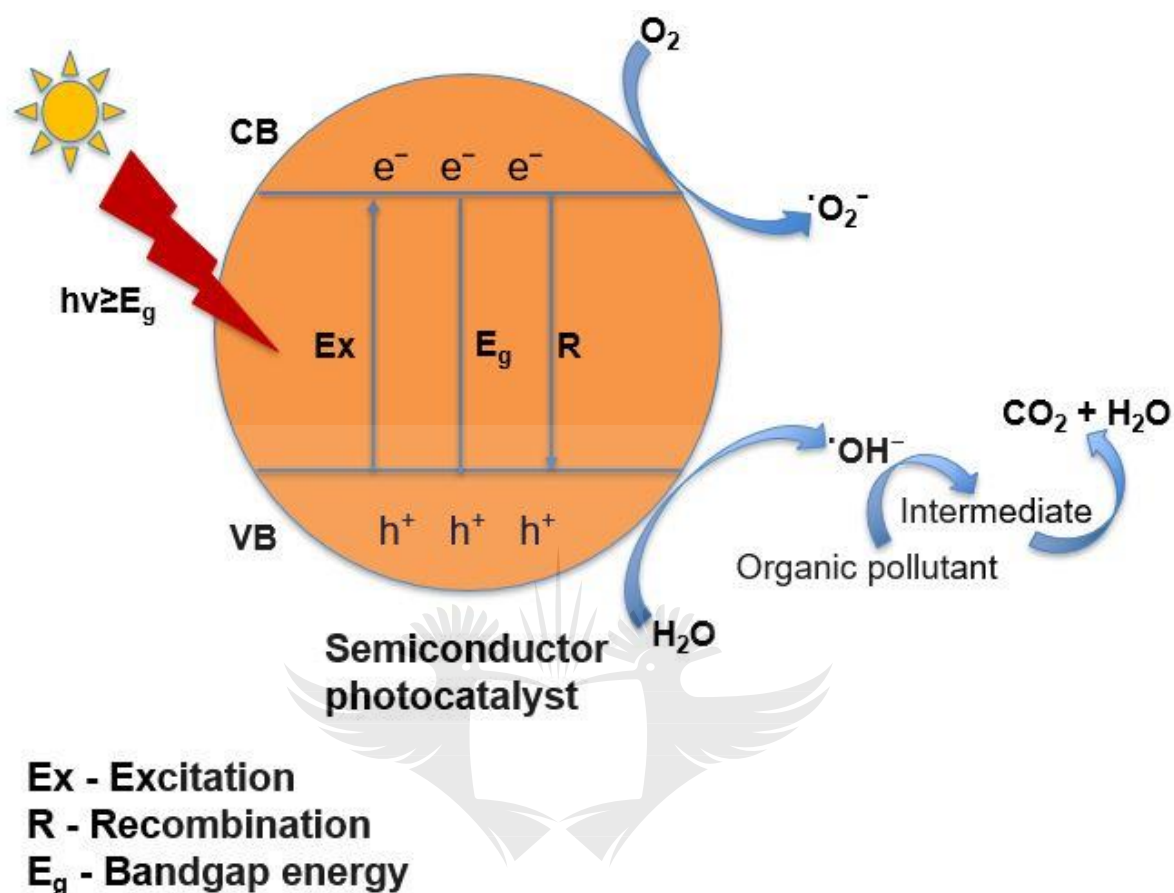
Figure 2.3: Photocatalysis reaction mechanism (Marshall 2014).

In the occasion that electrons are not utilized, they return to the VB, therefore recombining with the generated holes. Photocatalysis reaction process can generally be explained using three mechanistic steps such as the excitation, bulk diffusion and surface transfer of photogenerated charges (Marschall 2014).

In heterogeneous photocatalysis, the semiconductor photocatalyst redox reactivity is affected both by electronic and surface atomic structures. According to surface atomic arrangement and coordination that determine the reactant molecules adsorption intrinsically, surface charge transfer occurs between adsorbed molecules and photogenerated charges. Therefore, an efficient photocatalyst maximizes charge transfer for photodegradation of adsorbed molecules and consequently result in low charge recombination.

Pristine photocatalysts have been employed for photocatalytic degradation of pollutants in water such as TiO_2 (Xu et al. 2014), WO_3 (Georgaki et al. 2015; Fakhri & Behrouz 2015b), ZnO (Abudayyeh 2014; Khan et al. 2015), and SnS_2 (Fakhri & Behrouz 2015a). The most studied photocatalysts are TiO_2 and ZnO as they possess similar characteristics such as absorption only in the ultraviolet light (UV). This is due to a large band gap, stability at wide pH range, nontoxicity and are cheap.

The disadvantage with these photocatalysts is that they only absorb in the UV region which accounts for 4% of the solar spectrum (Raj 2012). Research interests has recently focused on developing visible light absorbing photocatalysts such as WO_3, SnS_2 and SnO_2 (Kim et al. 2018; Rahimnejad et al. 2014). Even though these photocatalysts are active under visible light, they still suffer from high photogenerated charge recombination. The proposed ways to combat the limitations encountered in semiconductor photocatalysts are doping (metal/non-metal), dye sensitization, phase-junction and heterojunction formation (Marschall 2014; Chowdhury et al. 2017).

2.5.2.2 Photocatalyst modification

Modification of photocatalysts has been studied after realization of the limitations encountered by single photocatalysts. Consequently, research interests have embarked on modifying the photocatalysts' intrinsic properties using various methods including doping (metal/non-metal), dye sensitization, facet design and heterojunction formation to enhance their photocatalytic properties. It is of paramount importance to modify the photocatalyst to suit the desired feature for a complete removal of the targeted pollutant.

2.5.2.2.1 Dye-sensitization

Dye sensitization involves the addition of an organic molecule to semiconductor photocatalyst to enhance the absorption capability of the photocatalyst (**Figure 2.4**).

This type of modification is mainly used for visible light absorption capabilities whereby it is purposefully introduced to enhance visible light absorption of UV light absorbing photocatalysts such as TiO_2 and ZnO (Watanabe 2017; Youssef et al. 2018). Types of dyes are xanthene dyes, transition metal-based dyes and organic dyes.

Dye-modified photocatalysts using TiO_2 have been reported. In these studies improved electron transport was observed due to optimization of compact layer/perovskite interface by an organic dye sensitization utilizing a triazine-substituted zinc porphyrin as an electron transport later (ETL) (Youssef et al. 2018; Momeni 2016). Balis et al. 2018 discussed the use of metal free organic dye D35 as a sensitizer in liquid- or solid-state DSSCs.

D35 was found to be an efficient sensitizer on TiO_2 due to its butoxyl chains that enhance semiconductor protection by providing self-assembly and allows the formation of TiO_2 aggregates free dye layer surface (Balis et al. 2018). Consequently, acting like an insulating hydrophobic shield that prevents the oxidized species away from TiO_2 surface and suppressing the electron recombination. They observed high output power conversion efficiencies (PECs) of 13% for D35 modified Titania sensitized cells which outperformed cells without D35.
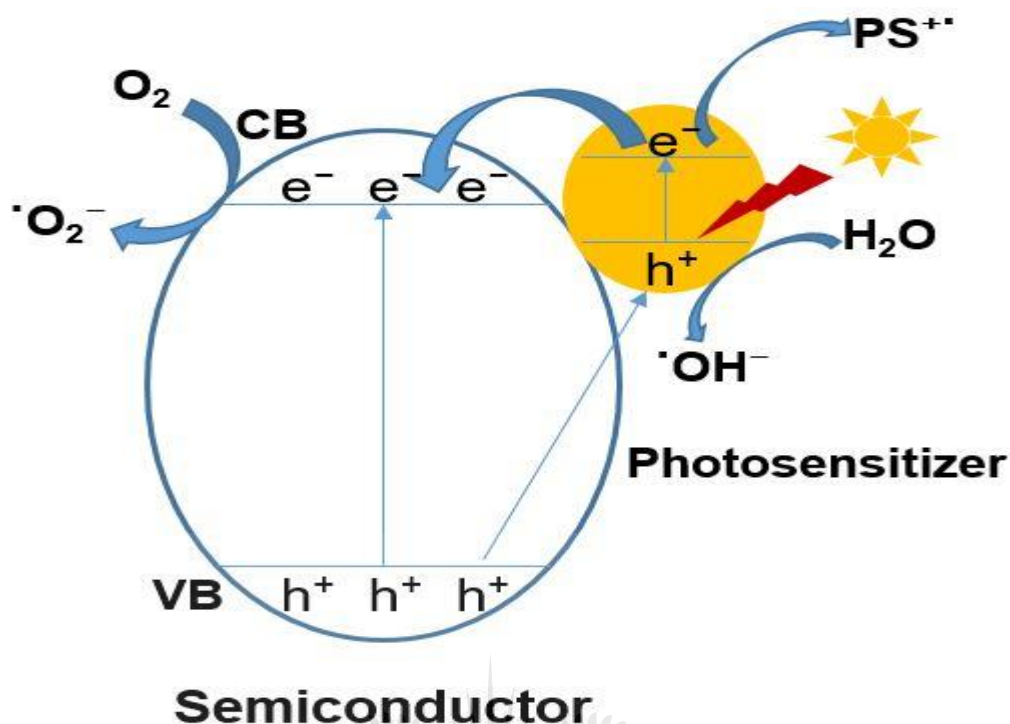
Figure 2.4: Schematic diagram of photosensitized photocatalyst (Youssef et al. 2018).

The disadvantage with dye sensitization is the development of a NPs-sensitized system that have good stability, intensive visible light harvesting capabilities and high photocatalytic activity.

High photocatalytic activity is obtained by optimizing parameters such as the type of nanomaterial (TiO_2, ZnO, fullerenes, graphene), nature and content of photosensitizer (xanthene dyes, transition metal-based dyes, organic dyes), presence or absence of heavy metal atoms in the cavity of the photosensitizers, linkage mode between photosensitizer and the surface of the NPs (physisorption, covalent grafting) and the type of light utilized for the photocatalytic applications (UV, Visible or solar) (Youssef et al. 2018).

2.5.2.2.2 Metal/Non-metal doping

Doping is an introduction of an impurity into the lattice crystal of a semiconductor photocatalyst. The impurity may be a metal or non-metal ion. In metal doped

photocatalysts, the metal forms a Schottky junction (interface) with the photocatalyst (**Figure 2.5**) (Xiang et al. 2010; Li et al. 2015). The interface allows electron transfer from the semiconductor to the metal ion by aligning the fermi levels of the metal dopant and the semiconductor, therefore, results in the enhancement of the photocatalytic activity of the semiconductor photocatalyst (Wang et al. 2015; Li et al. 2015).

The metal dopant generally acts as an electron sink by temporarily trapping the electrons. Consequently, this reduces the electron-hole charge recombination which results in efficient charge separation and transfer. The metal dopant on the semiconductor photocatalyst can also act as reaction active site thereby increasing the number of active sites on the photocatalyst (Ran et al. 2013).
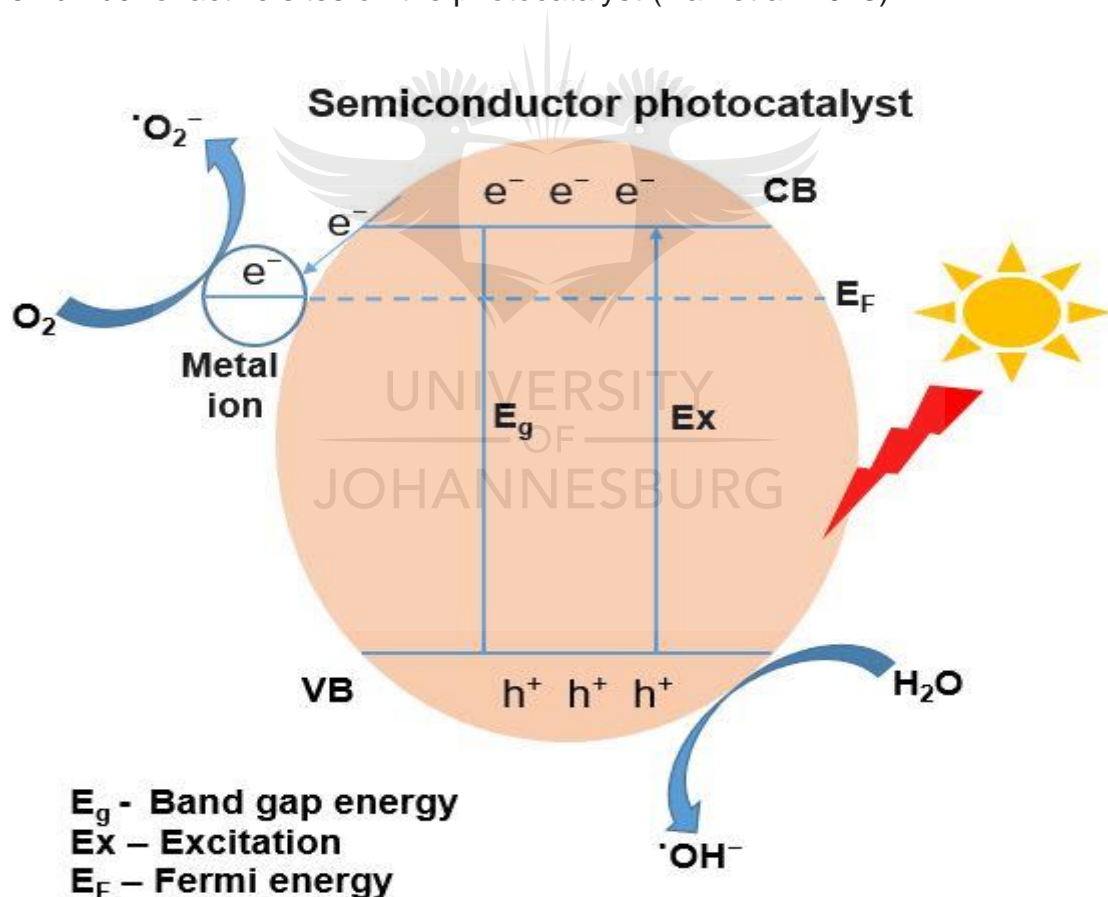
Figure 2.5: Schematic diagram of metal doped semiconductor photocatalyst (Li et al. 2015).

The metal dopants reported so far include silver (Ag), gold (Au), manganese (Mn), magnesium (Mg), copper (Cu) and platinum (Pt) (Ran et al. 2013). Some examples

of the resulting metal doped photocatalysts are Mn-WO$_3$ (Parthibavarman & Prabhakaran 2017), Pt-TiO$_2$ (Li et al. 2015) and Au-BiVO$_4$ (Ran et al. 2013).

Reported Schottky junction formed between Pt and TiO$_2$ (Pt-TiO$_2$) showed improved charge separation and enhanced photocatalytic activity for water splitting (Xu et al. 2014). This was alluded to the presence of Pt having a large work function and low activation energy for H$_2$ evolution. The disadvantage of metal dopant is that at high degree of doping may lead to high recombination rate due to excess of the metal dopants acting as recombination centers. This method was employed in this study whereby appropriate metal dopant level was used for optimum performance.

In non-metal doping, a semiconductor photocatalyst is modified using a non-metal inserted close to its valence band maximum (**Figure 2.6**) (Islam et al. 2017). Compared to metal ions, non-metal ions are less prone to formation of recombination centers and have found to be more effective on the photocatalytic activity enhancement, especially of TiO$_2$. It occurs due to the ability of the non-metal dopant to narrow the band gap of the semiconductor because the related impurity states are located close to the valence band maximum.
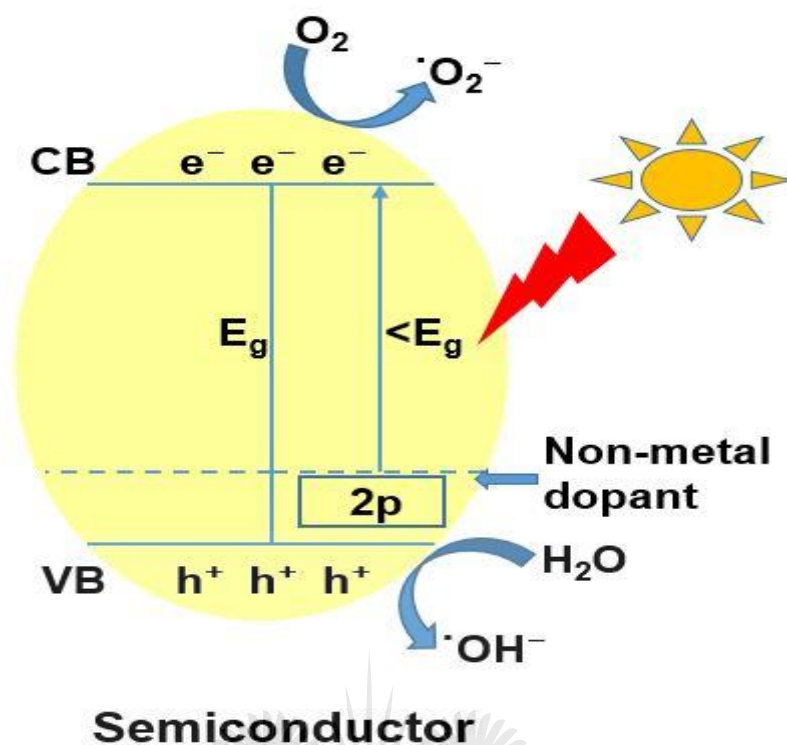
Figure 2.6: Schematic diagram of non-metal doping (Islam et al. 2017).

The reported non-metal dopants include nitrogen, fluorine, sulphur and iodine (Yang et al. 2009). The most studied semiconductor photocatalyst (TiO_2) was subjected to non-metal doping using nitrogen as dopant. The nitrogen dopant decreased the band gap of TiO_2 allowing the photocatalyst to absorb visible light (Islam et al. 2017).

However, non-metal doping has limitations such as strict reaction conditions and the non-metal are unstable, difficult to control and the process is tedious. Some non-metal dopants have ionic radius that is too large to be incorporated into the semiconductor lattice. Example, Sulphur has a large ionic radius to be incorporated into TiO_2 lattice crystal.

2.5.2.2.3 Phase junction

Phase junction is the formation of two crystallographic phases of a semiconductor photocatalyst joined together as illustrated in **Figure 2.7** (Li et al. 2015). The phase

junction occurs by transitioning one phase slightly onto another phase, as a result, two phases are present in conjunction with one another. The different phases pose different photocatalytic activity of which when combined can enhance the activity of the photocatalyst. This is due to improved charge separation because photogenerated charges will move from one phase to another of that photocatalyst.

Methods for achieving phase junction include adjusting of pH, degree of doping, and temperature (Li et al. 2015). These methods can achieve phase transitioning and stabilization from one phase onto another thus forming a phase junction. An example of a phase junction is TiO_2 anatase/rutile junction whereby electron transfer occurred from the conduction band of anatase to the conduction band of rutile therefore increasing photoactivity by increasing separation of photogenerated charges (G. Liu et al. 2011). Though the disadvantage is that the method is tedious.
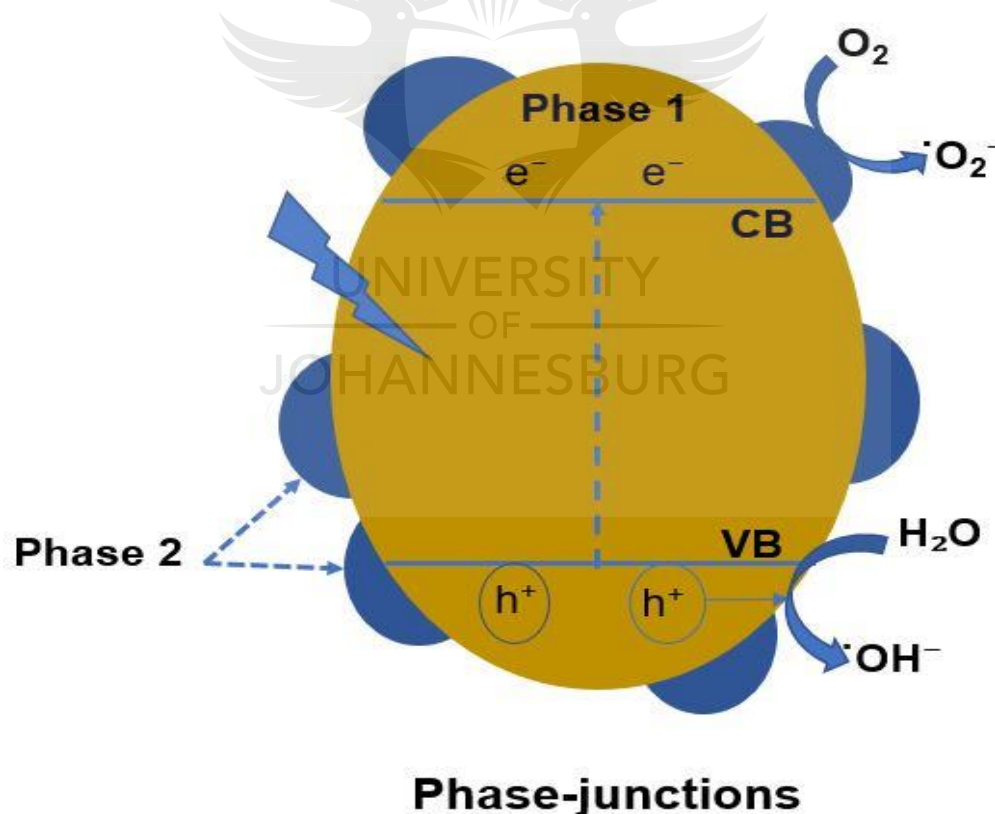
Figure 2.7: Schematic diagram of phase-junction composite (Li et al. 2015).

2.5.2.2.4 Heterojunction

Heterojunction is the interface of two photocatalyst materials with different band gaps joined together through a junction barrier (Tang et al. 2015). The heterojunction is formed to overcome photogenerated charge recombination by movement of charges from one photocatalyst to another, thereby facilitating electron and hole separation. There are two types of heterojunctions reported such as *p-n* and *n-n* heterojunctions. These heterojunctions are aligned based on the band edge positions. There are three types of alignment in the heterojunction set-up, being type I, type II and type III (**Figure 2.8**) (Tang et al. 2015; Marschall 2014).
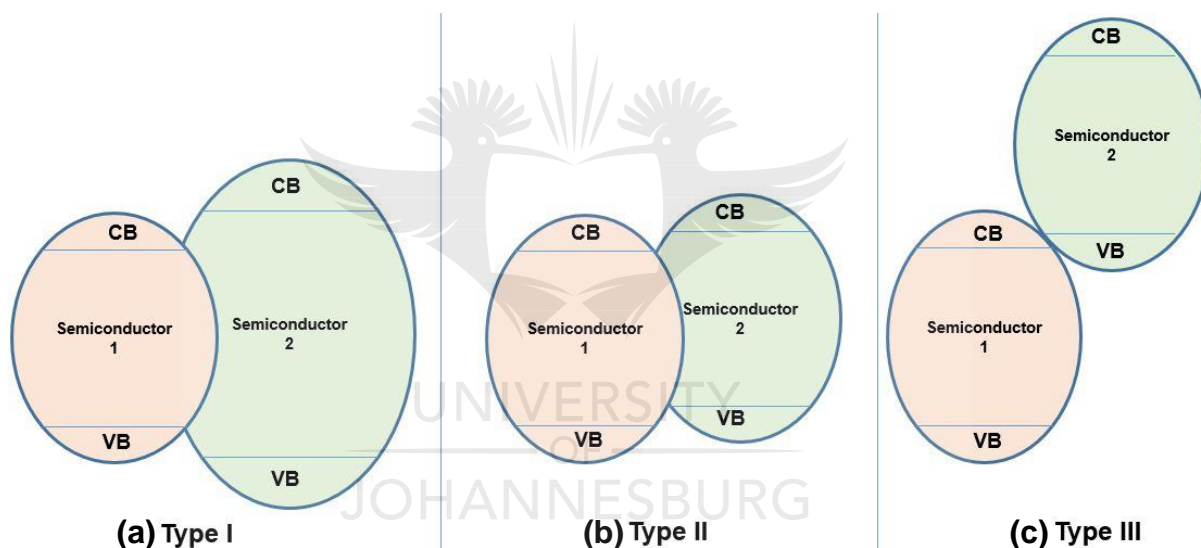
Figure 2.8: Schematic diagram of different types (I-III) of heterojunctions (Marshall et al. 2014).

Type I heterojunction involves sandwiching one of the semiconductor band edges into another semiconductor (**Figure 2.8(a)**), which results in all the photogenerated charges accumulating on one semiconductor (Marschall 2014). This yield no improvement in the photocatalytic activity; however, the type of heterojunction is common.

Type II heterojunction have respective band edges of one semiconductor above the corresponding band positions of the other semiconductor CB(2) above CB(1) and VB(2) above CB(1)) (**Figure 2.8(b)**). The photoexcited electrons are transferred from the CB(1) to CB(2). The photogenerated holes are then simultaneously transfer from VB(1) to VB(2). Therefore, the movement of photogenerated charges result in low recombination rate and consequently separate the electrons from holes (Tang et al. 2015).

This type of heterojunction is the best amongst the other two types and it is observed in many composite photocatalysts. It results in improved photocatalytic activity due to optimum band positioning for efficient charge separation. In this work, type II heterojunction was chosen based on the advantages it poses also due to WO_3 and SnS_2 band positioning (Li et al. 2014).

Type III heterojunction involves one semiconductor with both its CB and VB further set off from the other semiconductor CB (**Figure 2.8(c)**). This type of heterojunction is called broken-gap situations and is uncommon due to less charge separation (Marschall 2014).

2.5.2.2.4.1 *p-n* heterojunction

p-n heterojunction is a heterojunction formed between a *p*-type semiconductor with an *n*-type semiconductor, shown in **Figure 2.9** (Li et al. 2015). The two semiconductor photocatalysts have different charge carriers which are holes and electrons for *p*-type and *n*-type respectively. This type of heterojunction has been employed for the modification of photocatalytic activity of a semiconductors such as $CaFeO_4$/WO_3 forming a z-scheme photocatalysis (Miyauchi et al. 2013).

Furthermore, coupling of Cu_2O(*p*)/CuO(*n*) semiconductors led to more than 80% norfloxacin degradation under visible light, this was attributed to the charge separation induced in the heterojunction composite (Mamba et al. 2017). Based on

the chosen semiconductor materials, this type of heterojunction can form any of the three band alignment designs (type I, II, and III).
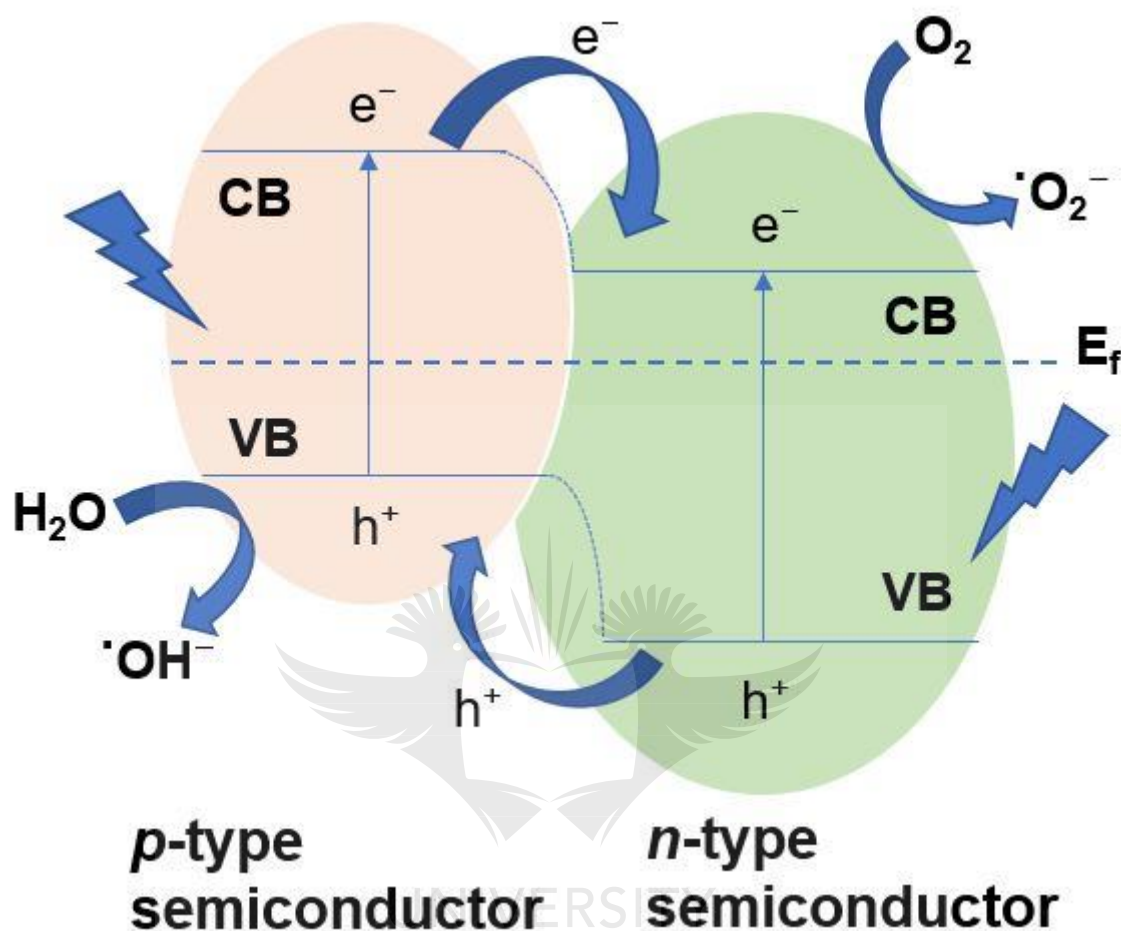
Figure 2.9: Schematic diagram of *p-n* heterojunction (Li et al. 2015).

2.5.2.2.4.2 *n-n* heterojunction

n-n heterojunction is a heterojunction formed by two *n*-type semiconductors (**Figure 2.10**) (Li et al. 2015). Its charge mobility is capacitated by electrons due to both semiconductors' charge mobility facilitated by electrons. There are many heterojunction photocatalysts of this type formed which showed improved charge separation and enhanced photoactivity such as $WO_3/BiVO_4$ (Zheng et al. 2017). This type of heterojunction is used in this work due to both WO_3 and SnS_2 being *n*-type.

This type of heterojunction is the most studied and formed so far due to its effective charge separation. Most of *n-n* heterojunctions form type II design, as expected in this study. The photogenerated electrons will flow from SnS_2 (CB) to WO_3 (CB) and consequently the photogenerated holes migrate from WO_3 (VB) to SnS_2 (VB) thereby enhancing charge separation (Li et al. 2014).
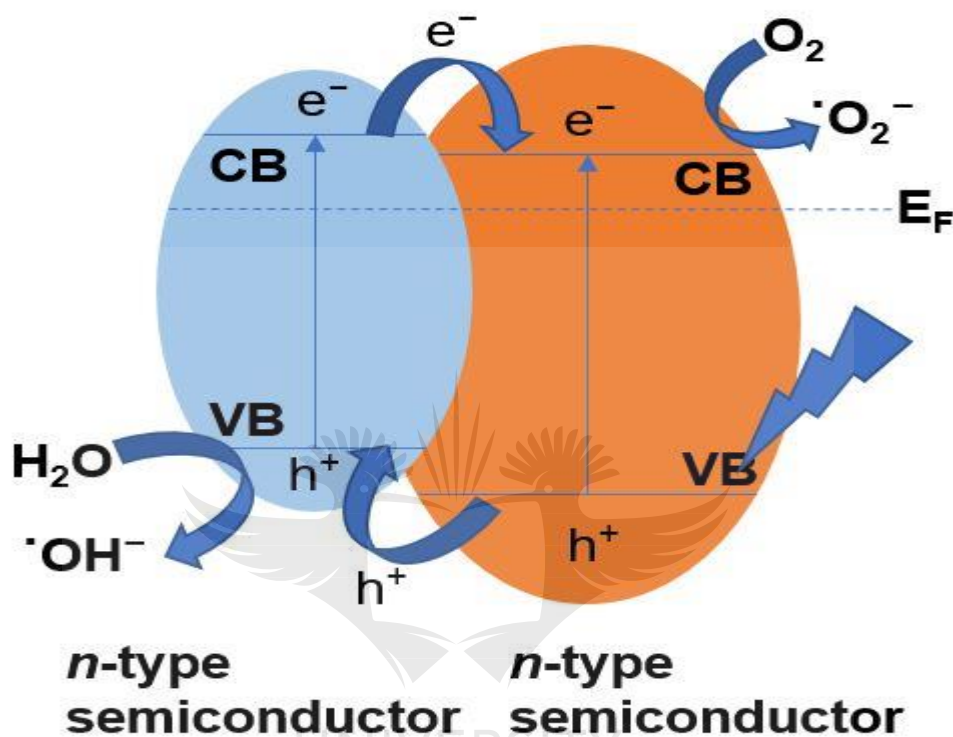
Figure 2.10: Schematic diagram of *n-n* junction heterojunction (Li et al. 2015).

2.5.3 Tungsten trioxide (WO₃)

Tungsten trioxide (WO_3) is one of the mostly studied semiconductor photocatalysts. This is due to its interesting properties such as narrow band gap between 2.2 to 3.2 eV allowing visible light absorption (Kominami et al. 2001). Its electronic band gap (E_g) corresponds to the space between the valence band energy level formed by filled 2p orbitals of oxygen and the conduction band energy level formed by the empty tungsten 5d orbitals (Simelane et al. 2017).

WO_3 is an n-type semiconductor, which implies that major charge carrier mobility is facilitated by electrons (Chae et al. 2017). Nanostructured WO_3 generally have band

gap increase upon grain size reduction. This is observed experimentally by a blue shift of the optical absorption band edge. The blue shift is attributed to quantum confinement (QC) effects (Rahimnejad et al. 2014). Due to its optical properties, applications in photocatalysis under visible light is possible, considering the abundance of visible light in the solar spectrum.

Like other photocatalysts, WO_3 has limitations such as recombination of photogenerated charges. Tungsten trioxide nanomaterials have been extensively studied for its properties in variety applications such as electrochemical gas sensing, water splitting, and photocatalysis (organic and inorganic degradation) (Xie et al. 2012).

The advantages of working with WO_3 are that synthesis of the nanomaterial is easy and obtainable in high purity (Ahmadi et al. 2014). This is the reason WO_3 nanomaterials can be synthesized to obtain different polymorphs (Srivastava et al. 2006). It is based on the nature of WO_3 existing in different crystalline phases which arise from the three-dimensional array of corner and edged sharing WO_6 metal-oxygen octahedral in its original structure illustrated in **Figure 2.11** (Cui 2005).
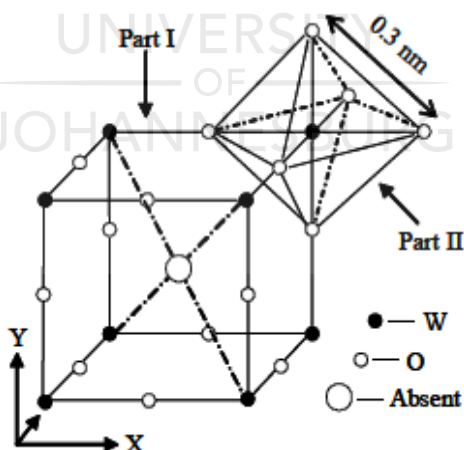
Figure 2.11: Unit cell of the perovskite lattice (Part I) and octahedral symmetries (Part II) in the perovskite structure (Cui 2005).

Different phases arise due to corner and sharing of atoms in WO_3 structure. The W atom is displaced from the octahedral center thereby causing a distortion and the displacement is temperature dependent. As a result, different crystalline phases are

formed such as monoclinic, triclinic, orthorhombic and tetragonal. These crystalline phases are formed in temperatures between <123K to 1013K through annealing and cooling processes (Rodríguez-Pérez et al. 2015).

Monoclinic phase is the most stable and the most photocatalytic compared to the other phases. Monoclinic tungsten trioxide was chosen for this work due to its superior properties. Tungsten trioxide, like many other semiconductor photocatalysts suffers from high photogenerated charge recombination. This need to be combated with various methods, and in this work, doping and heterojunction formation will be used as described in the previous sections.

Table 2.1: WO_3 crystalline phases and their corresponding temperatures of formation.

Crystal structure	Crystalline phase	Temperature formation
Monoclinic II	ε-WO_3	<-43
Triclinic	δ-WO_3	-43 to 17
Monoclinic I	Υ-WO_3	17 to 330
Orthorhombic	β-WO_3	330 to 740
Tetragonal	α-WO_3	>740

2.5.4 Tin (IV) disulphide (SnS2)

Tin (IV) disulphide (SnS_2) is a visible light active semiconductor with a narrow band gap (E_g) between 2.0-2.5 eV (Burton et al. 2016; Zhou et al. 2017). The resultant conduction band position is more negative on the normal hydrogen electrode (NHE) than H_2/H_2O reduction potential and its valence band is less positive than O_2/H_2O. Sn usually form hexagonal structure when in oxidation state of +4 (Du et al. 2011). SnS_2 crystal structure displays that Sn (IV) coordinates to six S atoms in a regular octahedral (**Figure 2.12**) (Whittles et al. 2016).
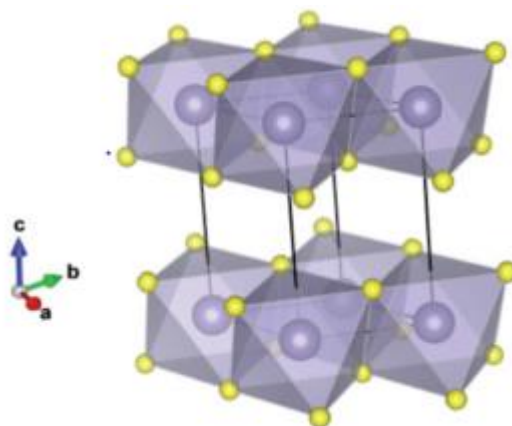
Figure 2.12: Ground state (2H) structure of SnS_2 showing the 2-dimensional bonded plane of edge-sharing octahedra and the conventional unit cell (Whittles et al. 2016).

Tin (IV) disulphide is a good semiconductor photocatalyst because of its wider spectrum response, nontoxic, abundance, relatively inexpensive and chemically stable in acid or neutral solutions (Yang et al. 2016). It has been applied in a wide variety of application in its pristine or doped with other material (Ou et al. 2015; Zhang et al. 2011). The applications range from electrochemical sensors, adsorption, and photocatalysis on variety of environmental pollutants (Luo et al. 2018; Yu et al. 2014; Mondal et al. 2014).

Ma et al. 2015 reported a formation of composite material of tin (IV) sulphide-reduced graphene oxide (SnS_2-rGO) which was applied in Na-ion batteries (Ma et al. 2015). The composite exhibited a reversible capacity of 630 mAhg-1 with high performance rate. It also showed a potential of splitting water with a photon-to-current conversion efficiency of 38%.

Christoforidis et al. reported the ability of SnS_2 to act as oxidizing agent and charge carrier separator when ultrathin decorated on 1D anatase TiO_2 using a one-step soft hydrothermal process (Christoforidis et al. 2015). Furthermore, formation of heterojunction of SnS_2 with Ag_2CO_3 showed an enhanced visible-light photocatalytic activity for the degradation of organic pollutants. The composite (Ag_2CO_3/SnS_2) with weight content of 2.0% Ag_2CO_3 gave degradation of methyl orange of 6.22, 1.65 times higher than those obtained using pure Ag_2CO_3 and SnS_2, respectively (Luo et

al. 2015). This was alluded to the synergistic effect between Ag_2CO_3 and SnS_2 with improved photogenerated charge separation and enhanced interfacial charge transfer.

2.6 Synthesis of nanomaterials

Nanomaterials are synthesized using different methods especially due to their size and their different polymorphs. Two ways have been proposed for their synthesis which are bottom-up and top-down approaches (Y. Liu et al. 2011). Bottom-up approach involves the synthesis of the nanomaterials from atomic level, further undergoing self-processing leading to nanostructure formation (Saravanan et al. 2008). During the self-assembly process, physical forces operate at nanoscale to combine basic units into larger stable structures (Moores 2018).

This technique consists of chemical synthesis, chemical vapor decomposition, hydrothermal reactions, thermal spray technique, inert gas condensation rapid solidification and electrodeposition (Aoki et al. 2016). Most applications use bottom-up approaches because they are readily accessible, low-cost and productive. But they suffer from inability to precisely control particle shape, size and dispersity (Yamamoto et al. 2013).

Top-down approach is a lithographic method for generating desired patterns in nano- or micro-scale. Top-down methods provide nanomaterials with high consistency and high controllability on pattern size and shape (Y. Liu et al. 2011). The methods have disadvantages such as high costs of equipment and limited access to fabrication facilities. The fabrication capacity of top-down methods is low which disadvantage the use of this approach.

PRINT (Particle Replication In Non-wetting Templates) process is the best top-down synthesis method that is less costly and highly scalable (Fu et al. 2018). Though it still shows lower fabrication capacity than most bottom-up methods. Examples of top-down methods are photolithography and PRINT. The most studied method is

the photolithography due to advantages such as reliability, productivity and convenience.

2.6.1 Hydrothermal method

Hydrothermal method is described as a crystal synthesis or crystal growth carried out at high temperature and pressure water conditions from insoluble substances under ordinary temperature and pressure (Hayashi & Hakuta 2010). This method is widely used and most effective route for the synthesis of nanomaterials of different shapes, size and polymorphs. The reactants are sealed into an autoclave filled with water to form a solution and heated under high pressure and temperature conditions.

Teflon-lined autoclaves are capable of withstanding high temperatures and pressure which allows for hydrothermal synthesis to be carried out at extreme temperature and pressure conditions (Khanjani & Morsali 2010). The particle size of the metal oxide depends on the hydrolysis rate and its solubility (Navarro et al. 2014). This method can be carried out in batch type or continuous flow type to obtain the desired products. The reaction conditions can be controlled by instantaneous mixing and sudden temperature increase which results in supersaturation, though rapid heating is important when small and homogeneous NPs are produced.

The initial set-up of reaction parameter is easy to conduct. The low cost of this method makes it viable to obtain small and homogeneous NPs (Aoki et al. 2016). Based on the advantages this method possesses, it was adapted for use in this work as it has been reported to produce desired small NPs with homogeneous shape and these nanoparticles exhibit high photocatalytic activity.

2.6.2 Sol-gel method

Sol-gel synthesis method is used for the preparation of metal oxide nanoparticles and nanocomposites (Danks et al. 2016). It is a wet chemistry technique that involves processes such as hydrolysis and polycondensation reactions from metal and metalloid elements which are surrounded by ligands. The metal oxides are formed by connection of metal centers with either oxo (M-O-M) or hydroxo (M-OH-M) bridges, thereby producing metal-oxo or metal-hydroxo polymers in solution as illustrated in **Equations 2.2-2.4** (Simonsen & Søgaard 2010):

$$W\text{-}OR + H_2O = W\text{-}OH + ROH \text{ (hydrolysis)} \qquad \textbf{2.2}$$
$$W\text{-}OH + OR\text{-}W = W\text{-}O\text{-}W + ROH \text{ (condensation)} \qquad \textbf{2.3}$$
$$W\text{-}OH + HO\text{-}W = W\text{-}O\text{-}W + H_2O \text{ (condensation)} \qquad \textbf{2.4}$$
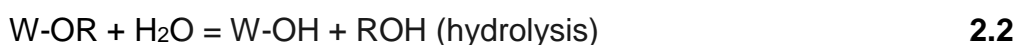
Sol-gel synthesis methods differ from other methods due to its unique properties such as the production of solid-state materials from homogenized chemical precursors and the ability to control the size and morphology of the particles they produce (Tseng et al. 2010). There are two types of sol-gel methods based on the type of reaction medium used, namely, aqueous sol-gel method which uses water as the reaction medium and non-aqueous sol-gel method which involves the use of organic solvent as reaction medium (Dimitriev et al. n.d.). Tungsten trioxide synthesized using sol-gel method was reported with defined structures (Prentice et al. 2006).

2.6.3 Precipitation method

Precipitation synthetic method for nanomaterials is mainly based on shape, size and composition control (Wu et al. 2019). This method was extensively studied and used because of its low operation cost, large scale use in industrial production and unsophisticated equipment needed (Sharma et al. 2016; Wu et al. 2019). High yields are produced, though the surface area of the powder is compromised due to production of irregular particle morphology, large particle size distribution and high

degree of agglomeration. WO_3 nanoparticles were synthesized using this method on a polyethylene glycol (PEG) template as steric stabilizer to obtain polyhedral shapes (Luévano-hipólito et al. 2014). The nanoparticles exhibited high surface area and uniform shapes.

2.7 Characterization techniques

These techniques were used to analyze and confirm the successful formation of the materials synthesized in this project. Their theory and applications are discussed below.

2.7.1 Powder X-ray diffraction spectroscopy (XRD)

X-ray diffraction spectroscopy provides information about the material's phase transition, crystallographic appearance and polymorphism. This technique can give information regarding unit cell dimensions and its used to determine the degree of crystallinity or amorphization of the sample material, which is performed on a finely ground and homogenized samples (Das et al. 2014; Kuzmin & Purans 2014).

In principle, XRD is based on constructive interference of monochromatic X-ray irradiation and a crystalline sample (Das et al. 2014). The instrument consists of a cathode ray tube with a filament that upon heating generate X-rays to produce electrons. A voltage is applied to accelerate the produced electrons toward the target material. When conditions meet equation **2.5** known as Bragg's law, a constructive interference occur when the incident rays interact with the samples material. In the Bragg's law, n is an integer, λ is the wavelength, d is the spacing between two lattice points and θ is the incident beam angle (Jenkins 2000).

$n\lambda = 2d \sin \theta$ **2.5**

The characteristic X-ray spectra is produced when electrons have enough energy to move inner shell electrons of the target material at specific wavelength characteristic to target material (Cu, Fe, Mo or Cr). The monochromatic X-rays needed for diffraction are produced after filtering other X-rays by foils or crystal monochromators (Monshi et al. 2012). The most commonly used target material for single crystal diffraction is copper with CuKα radiation of 1.5418Å.

The diffracted X-rays are detected, processed and counted by scanning the sample material through 2θ range to attain all diffraction directions of the lattice due the random material orientation. The diffraction peaks are converted to d-spacings thereby allowing sample identification due to compounds having a set of unique d-spacings. The average particle size can be calculated from Debye Scherrer equation (equation **2.6**); where D is the average particle size in nm, k is the dimensionless shape factor (0.9), λ is the x-ray wavelength, β is the line broadening at full width half maximum intensity (FWHM) and θ is the Bragg's angle (peak position/2) (Monshi et al. 2012).

$$D = k\lambda / \beta \cos \theta \qquad\qquad\qquad\qquad \textbf{2.6}$$

2.7.2 Raman spectroscopy

This technique was named after Sir C.V. Raman who invented it (Joshi et al. 2008; Das & Agrawal 2011). Raman is a spectroscopic technique based on the elastic scattering of monochromatic light from a laser source. Raman spectroscopy technique is used to elucidate vibrational, rotational and other low frequency modes in a compound (Joshi et al. 2008). It gives compound fingerprint and can be used for solid, liquid and gaseous sample materials analysis. The electron cloud formed is polarized by incident photon that creates unstable excited virtual states which further stabilized when another photon is re-emitted to similar but not identical energy, phenomenon called the Raman Effect (Das & Agrawal 2011).

The Raman Effect is based on molecular polarizability (α) which determines the molecular deformations in electric field (E) (Das & Agrawal 2011; Warner & Butler 1970). the Raman scattering intensity is proportional to the magnitude of polarizability of the compound. Since Raman techniques are dependence on the polarizability of electron cloud, they can analyze vibrational/rotational transitions. At room temperature, most molecules occur in the lowest energy vibrational level.

Therefore, the energy of these states is determined by the frequency of the employed light source considering the virtual states are not real states of the molecules though made during electrons and laser interactions which causes polarization (Nakamoto & Brown 2003). Due to similar scatter of photons, the Rayleigh process becomes the most intense process because light returns to the same energy state since it does not involve energy change.

Stokes scattering results from absorption of energy by molecule from the ground vibrational state *m* and promoted to a higher energy excited vibrational state (*n*) during Raman scattering process (Nakamoto & Brown 2003; Das & Agrawal 2011). Inversely, energy is transferred to the scattered photon when scattering occurs from the *n* states to the ground state *m* during a process called anti-stokes scattering.

A shift in energy from the laser beam energy result in Raman scattering which is only shown as the Stokes spectrum. Therefore, a difference in the laser energy and the scattered energy corresponding to ground and excited vibrational states (*n* and *m*) indicate the Raman scattering that is expressed as cm^{-1} is an energy shift from the exciting radiation energy (Das & Agrawal 2011).

2.7.3 Diffuse reflectance spectroscopy in the UV-Vis-NIR region (UV-Vis-DRS)

UV-Vis spectroscopy is an ultraviolet-visible light absorption dependent characterization technique of the electromagnetic radiation spectrum (Beale et al. n.d.; Sadeghzadeh-attar et al. 2018). The absorption region ranges from

190-700 nm of the electromagnetic radiation spectrum. The molecule electronic transitions occur in the material's absorption range of the electromagnetic radiation spectrum.

The molecule electronic transitions are measured by absorption of light from the ground state to the excited state. The absorbance of a solution of a material/sample increases when beam attenuation increases (Beale et al. n.d.). Therefore, the absorbance of a molecule is directly proportional to the path length (b), the concentration (c) of the absorbing material with the absorptivity (ε) following the Beer's Law (equation **2.7**).

$$A = \varepsilon bc \hspace{4cm} \textbf{2.7}$$

Diffuse reflectance spectroscopy is used to measure the absorption spectra of a solid material. It allows for extrapolation of the wavelength range in which the material absorbs. Therefore, size and type of band gap (direct or indirect) can be calculated based on principle of discrete energy levels corresponding to allowed electron states possessed by semiconductors (Weckhuysen 2004; Zanjanchi et al. 2006). Tauc relation equation **2.8** is then used to calculate band gap value.

$$(\alpha h\nu) = A \, (h\nu - E_g)^n \hspace{3cm} \textbf{2.8}$$

Where α – the absorption coefficient

$h\nu$ – the energy of the incident radiation

A – constant based on effective mass of electrons and holes

n – band gap transitions (direct, 0.5 or indirect, 2)

E_g – band gap of the semiconductor

2.7.4 Transmission electron microscopy

TEM is a characterization technique used to identify the morphology/shape of the nanoparticles or thin films such as metals, polymers, alloys, semiconductors and

composite materials (Zablotskii et al. 2013; Zhao & Yang 2010). TEM fields of applications include cancer research, virology and material sciences. It produces images when beam of electrons is transmitted on the sample (Joshi et al. 2008; Brillson 2016).

The generated image is constructed on the photographic film or charge-coupled device (CCD) after sample and beam interaction and refraction around atoms (Abudayyeh 2014). Therefore, the information about the sample surface morphology is revealed. The nano-scale surface dopants such as metallic and/or crystalline elements can also be detected using TEM. This is because electron microscopes are capable of higher resolution imaging due to small de Broglie wavelength of electrons (Nanocomposix 2012).

Available tool on TEM is surface area electron diffraction (SAED) which is used to visualize electron diffraction rings or spots corresponding to certain crystal polymorph (Joshi et al. 2008). The diffraction rings or spots obtained using SAED can be used in conjunction with X-ray diffraction spectroscopy (XRD) results as it is possible to correlate the ring size with known d-spacing of the crystal polymorph. The SAED image can further be processed in diffraction rings or spots identifier software such as Crystbox to identify the crystal planes corresponding to the diffraction rings or spots.

2.7.5 Scanning electron microscopy

SEM is one of the most versatile techniques used for microstructure morphology and chemical composition of material characterization (Joshi et al. 2008). It is used to study the surface morphology of the materials such as semiconductor photocatalyst and membranes, together with their size. SEM is an electron microscope which acquires images by scanning the signals produced from interactions between an electron beam and the sample specimen.

In the instrument, the interaction of the emitted high energy electron beam with the surface of the sample that emits counter (secondary) electrons that are captured by detectors and then transformed into an image. Either backscattering and/or diffraction backscattering results from the electrons emitted by the sample. Despite an image being two dimensional, a three-dimensional image results from the electrons (Martin 2015; Joshi et al. 2008).

Energy dispersive X-ray spectroscopy (EDS) is a tool found in both SEM and TEM instruments for analyzing elements in the samples. It results in a spectrum of elements found in the sample and their ratios. The electron beams are used to excite electrons in the ground state in the sample and then are ejected, occurs both in SEM and TEM. Therefore, an electron from a higher shell fills a vacant in the ground state during a de-excitation process which results in an X-ray being emitted. The emitted X-ray is of energy equal to the difference between the two shells which is characteristic of individual elements (Joshi et al. 2008).

2.7.6 Photoluminescence spectroscopy

Photoluminescence spectroscopy is a non-destructive and contactless method to examine the electronic structure of materials. When the sample is subjected to light source in the instrument, it absorbs and imparts excess energy into the material during a process called photoexcitation (Kanellopoulos 2011). The energy can be dissipated by the sample through the emission of light, which is termed luminescence. In the case of photoexcitation, this luminescence is called photoluminescence.

Photoexcitation causes electrons to move into a permissible excited state in the material. The electrons later return to the equilibrium states, whereby the excitation energy is released which may or may not include radiative or non-radiative processes of the emission of light (**Figure 2.12**) (Wu et al. 2014). The emitted light energy (photoluminescence) is related to the difference in energy levels between

the excited and equilibrium electron states involved in the transition. The amount of the emitted light is related to the radiative process relative contributions.
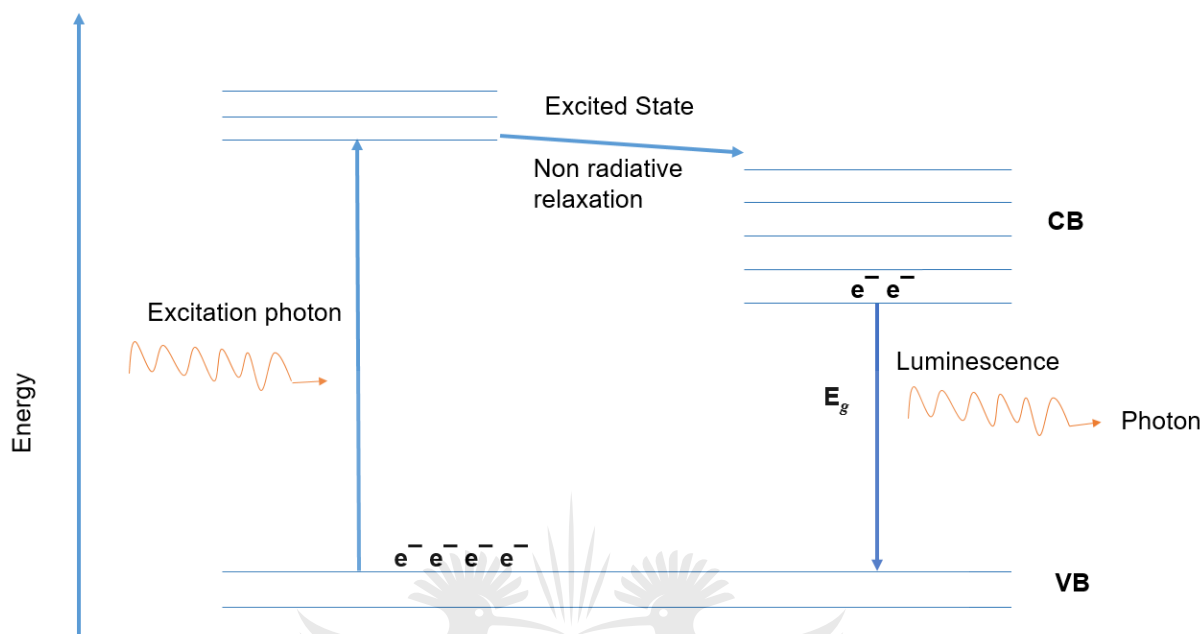
Figure 2.13: A schematic representation for the mechanism in photoluminescence (Wu et al. 2014).

An emission spectrum is produced when the excitation wavelength is fixed, and the emitted radiation is scanned. This occurs by selecting excitation wavelength by one monochromator and luminescence observed through the second monochromator positioned at 90 ºC to the incident light to minimize the intensity of the scattered light reaching the detector. Therefore, the spectral distribution of the PL from a semiconductor can be analyzed to determine non-destructively the material's electronic band gap. Furthermore, concentration of local defects may be quantified from the photoluminescence energy associated with those local defects.

2.7.7 Electrochemical Impedance Spectroscopy (EIS)

The electrochemical impedance spectroscopy is a powerful technique to study the electrochemical reactions. The impedance spectroscopy (IS) is divided into two

categories namely, electrochemical IS and dielectric IS based on the material, device, or system under study (Scribner Associates n.d.; Stoynov et al. 2009).

Dielectric IS involving the analysis of dielectric materials with mainly electronic conduction and electrochemical IS applies to materials with prevalent ionic conduction on the electronic one. Such systems are solid and liquid electrolytes, glasses and polymers. This technique has been largely employed in the study of corrosion or electrochemical and photoelectrochemical cells such as fuel cells, batteries or solar devices (Miguel et al. 2019).

The EIS measurements are based on the application of AC voltage (or current, such as in galvanostatic EIS) to the system under study and on the AC current (voltage) analysis response as a function of frequency (Scribner Associates n.d.). The potentiostat and frequency response analyzers (FRA) are usually used to carry such measurements, either in 2- or 3-electrodes configuration. The electrodes configurations depend on the absence (2-electrodes) or the presence (3-electrodes) of a reference electrode (Stoynov et al. 2009). The reference electrode has known and fixed potential.

2.7.8 Surface area, pore size and pore volume determination (BET)

The surface area, pore volume and pore size of a material are widely measured using gas adsorption measurements techniques (Sing & Williams 2004). This is because most applications such as gas sensing and photodegradation of organic compounds are processes that occur on the surface of the material. To obtain these measurements, a standard method for surface area measurements called the Brunauer-Emmett-Teller (BET) theory is used (Sing 2001; Sing 2004).

The BET theory describes the physisorption of the gas molecules on the surface of a solid material which results from the weak van der Waals forces. This theory was adapted from the Langmuir theory which describes the monolayer adsorption of a

gas on a solid material by extending the concept to allow multilayer adsorption calculated using equation **2.9** (Cui 2005.).

$$\frac{1}{v_a\left[\left(P^0 \div P\right)-1\right]} = \frac{(c-1)}{v_m c}\left(\frac{p}{p^0}\right) + \frac{1}{v_m c}$$

2.9

Where v_α is the volume of the gas adsorbed at standard temperature and pressure (STP), p and p^0 are the partial vapor pressure and saturation pressure of the physisorbed gas (often N_2), c is the BET constant and v_m is the adsorbed gas quantity per volume to produce a monolayer. The BET constant is described by equation **2.10**:

$$c = e^{\frac{(E_1 - E_L)}{RT}}$$

2.10

Where E_1 is the first layer's heat of adsorption and E_L is the corresponding heat of adsorption for n layers > 1. Therefore, the BET specific surface area (S_{BET}) is given by equation **2.11**:

$$S_{BET} = a\left(\frac{v_m N_A s}{V}\right)$$

2.11

Whereby, *a* is the mass of the powdered adsorbent, N_A is the Avogadro's number, *S* is the adsorption cross section of the powder and *V* is the molar volume gas (Cui 2005).

2.7.9 Thermogravimetric analysis (TGA)

Thermos-gravimetric analysis (TGA) is an important analytical technique for determining compound's characteristic changes under varying temperatures. It is most important for phase changes and condensation reactions in polymers

(Peterson et al. 2001; Gai et al. 2013). This technique monitors the mass of the sample as a function of temperature or time by subjecting the sample specimen to a controlled temperature program in a controlled atmosphere.

TGA is used to monitors the mass of a solid or liquid material over temperature with high precision by measuring the mass difference due to evaporation or sublimation. The data obtained can then be plotted on a simple x-y curve; mass (as a percentage) versus temperature or time. Perkin Elmer (2010) explained that TGA constitutes of different compartments which are a sample pan that is supported by a precision balance in a furnace which is heated and cooled during the experiment (Perkin Elmer 1960).

During the experiment, the sample mass is monitored while a gas is purged through the sample to control the sample environment. The gas may be inert or a reactive gas that flows over the sample and exits through an exhaust. The mass loss may be due to processes such as degradation and/or decomposition, vaporization of bulk liquids or liquids adsorbed by solids, sublimation, reduction of metal oxides to metals, and decomposition of gases. On a contrary, mass gain may be due to adsorption of gases, reaction of solids with reactive gases such as oxygen, chlorine and carbon monoxide (Peterson et al. 2001).

2.7.10 Electrophoretic light scattering (ELS)

The zeta potential value gives idea about the stability of the colloids and the degree of repulsion that exists between adjacent particles of the same charge (De Kanter et al. 2016). Zeta potential is a potential at a theoretical boundary surrounding the electrical double layer within which the liquid moves together with the particles. The electrokinetic properties therefore exists which are determined by an electrical charge distribution due to the electrical double layer surrounding the particle (Malvern Instruments n.d.). This happens when the particle is immersed in an electrolyte such as water, whereby an ionic particle becomes surrounded by counter ions with a positive to that at the surface.

The zeta potential is determined by the measurement of an electrokinetic effects observed when two phases (solid and liquid) move relative to each other achieved using micro-electrophoresis in conjunction with electrophoretic light scattering (Malvern Instruments n.d.). A specialized cuvette-type cell is used to hold the particle-electrolyte solution which is subjected to an applied oscillating electric field which causes the particles to move with velocity proportional to their zeta potential.

The velocity is then measured by passing a laser beam through the cell, and the Doppler shift frequency observed is proportional to the dispersed particle's mobility (Zhu et al. 2014). Upon determination of electrophoretic mobility by electrophoretic light scattering, the Smoluchowski equation **2.12** is employed to convert the obtained EPMs to zeta potential (Lin et al. 2009; Zhu et al. 2014). The Smoluchowski equation is defined as follows:

$$\mu = \frac{\varepsilon \zeta}{\eta}$$ **2.12**

Where μ is the electrophoretic mobility, ε is the dielectric constant of the solution, η, ζ is the viscosity and the zeta potential respectively.

2.7.11 Fourier transform infrared spectroscopy (FTIR)

This is an important spectroscopic characterization technique for detection and fingerprinting of covalent bonds and to check the presence of impurities and contaminants on the semiconductor photocatalysts surfaces (Series 2010). Though it is normally achieved using the infrared spectroscopy. It is used for chemical compound identification in variety of products including polymers, paints, consumer products, pharmaceuticals and foods.

It is easy to detect organic contaminants due to their intrinsic molecular complex (Haug et al. 2011). Though, photocatalysts pose few IR-active bonds because they are mainly crystalline consisting of simple molecular structures. Although, molecules that possess change associated with dipole moments because of vibration are IR active.

FTIR possess abilities such as easy to use and understand and fast sampling, though its signal to noise ratio is high. FTIR analysis uses polychromatic light source and the beams first pass through Michelson interferometer splitting device (Joshi et al. 2008; Rosen et al. 2009). This results in a deliberate path shift followed by detector illumination after mixed interference beam of all wavelengths hit the sample. Beam retardation is caused by the moving mirror with real units within the interferometer.

Therefore, the detector produces an interferometer; a fixed set of retardation values and a corresponding set of intensities. The position of the intensity of the absorption bands of a sample are exceptionally specific for a substance and can be used as a highly characteristic "fingerprint" for identification of photocatalysts (Rosen et al. 2009).

2.7.12 Liquid Chromatography-Mass spectroscopy (LC-MS)

LC-MS is a coupled analytical technique used exclusively for the detection and structure elucidation of metabolites (Traldi et al. 2018). This arise from the all-time desire to couple MS and chromatographic techniques due to the sensitive and highly specific nature of MS compared to other chromatographic detectors. It was obvious to couple MS and LC, but there was no progress in the development for many years due to relative incompatibility of the existing MS ion sources with a continuous liquid stream (Pitt 2009).

LC-MS own advantages such as high specificity and the ability to handle complex mixtures. Most of LC-MS instruments are fitted with electron spray ion source in the MS compartment.

The mass spectrometers operation involves the conversion of the analyte molecule to a charged (ionized) state, therefore the ions and any other fragments ions produced during ionization process are analyzed based on their mass to charge ration (m/z) (Richardson & Postigo 2018). Different technologies are available for both ionization and ion analysis. Due to the versatility of some configurations the processes major types of ion sources and mass analyzers which are likely to be used in LC-MS systems have been developed and identified.

Ion sources such as electrospray ionization (ESI), atmospheric pressure chemical ionization (APCI), and atmospheric pressure photo-ionization (APPI) have been found to be compatible in the LC-MS (Pitt 2009). Amongst them, electrospray ionization sources demonstrated its capability for LC interface and application to several important classes of biological molecules. It works well with moderately polar molecules and suited for many metabolites and xenobiotics analysis.

Liquid samples are pumped through a metal capillary maintained at 3 to 5 kV and nebulized at the tip of the capillary to form a fine spray of charged droplets (Pitt 2009). To minimize contamination, the capillary is placed orthogonal to, or off-axis from the entrance to the mass spectrometer. Under the application of heat and dry nitrogen, rapid evaporation of droplets occurs, and the residual electrical charge on the droplets is transferred to the analyte. Therefore, the ionized analytes are then transferred into the high vacuum of the mass spectrometer. The ion source and the subsequent ion optics are operated to detect either positive or negative ions and switching between the two modes within an analytical run (Richardson & Postigo 2018).

MS can be fitted with mass analyzers such as quadrupole, time-of-flight (TOF), hybrid, and ion trap analyzers. Quadrupole analyzers are the common mass analyzers used in GC-MS and LC-MS (Pitt 2009). Quadrupole analyzers operates

at <4000 *m/z* and scan speed of up to 1000 *m/z* per second. They can be set to monitor a specific *m/z* value by stepping the voltages.

Therefore, this technique improves the detection limit of targeted analytes due to more detector time. The ions under collision induced dissociation which is ion fragmentation by collision with inert gas such as argon or nitrogen in a collision cell (Traldi et al. 2018). There are 4 quadrupole analyzers in an MS which the first and third can be simultaneously stepped to different *m/z* values and panels of the precursor/product ion pairs can be created to specifically detect many target analytes in a process called multiple reaction monitoring (MRM) commonly used in LC-MS (Richardson & Postigo 2018; Pitt 2009).

The LC compartment is also a huge participator in the LC-MS application. This is because there are many factors involved in the LC operation that can affect the quality of the MS data. Those factors include the flow rate, mobile phase, resolution and through-put (Pitt 2009). These factors when set to the system optimum operation they yield better results.

2.8 Conclusion

Pollutants (organic, microbial, and humus) has been a concern to the environment due to their effects especially in water systems. This arise from their frequent detection in the environment at high levels, endangering life. These pollutants according to their classes have showed to affect a variety of species including human beings.

Those pollutants include organophosphate pesticides such as chlorpyrifos widely used in agricultural activities. The effects of chlorpyrifos range from skin irritations, dizziness, shortness of breath and to death at most (especially in children). Human beings mostly suffer from the effects of these pollutants directly and indirectly.

Methods of degrading these pollutants in water and wastewater have been employed. Those methods include biological (fungal and bacterial strains) and

chemical (chlorination, advanced oxidation processes) treatment. Advanced oxidation processes (AOPs) have been extensively studied for removal of pollutants in water. These processes use hydroxyl and superoxide radicals as reactive species towards pollutant degradation. Such AOPs include Fenton process and photocatalysis. Photocatalysis is the most studied advanced oxidation process, which uses a semiconductor catalyst under light irradiation. The pristine semiconductor catalysts (such as WO_3 and SnS_2) have limitations such as photogenerated charge recombination and UV light absorption. Therefore, modification to improve the photocatalytic activity of the semiconductor catalysts include doping with metal, nonmetal and another semiconductor catalyst.

Tungsten trioxide (WO_3) is a stable, visible light absorbing photocatalyst suitable for organic pollutant removal due to a more positive valence band edge. It suffers from photogenerated charge recombination. Modification using SnS_2 to form a heterojunction improve charge separation.

Methods for synthesis of these nanomaterials include sol-gel, precipitation and hydrothermal synthesis. Tungsten trioxide synthesized with hydrothermal method has illustrated efficiency towards organic pollutants degradation when doped with metal or nonmetal or another photocatalyst.

2.9 References

Abudayyeh, H. 2014. Synthesis and Analysis of ZnO Nanowires. 2012. Thesis submitted at Birzeit University. (Accessed @ https://www.researchgate.net/publication/263849645_Synthesis_and_Analysis_of_ZnO_nanowires on 20 December 2018.

Ahmadi, M., Younesi, R. & Guinel, M. J. F., 2014. Synthesis of tungsten oxide nanoparticles using a hydrothermal method at ambient pressure. *Journal of Materials Research*, 29(13), pp.1424–1430.

Alharbi, O. M. L., Basheer, A. A., Khattab, R. A. & Ali, I. 2018. Health and environmental effects of persistent organic pollutants. *Journal of Molecular Liquids*, 263, pp.442–453..

Aoki, N., Sato, A., Sasaki, H., Litwinowics, A., Seong, G., Aida, T., Hojo, D., Takami, S. & Adschiri, T. 2016. Kinetics study to identify reaction-controlled conditions for supercritical hydrothermal nanoparticle synthesis with flow-type reactors. *The Journal of Supercritical Fluids*, 110, pp.161–166.

Awofolu, O. R., Mbolekwa, Z., Mtshemla, V. & Fatoki, O. S. 2005. Levels of trace metals in water and sediment from Tyume River and its effects on an irrigated farmland. *Water SA*, 31(1), pp.87–94.

Awotiwon, O. F., Wyk, V. P., Dhansay, A., Day, C. & Bradshaw, D. 2016. Diarrhoea in children under five years of age in South Africa (1997 – 2014). *Tropical Medicine and International Health*, 21(9), pp.1060–1070.

Ayoub, K., D. van Hullebusch, E., Cassir, M. & Bermond, A. 2010. Application of advanced oxidation processes for TNT removal: A review. *Journal of Hazardous Materials*, 178(1–3), pp.10–28.

Balis, N., Zaky, A. A., Perganti, D., Kaltzoglou, A., Sygellou, L., Katsaros, F., Stergiopoulos, T., Kontos, A. G. & Falaras, P. 2018. Dye sensitization of titania compact layer for efficient and stable perovskite solar cells. *ACS Applied Energy Materials*, 1(11), pp.6161-6171.

Batzill, M., 2011. Fundamental aspects of surface engineering of transition metal oxide photocatalysts. *Energy & Environmental Science*, 4(9), pp.3275-3286.

Beale, A. M., Stavitski, E. & Weckhuysen, B. M. Characterization of Catalysts:

Surface and In-Situ Methods. *Encyclopedia of Life Support Systems (EOLSS)* @ https://www.eolss.net/Sample-Chapters/C06/E6-190-13-00.pdf. Accessed 26 January 2019.

Binning, K. & Baird, D. 2001. Survey of heavy metals in the sediments of the Swartkops River Estuary, Port Elizabeth South Africa. *Water SA*, 27(4), pp.461–466.

Brillson, L. J. 2016. *An Essential Guide to Electronic Material surface and interface*. 2nd edn. John Wiley & Sons, Ltd. Ohio State University, USA. (Accessed on 26 January 2019).

Buckley, C. & Naidoo, V. 2003. Survey of pesticide wastes in South Africa and review of treatment options. *WRC Report No. 1128/1/03*. Water Research Commission Pretoria, South Africa. (Accessed on 26 January 2019).

Burton, L. A. Whittles, T. J., Hesp, D., Linhart, W. M., Skelton, J. M., Hou, B., Webster, R. F., O'Dowd, G., Reece, C., Chems, D., Fermin, D. J., Veal, T. D., Dhanak, V. R. & Walsh, A. 2016. Electronic and optical properties of single crystal SnS_2: An earth-abundant disulfide photocatalyst. *Journal of Material Chemistry. A*, 4, pp.1312–1318.

Chae, S. Y., Lee, C. S., Jung, H., Joo, O., Min, B. K., Kim, J. H. & Hwang, Y. J. 2017. Insight into charge separation in $WO_3/BiVO_4$ heterojunction for solar water splitting. *ACS Applied Materials & Interface*, 9(23), pp.19780-19790.

Chen, S., Liu, C., Peng, C., Liu, H., Hu, M. & Zhong, G. 2012. Biodegradation of chlorpyrifos and its hydrolysis product 3,5,6-trichloro-2-pyridinol by a new Fungal Strain *Cladosporium cladosporioides* Hu-01. *PLoS ONE*, 7(10), pp.1–12.

Chen, S., Chen, M., Wang, Z., Qiu, W., Wang, J., Shen, Y., Wang, Y. & Ge, S. 2016. Toxicological effects of chlorpyrifos on growth, enzyme activity and chlorophyll a synthesis of freshwater microalgae. *Environmental Toxicology and Pharmacology*, 45, pp.179–186.

Chowdhury, P., Malekshoar, G. & Ray, A. K. 2017. Dye-Sensitized Photocatalytic Water Splitting and Sacrificial Hydrogen Generation: Current Status and Future Prospects. *Inorganics*, 5(2), pp.34.

Christoforidis, K. C., Sengele, A., Keller, V. & Keller, N. 2015. Single-step synthesis of SnS_2 nanosheet-decorated TiO_2 anatase nanofibers as efficient

photocatalysts for the degradation of gas-phase diethylsulfide. *ACS Applied Materials and Interfaces*, 7(34), pp.19324–19334.

Cui, H. 2005. Preparation and characterization of optical multilayered coatings for smart windows applications @ http://www.repositorium.sdum.uminho.pt/bitstream/1822/3341/7/Chapter9-ECD-Conclusion.pdf Accessed on 16 August 2018.

Danks, A. E., Hall, S. R. & Schnepp, Z. 2016. The evolution of 'sol-gel' chemistry as a technique for materials synthesis. *Materials Horisons*, 3, pp.91–112.

Das, R., Ali, Md. E. & Hamid, Sh. B. A. 2014. Current applications of x-ray powder diffraction. *Reviews on Advanced Material Science*, 38(2), pp.95-109.

Das, R. S. & Agrawal, Y. K. 2011. Vibrational Spectroscopy Raman spectroscopy : Recent advancements, techniques and applications. *Vibrational Spectroscopy*, 57(2), pp.163–176.

De Kanter, M., Meyer-Kirschner, J., Viell, J., Mitsos, A., Kather, M., Pich, A. Janzen, C. 2016. Enabling the measurement of particle sizes in stirred colloidal suspensions by embedding dynamic light scattering into an automated probe head. *Measurement*, 80, pp.92–98.

Department of Water Affairs (DWA). 2011. Directorate Water Resource Planning Systems: Water Quality Planning. Resource Directed Management of Water Quality. *Planning Level Review of Water Quality in South Africa*. Sub-series No. WOP 2.0. Pretoria, South Africa. (Accessed on 26 January 2019).

Dimitriev, Y., Iordanova, R., Mancheva, M. & Klissurski, D. 2005. Preparation of nanocrystalline WO_3 and MoO_3 by different Sol – Gel methods. *Chemistry for sustainable development,* 13, pp.185–189.

Dong, H., Zeng, G., Tang, L., Fan, C., Zhang, C., He, X. He, Y. 2015. An overview on limitations of TiO_2 -based particles for photocatalytic degradation of organic pollutants and the corresponding countermeasures. *Water Research*, 79, pp.128–146.

Du, W., Deng, D., Han, Z., Xiao, W., Bian, C. & Qian, X. 2011. Hexagonal tin disulfide nanoplatelets: A new photocatalyst driven by solar light. *Crystallography, Engineering and Communication*, 13(6), pp.2071–2076.

EAP Task Force. 2007. Surface Water Quality Regulation in EECCA Countries: Directions for Reform. *Europe's Environment: The Fourth Assessment,*

European Environmental Agency, Copenhagen, pp.1–13.

Edokpayi, J. N., Odiyo, J. O., Popoola, O. E. & Msangati, T. A. 2016. Assessment of trace metals contamination of surface water and sediment: A case study of Mvudi River, South Africa. *Sustainability*, 8, pp.135–148.

El Masri, A., Al Rashidi, M., Laversin, H., Chakir, A. & Roth, E. 2014. A mechanistic and kinetic study of the heterogeneous degradation of chlorpyrifos and chlorpyrifos oxon under the influence of atmospheric oxidants: ozone and OH$^-$ radicals. *RSC Advances*, 4, pp.24786–24795.

Fadaei, A. & Kargar, M. 2013. Photocatalytic degradation of chlorpyrifos in water using titanium dioxide ad zinc oxide. *Fresenius Environmental Bulletin*, 22(8), pp.2442–2447.

Fakhri, A. & Behrouz, S. 2015a. Assessment of SnS_2 nanoparticles properties for photocatalytic and antibacterial applications. *Solar Energy*, 117, pp.187–191.

Fakhri, A. & Behrouz, S. 2015b. Photocatalytic properties of tungsten trioxide (WO_3) nanoparticles for degradation of Lidocaine under visible and sunlight irradiation. *Solar Energy*, 112, pp.163–168.

Fan, S., Li, K., Yan, Y., Wang, J., Wang, J., Qiao, C., Yang, T., Jia, Y. & Zhao, B. 2018. A novel chlorpyrifos hydrolase CPD from *Paracoccus sp.* TRP: Molecular cloning, characterization and catalytic mechanism. *Electronic Journal of Biotechnology*, 31, pp.10–16.

Fang, B., Li, J. W., Zhang, M., Ren, F. Z. & Pang, G. F. 2018. Chronic chlorpyrifos exposure elicits diet-specific effects on metabolism and the gut microbiome in rats. *Food and Chemical Toxicology*, 111(11), pp.144–152.

Fatoki, O. S. & Awofolu, R. 2003. Levels of Cd, Hg and Zn in some surface waters from the Eastern Cape Province, South Africa. *Water SA*, 29(4), pp.375–380.

Ferraro, J. R., Nakamoto, K. & Brown, C.W. 2003. *Introductory Raman Spectroscopy*, 2nd edn, Elsevier. (Accessed on 30 October 2018).

Fu, X., Cai, J., Zhang, X., Li, W., Ge, H. & Hu, Y. 2018. Top-down fabrication of shape-controlled, monodisperse nanoparticles for biomedical applications ☆. *Advanced Drug Delivery Reviews*, 132, pp.169-187.

Gai, C., Zhang, Y., Chen, W., Zhang, P. & Dong, Y. 2013. Thermogravimetric and kinetic analysis of thermal decomposition characteristics of low-lipid microalgae. *Bioresource Technology*, 150, pp.139–148.

Georgaki, I. V. I., Kenanakis, D. V. G. & Katsarakis, N. 2015. Synthesis of WO_3 catalytic powders: evaluation of photocatalytic activity under NUV/visible light irradiation and alkaline reaction pH. *Journal of Sol-Gel Science and Technology*, 76(1), pp.120-128.

Glynnis, R., Perry, M., Lee, M. M., Hoffman, E., Delport, S. & Dalvie, M. A. 2012. Farm residence and reproductive health among boys in rural South Africa. *Environment International*, 47, pp.73–79.

Gupta, V. K., Eren, T., Atar, N., Yola, M. L., Parlak, C. & Karimi-Maleh, H. 2015. $CoFe_2O_4$@TiO_2 decorated reduced graphene oxide nanocomposite for photocatalytic degradation of chlorpyrifos. *Journal of Molecular Liquids*, 208, pp.122–129.

Hamilton, D. J., Ambrus, A., Dieterle, R. M., Felsot, A. S., Harris, C. A., Holland, P. T., Katayama, A., Kurihara, N., Linders, J., Unsworth, J. & Wong, S. S. 2003. Regulatory limits for pesticide residues in water (IUPAC Technical Report). *Pure Applied Chemistry*, 75(8), pp.1123–1155.

Haug, A., Hiesgen, R., Schulze, M., Schiller, G. & Friedrich, K. A. 2011. Fourier transform infrared spectroscopy from: PEM fuel cell diagnostic tools. *CRC Press*. (Accessed on 06 December 2018 on https://www.routledgehandbooks.com/doi/10.1201/b11100-20).

Hayashi, H. & Hakuta, Y., 2010. Hydrothermal synthesis of metal oxide nanoparticles in supercritical water. *Materials*, 3, pp.3794–3817.

Hill, J. M., Motitsoe, S. N. & Hill, M. P. 2015. Pollution mapping in freshwater systems: using aquatic plants to trace N-Loading. *WRC Report No.2262/1/15.* Water Research Commission Pretoria, South Africa. (Accessed 30 September 2018).

Hou, J., Zhang, F., Wang, P., Wang, C., Chen, J., Xu, Y., You, G., Zhou, Q. & Li, Z. 2018. Enhanced anaerobic biological treatment of chlorpyrifos in farmland drainage with zero valent iron. *Chemical Engineering Journal*, 336, pp.352–360.

Ishag, A. E. S. A., Abdelbagi, A. O., Hammad, A. M. A., Elsheikh, E. A. E., Elsaid, O. E., Hur, J. H. & Laing, M. D. 2016. Biodegradation of chlorpyrifos, malathion, and dimethoate by three strains of bacteria isolated from pesticide-polluted soils in Sudan. *Journal of Agricultural and Food Chemistry*, 64, pp.8491-8498.

Islam, S. Z., Nagpure, S., Kim, D. Y. & Rankin, S. E. 2017. Synthesis and catalytic applications of non-metal doped mesoporous titania. *Inorganics*, 5(15), pp.1–43.

Jamieson, A. J., Malkocs, T., Piertney, S. B., Fujii, T. & Zhang, Z. 2017. Bioaccumulation of persistent organic pollutants in the deepest ocean fauna. *Nature Ecology & Evolution*, 1, pp.51.

Jenkins, R. 2000. X-ray Techniques: Overview. *Encyclopedia of Analytical Chemistry*, R. A. Meyers (Ed), pp.13269–13288.

John, E. M. & Shaike, J. M. 2015. Chlorpyrifos: pollution and remediation. *Environmental Chemistry Letters*, 13(3), pp.269–291.

Joshi, M., Bhattacharyya, A. & Ali, S. W. 2008. Characterization techniques for nanotechnology applications in textiles. *Indian Journal of Fibre & Textile Research*, 33, pp.304–317.

Kanellopous, N. 2011. Nanoporous Materials: Advanced technologies for characterization, modelling, and processing. *CRC press*, New York. (Accessed on 30 September 2018).

Khan, S. H., Suriyaprabha, R., Pathak, B. & Fulekar, M. H. 2015. Photocatalytic degradation of organophosphate pesticides (Chlorpyrifos) using synthesized zinc oxide nanoparticle by membrane filtration reactor under UV irradiation. *Frontiers in Nanoscience and Nanotechnology*, 1(1), pp.23–27.

Khanjani, S. & Morsali, A. 2010. Synthesis and characterization of lanthanum oxide nanoparticles from thermolysis of nanostructured supramolecular compound. *Journal of Molecular Liquids*, 153(2–3), pp.129–132.

Kharagpur Web Course. Module 10: Classification of water pollutants and effects on environment. *NPTEL IIT Kharagpur Web Course*, pp.1–7. (Accessed on 20 October 2018).

Kim, J., Kim, J., Yoon, S., Kang, J., Jeon, C. & Jo, W. 2018. Single phase formation of SnS competing with SnS$_2$ and Sn$_2$S$_3$ for photovoltaic applications: Optoelectronic characteristics of Thin- Film surfaces and interfaces. *Journal of Physical Chemistry C*, 122(6), pp.3523-3532.

Kominami, H., Yabutani, K., Yamamoto, T., Kera, Y. & Ohtani, B. 2001. Synthesis of highly active tungsten (VI) oxide photocatalysts for oxygen evolution by hydrothermal treatment of aqueous tungstic acid solutions. *Journal of Materials*

Chemistry, 11, pp.3222–3227.

Kravvariti, K., Tsiropoulos, N. G. & Karpouzas, D. G. 2010. Degradation and adsorption of terbuthylazine and chlorpyrifos in biobed biomixtures from composted cotton crop residues. *Pesticide Management Science*, 66, pp.1122–1128.

Kuzmin, A. & Purans, J. 1998. X-ray diffraction, extended x-ray absorption fine structure and Raman spectroscopy studies of WO_3 powders and $(1- x)WO_{3-y}\bullet xReO_2$ mixtures. *Journal of Applied Physics*, 84(10), pp.5515-5524.

Li, J., Du, X., Yao, L. & Zhang, Y. 2014. Synthesis of SnS_2/WO_3 nanocomposite with enhanced photocatalytic activity. *Materials Letters*, 121, pp.44–46.

Li, X., Yu, J., Low, J., Fang, Y., Xiao, J. & Chen, X. 2015. Engineering heterogeneous semiconductors for solar water splitting. *Journal of Materials Chemistry A*, 3, pp.2485–2534.

Lim, L. & Bolstad, H. M. 2018. Organophosphate Insecticides: Neurodevelopmental Effects. *2nd edn. Elsevier Inc.* United States. (Accessed on 20 October 2018).

Lin, D., Liu, N., Yang., K., Zhu., L., Xu, Y. & Xing, B. 2009. The effect of ionic strength and pH on the stability of tannic acid-facilitated carbon nanotube suspensions. *Carbon*, 47(12), pp.2875–2882.

Liu, G., Yu, J. C., Lu, G. Q. & Cheng, H. 2011. Crystal facet engineering of semiconductor photocatalysts: motivations, advances and unique properties. *Chemical communications*, 47(24), pp.6763–6783.

Liu, J., Tan, L., Wang, J., Wang, Z., Ni, H. & Li, L. 2016. Complete biodegradation of chlorpyrifos by engineered *Pseudomonas putida* cells expressing surface-immobilized laccases. *Chemosphere*, 157, pp.200–207.

Liu, Y., Mai, S., Li, N., Yiu, C. K. Y., Mao, J., Pashley, D. & Tay, F. R. 2011. Differences between top-down and bottom-up approaches in mineralizing thick, partially demineralized collagen scaffolds. *Acta Biomaterialia*, 7(4), pp.1742–1751.

Lockwood, D. 2017. Persistent organic pollutants, made by nature. *Journal of Chemical & Engineering News Global Enterprise*, 95(42), pp.13–15.

Luévano-hipólito, E., Martinez-de la Cruz, A., Yu, Q. L. & Brouwers, H. J. H. 2014. Precipitation synthesis of WO_3 for NO_x removal using PEG as template. *Ceramics International*, 40, pp.12123–12128.

Luo, B., Hu, Y., Zhu, X., Qiu, T., Zhi, L., Xiao, M., Zhang, H., Zou, M., Cao, A. & Wang, L. 2018. Controllable growth of SnS_2 nanostructures on nanocarbon surfaces for lithium-ion and sodium-ion storage with high rate capability. *Journal of Materials Chemistry A*, 6, pp.1462–1472.

Luo, J., Zhou, X., Zhang, J. & Du, Z. 2015. Fabrication and characterization of Ag_2CO_3/SnS_2 composites with enhanced visible-light photocatalytic activity for the degradation of organic pollutants. *RSC Advances*, 5, pp.86705–86712.

Ma, C., Xu, J., Alvarado, J., Qu, B., Somerville, J., Lee, J. Y. & Meng, Y. S. 2015. Investigating the energy storage mechanism of SnS_2-rGO composite anode for advanced Na-Ion batteries. *Chemistry of Materials,* 27, pp.5633-5640.

Malvern Instruments. Zeta Potential: An introduction in 30 Minutes. *Technical note,* 2, pp.1–6.

Mamba, G., Pulgarin, C., Kiwi, J., Bensimon, M. & Rtimi, S. 2017. Synchronic coupling of Cu2O(*p*)/CuO(*n*) semiconductors leading to Norfloxacin degradation under visible light. *Journal of Catalysis*, 353, pp.133–140.

Marigoudar, S. R., Mohan, D., Nagarjuna, A. & Karthikeyan, P. 2018. Ecotoxicology and environmental safety biomarker and histopathological responses of *Lates calcarifer* on exposure to sub lethal concentrations of chlorpyrifos. *Ecotoxicology and Environmental Safety*, 148, pp.327–335.

Marschall, R. 2014. Semiconductor composites: Strategies for enhancing charge carrier separation to improve photocatalytic activity. *Advanced Functional Materials*, 24(17), pp.2421–2440.

Martin, D. J. 2015. Investigation into high efficiency visible light photocatalysts for water reduction and oxidation, *Springer Theses*, Switzerland. (Accessed on 20 October 2018).

Miguel, M. T. De., Garcia-Martin, G., Lasanta, M. I. & Pérez, F. J. 2019. Solar energy materials and solar cells electrochemical impedance spectroscopy(EIS): An efficient technique for monitoring corrosion processes in molten salt environments in CSP applications. *Solar Energy Materials and Solar Cells*, 191, pp.157–163.

Miyauchi, M., Nukui, Y., Atarashi, D. & Sakai, E. 2013. Selective Growth of *n*-Type Nanoparticles on *p*-Type Semiconductors for Z-Scheme Photocatalysis. *Applied Materials & Interfaces*, 5, pp.9770-9776.

Mohiuddin, K. M., Ogawa, Y., Zakir, H. M., Otomo, K. & Shikazono, N. 2011. Heavy metals contamination in water and sediments of an urban river in a developing country. *International Journal on Environmental Science and Technology*, 8(4), pp.723–736.

Mojsak, P., Lozowicka, B. & Kaczyński, P. 2018. Estimating acute and chronic exposure of children and adults to chlorpyrifos in fruit and vegetables based on the new, lower toxicology data. *Ecotoxicology and Environmental Safety*, 159, pp.182–189.

Momeni, M. M. 2016. Dye-sensitized solar cell and photocatalytic performance of nanocomposite photocatalyst prepared by electrochemical anodization. *Bulletin of Materials Science*, 39(6), pp.1389–1395.

Mondal, C., Ganguly, M., Pal, J., Roy, A., Jana, J. & Pal, T. 2014. Morphology controlled synthesis of SnS$_2$ nanomaterial for promoting photocatalytic reduction of aqueous Cr(VI) under visible light. *Langmuir*, 30(14), pp.4157–4164.

Monshi, A., Foroughi, M. R. & Monshi, M. R. 2012. Modified scherrer equation to estimate more accurately nano-crystallite size using XRD. *World Journal of Nano Science and Engineering*, 2, pp.154-160.

Moores, A. 2018. Bottom up, solid-phase syntheses of inorganic nanomaterials by mechanochemistry and aging. *Current Opinion in Green and Sustainable Chemistry*, 12, pp.33–37.

Nanocomposix. 2012. Transmission Electron Microscopy analysis of nanoparticles. *nanocomposix*, 1, pp.1–7.

Navarro, J. R. G., Mayence, A., Andrade, J., Lerouge, F., Chaput, F., Oleynikov, P., Bergstrom, L., Parola, S. & Pawlicka, A. 2014. WO$_3$ nanorods created by self-assembly of highly crystalline nanowires under hydrothermal conditions. *Langmuir*, 30, pp.10487-10492.

Nousiainen, A., Mikkonen, A. & Valentın, L. 2013. Introduction to Organic Contaminants in Soil: Concepts and Risks. *Handbook of Environmental Chemistry*, pp.1–30.

Okonkwo, J. O. & Mothiba, M. 2005. Physico-chemical characteristics and pollution levels of heavy metals in the rivers in Thohoyandou, South Africa. *Journal of Hydrology*, 308, pp.122–127.

Ou, J. Z. , Ge, W., Carey, B., Daeneke, T., Rotbart, A., Shan, W., Wang, Y., Fu, Z., Chrimes, A. F., Wlodarski, W., Russo, S. P., Li, Y. X. & Kalantar-zadeh, K. 2015. Physisorption-Based Charge Transfer in Two-Dimensional SnS_2 for Selective and Reversible NO_2 Gas Sensing. *ACS Nano*, 9(10), pp.10313–10323.

Parthibavarman, M. K. M. & Prabhakaran, A. K. S. 2017. One-step microwave synthesis of pure and Mn doped nanoparticles and its structural, optical and electrochemical properties. *Journal of Materials Science: Materials in Electronics*, 28(9), pp.6635–6642.

Perkin Elmer. 1960. Thermogravimetric Analysis (TGA): A Beginner's Guide. Perkin Elmer, Inc, USA. (Accessed on 30 September 2018).

Peterson, J. D., Vyazovkin, S. & Wight, C. A. 2001. Kinetics of the Thermal and Thermo-Oxidative Degradation of Polystyrene, Polyethylene and Poly (propylene). *Macromolecular Chemistry and Physics,* 202, pp.775–784.

Pitt, J. J. 2009. Principles and applications of Liquid Chromatography-Mass Spectrometry in clinical biochemistry. *Clinical Biochemistry Reviews*, 30, pp.19–34.

Prentice, D., Pantoya, M. L. & Gash, A. E. 2006. Combustion wave speeds of sol-gel-synthesized tungsten trioxide and nano-aluminum: The effect of impurities on flame propagation. *Energy and Fuels,* 20(6), pp.2370–2376.

Quintana, M. M., Osimani, V. R., Magnarelli, G., Rovedatti, M. G. & Guinazu, N. 2018. The insecticides chlorpyrifos and acetamiprid induce redox imbalance in umbilical cord blood erythrocytes in vitro. *Pesticide Biochemistry and Physiology*, 148, pp.87–92.

Quiroz, M. A., Bandala, E. R. & Martínez-huitle, C. A. 2011. Advanced Oxidation Processes (AOPs) for Removal of Pesticides from Aqueous Media. Pesticides -Formulations, Effects, Fate, Prof. Margarita Stoytcheva (Ed.). InTech, Available from: http://www.intechopen.com/books/pesticides-formulations-effects-fate/advanced-oxidation-processes-aops-for-removal-of-pesticides-from-aqueous-media

Radulescu, C., Dulama., L. D., Stihi, C., Ionita, I., Chilian, A., Necula, C. & Chelarescu, E. D., 2014. Determination of heavy metal levels in water and therapeutic mud by atomic absorption spectrometry. *Romanian Journal of Physics*, 59(9-10), pp.1057–1066.

Rahimnejad, S., He, J. H., Chen, W., Wu, K. & Xu, G. Q. 2014. Tuning the electronic and structural properties of WO$_3$ nanocrystals by varying transition metal tungstate precursors. *RSC Advances*, 4(107), pp.62423–62429.

Raj, G. A. G., Kanmoni, V. G. G. & Daniel, S. 2012. Photocatalytic degradation of chlorpyrifos in aqueous suspensions using nanocrystals of ZnO and TiO$_2$. *Reaction Kinetics, Mechanisms and Catalysis*, 106(2), pp.325–339.

Ran, J., Zhang, J., Yu, J., Jaroniec M. & Qiao, S. Z. 2013. Earth-abundant cocatalysts for semiconductor-based photocatalytic water splitting. *Chemical Society Reviews,* 00, pp.1–26.

Richardson, S. D. & Postigo, C. 2018. Liquid Chromatography - Mass Spectrometry of Emerging Disinfection By-products. *Comprehensive Analytical Chemistry,* 79, pp.267-295.

Rodríguez-Peréz, M., Oskam, G., Rodríguez-Gattorno, G. & Chacón, C. 2015. Synthesis and characterization of WO$_3$ polymorphs: monoclinic, orthorhombic and hexagonal structures. *Journal of Materials Science: Materials in Electronics*, 26(8), pp.5526–5531.

Rosen, P., Vogel, H., Cunningham, L., Reuss, N., Conley, D. & Persson, P. 2009. Fourier transform infrared spectroscopy: Rapid, quantitative analysis of biogeochemical properties of lake sediments. *Pages news*, 17(3), pp.98-100.

Sadeghzadeh-attar, A., Akhavan-Safaei, L. & Bafandeh, M. R. 2018. UV-visible absorption and photoluminescence characteristics of SnO$_2$ nano-tube/wire arrays fabricated by LPD method. *Applied Ceramic Technology*, 15, pp.1084–1094.

Saini, R. & Kumar, P. 2016. Optimization of chlorpyrifos degradation by Fenton oxidation using CCD and ANFIS computing technique. *Biochemical Pharmacology*, 4(3), pp.2952–2963.

Samet, Y., Hmani, E. & Abdelhédi, R. 2012. Fenton and solar photo-Fenton processes for the removal of chlorpyrifos insecticide in wastewater. *Water SA*, 38(4), pp.537–542.

Saravanan, P., Gopalan, R. & Chandrasekaran, V. 2008. Synthesis and characterisation of nanomaterials synthesis and characterisation of nanomaterials. *Defense Science Journal*, 58(4), pp.504-516.

Scribner Associates. Electrochemical Impedance Spectroscopy (EIS): A powerful

and cost-effective tool for fuel cell diagnostics. *Scribner Associates-Tutorial*, pp.1–5. (Accessed on 30 September 2018).

Series, G. W. 2010. Fourier Transform Infrared Spectroscopy. *Optica Acta: International Journal of Optics*, 29(9), pp.1188-1188.

Sharma, R. K, Kumar, D. & Ghose, R. 2016. Synthesis of nanocrystalline ZnO – NiO mixed metal oxide powder by homogeneous precipitation method. *Ceramics International*, 42, pp.4090–4098.

Simelane, S., Ngila, J. C. & Dlamini, L. N. 2017. The effect of humic acid on the stability and aggregation kinetics of WO_3 nanoparticles. *Particulate Science and Technology*, 35(6), pp.632-642.

Simonsen, M. E. & Søgaard, E. G. 2010. Sol – gel reactions of titanium alkoxides and water: influence of pH and alkoxy group on cluster formation and properties of the resulting products. *Journal of Sol-Gel Science and Technology*, 53(3), pp.485–497.

Sing, K. 2001. The use of nitrogen adsorption for the characterisation of porous materials. *Colloids and Surfaces A: Physicochemical and Engineering Aspects*, 187-188, pp.3–9.

Sing, K. S. W. 2004. Characterization of porous materials: past, present and future. *Colloids and Surfaces A: Physicochemical and Engineering Aspects*, 241, pp.3–7.

Sing, K. S. W. & Williams, R. T. 2004. Physisorption hysteresis loops and the characterization of nanoporous materials. *Adsorption Science & Technology*, 22(10), pp.773–782.

Songca, S. P., Seteni, B. & Oluwafemi, O. S. 2013. Heavy metals found at Umzimvubu River Estuary in the Eastern Cape, South Africa. *African Journal of Environmental Science and Technology*, 7(5), pp.236–244.

Srivastava, A. K., Agnihotry, S. A. & Deepa, M. 2006. Sol-gel derived tungsten oxide films with pseudocubic triclinic nanorods and nanoparticles. *Thin Solid Films*, 515(4), pp.1419–1423.

Stocking, A., Kommineni, S., Zoeckler, J., Liang, S., Flores, A. & Kavanaugh, M. 3.0 Advanced Oxidation Processes. *Literature Review.* pp.109-208. (Accessed on 30 September 2018).

Stoynov, Z. B. & Vladikova, D. E. 2009. Electrochemical: Impedance Spectroscopy.

Elsevier, pp.632–642.

Tang, J., Moniz, A. J. A., Shevlin, S. A., Martin, D. J. & Guo, Z. 2015. Visible-light driven heterojunction photocatalysts for water splitting – a critical review. *Energy Environmental Sciences*, 8, pp.731–759.

Traldi, P., Crotti, S. & Aronco, S. D. 2018. Some Applications of Liquid Spectrometry in the Biomedical Field : New Analytical Methodologies and Instrumental Approaches. *Comprehensive Analytical Chemistry,* 79, pp.329-375.

Tseng, T. K., Lin, Y. S., Chen, Y. J. & Chu, H. 2010. A review of photocatalysts prepared by Sol-Gel method for VOCs removal. *International Journal of Molecular Sciences,* 11, pp.2336–2361.

Wang, L., Liu, Z., Zhang, J., Wu, Y. & Sun, H. 2016. Chlorpyrifos exposure in farmers and urban adults: Metabolic characteristic, exposure estimation, and potential effect of oxidative damage. *Environmental Research*, 149, pp.164–170.

Wang, X., Pang, L., Hu, X. & Han, N. 2015. Fabrication of ion doped WO_3 photocatalysts through bulk and surface doping. *Journal of Environmental Sciences*, 35, pp.76–82.

Warner, S. D. & Butler, I. S. 1970. Raman and FT-Raman Spectroscopy. *Comprehensive Coordination Chemistry II*, 2, pp.103–112.

Watanabe, M. 2017. Dye-sensitized photocatalyst for effective water splitting catalyst. *Science and Technology of Advanced Materials*, 18(1), pp.1–19.

Weckhuysen, B. M. (Ed). 2004. *In-situ Spectroscopy of Catalysts*. American Scientific Publishers, pp.1-11.

Weldon, R. H., Barr, D. B., Trujillo, C., Bradman, A., Holland, N. & Eskenazi, B. 2011. A pilot study of pesticides and PCBs in the breast milk of women residing in urban and agricultural communities of California. *Journal of Environmental Monitoring*, 13(11), pp.3136–3144.

Whittles, T. J., Burton, L. A., Skelton, J. M., Walsh, A., Veal, T. D. & Dhanak, V. R. 2016. Band alignments, valence bands, and core levels in the tin sulfides SnS, SnS_2, and Sn_2S_3: Experiment and Theory. *Chemistry of Materials*, 28(11), pp.3718–3726.

WHO. 2008. Children's Health and the Environment: WHO training Package for the Health Sector. *WHO*. (Accessed on 06 December 2018 at www.who.int/ceh).

Wu, S., Gao, G., Zhang, S., Zhu, W., Wang, L., Chen, R., Zhang, W., Wang, J., Yong, F., Li, J., Shen, L. & Sun, T. 2019. Mixed-solvent precipitation: A facile approach for nanoparticle self-assembled monolayers. *Applied Surface Science*, 465, pp.526–531.

Wu, X., Jiang, X., Chen, Q., Tian, Y. & Hou, X. 2014. Spark ablation − inductively coupled plasma optical emission for elemental depth profiling and imaging. *Microchemical Journal*, 116, pp.157–162.

Xiang, Q., Meng, G. F., Zhao, H. B., Zhang, Y., Li, H., Ma, W. J. & Xu, J. Q. 2010. Au nanoparticle modified WO_3 nanorods with their enhanced properties for photocatalysis and gas sensing. *Journal of Physical Chemistry*, 114, pp.2049–2055.

Xie, Y. P., Liu, G., Yin, L. & Cheng, H. 2012. Crystal facet-dependent photocatalytic oxidation and reduction reactivity of monoclinic WO_3 for solar energy conversion. *Journal of Materials Chemistry*, 22(14), pp.6746-6751.

Xu, H., Ouyang, S., Liu, L., Reunchan, P., Umezawa, N. & Ye, J. 2014. Recent advances in TiO_2-based photocatalysis. *Journal of Materials Chemistry A*, 2(32), pp.12642.

Yamamoto, H., Ohnuma, A., Ohtani, B. & Kozawa, T. 2013. Microelectronic engineering formation of nanoscale reaction field using combination of top-down and bottom-up nanofabricaiton. *Microelectronic Engineering*, 110, pp.369–373.

Yang, X., Wu, X., Brown, K. A., Le, T., Stice, S. L. & Bartlett, M. G. 2017. Determination of chlorpyrifos and its metabolites in cells and culture media by liquid chromatography-electrospray ionization tandem mass spectrometry. *Journal of Chromatography B*, 1063, pp.112–117.

Yang, X., Wolcott, A., Wang, G., Sobo, A., Fitzmorris, R. C., Qian, F., Zhang, J. Z. & Li, Y. 2009. Nitrogen-doped ZnO nanowire arrays for photoelectrochemical water splitting 2009. *Nano Letters*, 9(6), pp.2331–2336.

Yang, Y. B., Dash, J. K., Littlejohn, A. J., Xiang, Y., Wang, Y., Shi, J., Zhang, L. H., Kisslinger, K., Lu, T. M. & Wang, G. C. 2016. Large single crystal SnS_2 flakes synthesized from coevaporation of Sn and S. *Crystal Growth and Design*, 16(2), pp.961–973.

Yayra, B., Okoffo, E. D., Darko, G. & Gordon, C. 2016. Organophosphorus pesticide

residues in soils and drinking water sources from cocoa producing areas in Ghana. *Environmental Systems Research*, 5(10), pp.1-12.

Youssef, Z., Colombeau, L., Yesmurzayeva, N., Baros, F., Vanderesse, R., Hamieh, T., Toufaily, J., Frochot, C., Roques-Carmes, T. & Acherar, S. 2018. Dye-sensitized nanoparticles for heterogeneous photocatalysis: Cases studies with TiO_2 , ZnO , fullerene and graphene for water purification. *Dyes and Pigments*, 159, pp.49–71.

Yu, J., Xu, C., Ma, F., Hu, S., Zhang, Y. & Zhen, L. 2014. Monodisperse SnS_2 Nanosheets for High-Performance Photocatalytic Hydrogen Generation. *ACS Applied Materials & Interfaces*, 6(24), pp.22370–22377.

Zablotskii, A. V., Avilov, A. S., Bodunov, D. S., Kuzin, A. A., Kuzin, A. Y., Kuz'min, A. A. & Todua, P. A. 2013. A Method of estimating the stability of the scale factor of a transmission electron microscope. *Measurement Techniques*, 56(5), pp.14–16.

Zanjanchi, M. A., Noei, H. & Moghimi, M. 2006. Rapid determination of aluminum by UV – vis diffuse reflectance spectroscopy with application of suitable adsorbents. *Talanta*, 70, pp.933–939.

Zhang, Y. C., Du, Z. N., Li, K. W., Zhang, M. & Dionysiou, D. D. 2011. High-performance visible-light-driven SnS_2/SnO_2 nanocomposite photocatalyst prepared via in situ hydrothermal oxidation of SnS_2 nanoparticles. *ACS Applied Materials and Interfaces*, 3(5), pp.1528–1537.

Zhao, F. & Yang, Y. 2010. Use of monodisperse gold nanoparticles for transmission electron microscope high magnification calibration. *Colloid Journal*, 72(3), pp.346–352.

Zheng, Y., Zhang, L., Lin, L., Wygant, B. R., Liu, Y., Zhu, Y., Zheng, Y., Mullins, C. B., Zhao, Y., Zhang, X. & Yu, G. 2017. Highly efficient photoelectrochemical water splitting from hierarchical $WO_3/BiVO_4$ nanoporous sphere arrays. *Nano Letters*, 17, pp.3–8.

Zhou, P., Wang, X., Guan, W., Zhang, D., Fang, L. & Jiang, Y. 2017. SnS_2 nanowall arrays toward high performance sodium storage. *ACS Applied Materials & Interfaces*, 9, pp.6979-6989.

Zhu, X., Chen, H., Li, W., He, Y., Brookes, P. C. & Xu, J. 2014. Aggregation kinetics of natural soil nanoparticles in different electrolytes. *European Journal of Soil*

Science, 65, pp.206–217.

Zimba, M. & Zimudzi, C. 2016. Pesticide management practices among rural market gardening farmers near Harare, Zimbabwe. *South African Journal of Science*, 112(9), pp.71–75.

CHAPTER 3

EXPERIMENTAL PROCEDURE

3.1 Materials and methodology

3.1.1 Materials

Tungsten boride (WB) (≥97.0%), Tin(IV) chloride pentahydrate ($SnCl_4.5H_2O$, (98%)), Manganese(II) chloride tetrahydrate ($MnCl_2.4H_2O$, (≥98%)), nitric acid (≥65% puriss), Poly (vinylidene Fluoride) (PVDF), *N*-Methyl-2-pyrrolidone (NMP), silver paste, sodium sulfate (Na_2SO_4), silver/silver chloride (Ag/AgCl) electrode, sodium sulfide (Na_2S), chlorpyrifos (PESTNATAL, 99.9%) were all supplied by Sigma Aldrich. The chemicals were used as received.

3.2 Methodology

3.2.1 Synthesis of nanoparticles

Pristine WO_3 NPs were synthesized following method by Xie et al. (2012) with slight modification (Xie et al. 2012). Tungsten boride (4.12 mmol) was dissolved in 1 M HNO_3 (56.0 mL) under constant stirring, then transferred into a 100.0 mL Teflon lined stainless steel autoclave. The autoclave was heated in an oven at 190°C for 12 hours where a yellow solution was obtained. The yellow solution was further centrifuged (3 times at 1000 rpm for 10 minutes), washed 3 times with 30 mL of deionized water and dried at 100°C for 12 hours in an oven resulting in a yellow solid product of WO_3.

The same procedure was followed to obtain Mn-WO_3 via one pot synthesis of $MnCl_2.4H_2O$ (10.00 mmol) with WB (4.12 mmol) in 56.0 mL HNO_3 (Parthibavarman & Prabhakaran 2017).

Pristine SnS_2 NPs were synthesized by dissolving 2.73 mmol of $SnCl_4.5H_2O$ in 40.0 mL of deionized water under continuous stirring at 60°C for 10 minutes. Thereafter, Na_2S (2.73 mmol) was added to the solution and stirred for 10 minutes. The final mixture was then transferred into a 100.0 mL Teflon lined stainless steel autoclave and heated at 180°C for 12 hours. The resultant solution was then centrifuged 3 times at 1000 rpm for 10 minutes, washed 3 times with 30 mL deionized water and dried at 100 °C for 12 hours to obtain SnS_2 nanoparticles.

The heterojunction WO_3/SnS_2 was synthesized stepwise using a hydrothermal method (Li et al. 2014). The first step was adapted from the method for synthesizing pristine WO_3 and followed by the synthesis of SnS_2 NPs on the surface of dispersed WO_3 NPs in 40.0 mL of deionized water. The SnS_2 synthesis was adopted from the method of pristine SnS_2 NPs to obtain the heterojunction (WO_3/SnS_2).

Furthermore, the synthesis of Mn doped WO_3/SnS_2 heterojunction was carried out using hydrothermal treatment in a multistep method. Firstly, $MnCl_2.4H_2O$ (10.0 mmol) and tungsten boride (4.12 mmol) were dissolved in 1 M HNO_3 (56.0 mL) under constant stirring, then followed the same procedure as in the synthesis of WO_3 to obtain yellow solid product of Mn-WO_3.

The Mn-WO_3 (1.74 mmol) nanoparticles was dispersed in 40.0 mL of deionized water under continuous stirring and heat at 60°C. This was followed by the synthesis of SnS_2 NPs on the surface of Mn-WO_3 NPs adopted from the method of pristine SnS_2 nanomaterials to form Mn-doped WO_3/SnS_2 heterojunction composite nanoparticles. The heterojunction was obtained via hydrothermal treatment method at 180°C for 12 hours.

3.3.   Characterization techniques

The synthesized nanoparticles phases were characterized using powdered X-ray diffraction (XRD) (X'Pert Phillips) with CuKα radiation (0.1540 nm) monochromator beam in 2θ scan range from 20-80°. The instrument power settings used were 40 kV and 40 mA with a step size 2θ (0.0080) and scan step time of 0.0170 (2θ)

87.63s. The average crystallite size was calculated using Debye Scherrer's equation **(3.1)**:

$$L = \frac{K\lambda}{\beta cos\theta}$$ **(3.1)**

Where, β is the full width at half maximum, λ is the X-ray wavelength (0.1541 nm) for CuK_α, $K=0.89$, and θ is the diffraction angle. Raman spectroscopy (Raman Micro 200, Perkin Elmer) with a single monochromotor, a holographic notch filter and cooled TCD was used to determine the polymorphic of the phase of NPs vibrational and structural characteristics. The excitation was employed with a 514.5 nm Ar+ line. The power output used was below 0.5 mW at 4.0 seconds exposure time in dark field spectrum.

The morphological properties of the NPs were examined using high resolution transmission electron microscopy (HRTEM) (JOEL-TEM 2010) at an acceleration voltage of 200 kV. The ethanol (10 mL) dispersed nanoparticles (0.003 g) were deposited on carbon coated copper grid. Furthermore, selected area diffraction (SAED) images of the nanoparticles were captured and indexed using Crystbox software (Klinger, 2014). Field emission scanning electron microscope (FESEM) (TESCAN Vega TC instrument with VEGA 3 TESCAN software) coupled with energy dispersive X-ray (EDS) operated at 5.0 kV under nitrogen gas atmosphere was used to further study the morphology of the NPs and elemental composition.

Optical properties were investigated using UV spectrophotometer (Shimadzu UV-2450) using diffuse reflectance mode (DRS). $BaSO_4$ was used as reference. The band gap (E_g) of the nanomaterials, a graph of ($\alpha h\nu$) against photon energy ($h\nu$) was extrapolated following equation (*2*):

$\alpha h\nu = A (h\nu - E_g)^{n/2}$ **(3.2)**

where α is the absorption coefficient, $h\nu$ is the energy of the incident photon, A is a constant, and E_g is the bandgap energy. The value of n depends on semiconductor transition type, which are direct transition when n equals to 1 and indirect transition when n equals to 2. To measure the change in the position of the potential of valence band (E_{vb}) and conduction band (E_{cb}) equations (3) and (4) were used:

$$E_{cb} = \chi - E^o - 0.5E_g \qquad\qquad\qquad \textbf{(3.3)}$$
$$E_{vb} = E_{cb} + E_g \qquad\qquad\qquad\qquad \textbf{(3.4)}$$

Where, E_{cb} and E_{vb} are the conduction and valance band edge potentials, χ is the electronegativity of the semiconductor (the geometric mean of all the constituent atom's electronegativities), E° is the energy of free electrons on the hydrogen scale (4.5 eV), and E_g is the band gap of the semiconductor.

The photoluminescence spectra of the nanomaterials were obtained using PerkinElmer Fluorescence spectroscopy (Model LS 45). A 300 W xenon lamp was used as a light source. 0.003 g of the nanoparticles was dispersed in 100 mL deionized water for all the samples. 2 mL aliquot was transferred to a PL vial for measurements. The spectra were obtained at an excitation wavelength of 319 nm at room temperature. The excitation and emission wavelengths were set at 319 nm and 605 nm, respectively.

Surface area and pore volumes were performed using Brunauer-Emmett-Teller Surface isotherm (S_{BET}). The isotherms were obtained by nitrogen adsorption in a Micrometric ASAP 2020. The samples were degassed before the analysis at 100°C for 10 hours. The relative pressure (P/P_o) used was 0.980 for nitrogen adsorption volume during determination of pore volume.

Surface charge measurements were obtained using electrophoretic light scattering (ELS) by a Zetasizer NanoZS (Malvern) instrument. Zeta potential measurements were obtained using the Electrophoretic light scattering (ELS) to understand the surface charge of the nanomaterials as a function of pH of the solution. The nanomaterials were suspended into 30 mg/L in deionized (DI) water. The pH of the suspensions was adjusted to pH range of 2-10 using 1M NaOH and 1M HCl.

3.4 Preparation of chlorpyrifos standards

0.01 g of chlorpyrifos was dissolved in 1000 mL of deionized water in 1000 mL volumetric flask. Serial dilution was performed to prepare 75, 50, 25, 12.5, 6.25, 3.125 ppb. This was done by taking 1 mL of the previous solution and transferred into 2 mL LC-MS vial and 1 mL of deionized water was added. This was done until 3.125 ppb solution was obtained. The pH of the solutions was measured to be 5.78.

3.5 Photocatalytic activity

Photocatalytic activity of the nanomaterials was tested through photodegradation of chlorpyrifos in synthetic water samples under visible light irradiation (Photoreactor, Lelesil Innovative Systems). The volume of the working solution was kept at 500 mL of chlorpyrifos solution. Initially, the concentration of chlorpyrifos solution was 1 ppm and photocatalyst loading of 0.1 g was used at pH 5.8. The photodegradation reaction occurred under continuous magnetic stirring for 90 minutes under regulated temperatures of 20-25ºC subjected to a cooling jacket using ice cubes.

The photocatalyst suspension containing chlorpyrifos was kept in the dark for 30 minutes before irradiation to allow equilibration. The samples were collected from the batch reaction before and after irradiation in a set of time intervals (10 minutes, 10 mL aliquot) and filtered through a 0.45 µm PTFE membrane filter and transferred into a 2 mL LC-MS sample vial for analysis. The photocatalyst that degraded high concentration of chlorpyrifos was chosen to be $Mn-WO_3/SnS_2$ photocatalyst.

Furthermore, optimization of reaction conditions such as pH, initial chlorpyrifos concentration and initial photocatalyst loading were carried out. Therefore, the pH of the chlorpyrifos solution was adjusted to (3, 5.8, 7, 9), initial concentration of the pesticide (chlorpyrifos) to (100 ppb, 1 ppm, 5 ppm, 10 ppm and 20 ppm) and photocatalyst loading to (0.1 g, 0.5 g, 1 g and 2g).

Therefore, the filtered samples were analyzed using a triple quad UHPLC-MS/MS 8030 (Shimadzu Corporation) to monitor the removal of chlorpyrifos. The LC-MS/MS was fitted with Nexera UHPLC upgrade with capability to obtain 500 multiple reaction monitoring readings per second. The oven was equipped with a Raptor™ ARC-18 column (Restek Corporation) with 2.7 μm pore diameter, length 100 mm x 2.1 mm maintained at 40ºC. The mobile phase consisted of 0.1% formic acid in ratio of ultrapure water:methanol (9:1 %, v/v) at flow rate of 0.200 mL/min of 10μL injection volume. The ion source was electrospray ionization (ESI) and was operated at positive mode. The LC and MS/MS data for degradation intermediates was obtained after full scan mode was ran for 12 minutes at flow rate of 0.3 mL/min.

The percentage removal of chlorpyrifos in the synthetic water samples was calculated using equation **3.5** below:

$$\% \ chlorpyrifos \ removal = \left(1 + \frac{C}{C_0}\right) \times 100 \qquad (3.5)$$

Where C_o is the initial concentration and C is the final concentration of chlorpyrifos. The degradation products were determined by analyzing the samples for a period of 60 minutes. The degradation pathway was then deduced from the mass/ion ratio obtained from the MS spectrum. The reaction kinetics of chlorpyrifos degradation were studied and second order model fitted the results and the plot based on the calculated (1/[C]) versus reaction time was obtained.

$$\frac{1}{[C]_t} = kt + \frac{1}{[C]_0} \qquad (3.6)$$

Whereby, k is the rate constant, t is time taken for reaction, $[C]_t$ is the concentration of chlorpyrifos when time equal to t, and $[C]_0$ is the initial concentration of chlorpyrifos. The reaction rate is thus given by **Equation 3.7**:

$$rate = k[C]^2 \qquad (3.7)$$

3.5 References

Klinger, M. 2017. More features, more tools, more CrysTBox. *Journal of Applied Crystallography*, 50, pp.1-9.

Li, J., Du, X., Yao, L. & Zhang, Y. 2014. Synthesis of SnS_2/WO_3 nanocomposite with enhanced photocatalytic activity. *Materials Letters,* 121, pp.44–46.

Parthibavarman, M. K. M. & Prabhakaran, A. K. S. 2017. One-step microwave synthesis of pure and Mn doped - nanoparticles and its structural, optical and electrochemical properties. *Journal of Materials Science: Materials in Electronics*, 28(9), pp.6635–6642.

Xie, Y. P., Liu, G., Yin, L. & Cheng, H. 2012. Crystal facet-dependent photocatalytic oxidation and reduction reactivity of monoclinic WO_3 for solar energy conversion. *Journal of Materials Chemistry*, 22(14), pp.6746-6751.

CHAPTER 4

SYNTHESIS AND CHARACTERIZATION OF A MULTICOMPONENT

Mn-WO$_3$/SnS$_2$ COMPOSITE SYSTEM[*]

[*]Part of the work presented in this chapter has been submitted for publication in a peer-review journal.

4.1 Introduction

Fabrication and modification of photocatalysts has sparked interests amongst researchers due to their wide applications. Photocatalysts are used in applications ranging from water splitting, degradation of pollutants in water, gas sensing and optoelectronic devices (Dong et al. 2017).

These can be *n-type* (electrons are major charge (carriers) or *p-type* (holes are major charge carriers) photocatalysts (Marschall 2014). The most studied photocatalysts are TiO$_2$, WO$_3$ (*n-type*) and ZnO, CdS (*p-type*) degradation of organic and inorganic pollutants in water (Xie et al. 2012; Mahlalela et al. 2017). The photocatalytic efficiency of these materials is limited to certain extend, primarily, due to two major limitations.

Firstly, they are prone to fast electron-hole recombination which reduces the photocatalytic reactivity of the semiconductor. Lastly, they have wide band gaps that only absorb in the ultraviolet (UV) region which accounts to 4% of the solar spectrum (Batzill 2011).

Modification of photocatalyst to suit specific applications have been proposed. These include the use of metal dopants to form Schottky barriers and the fusion with other semiconductor photocatalysts resulting in heterojunctions (Marschall 2014). Metal dopants that have been employed include magnesium (Mg) (Harshulkhan & Velraj 2017), manganese (Mn) (Parthibavarman & Prabhakaran 2017), copper

(Cu)(Lu et al. 2016) and yttrium (Y) (Yamamoto et al. 2016) which resulted in improved photoactivity of the pristine photocatalyst.

Metal doping of photocatalysts shifts the bandgap of the material to absorb the readily available visible region of the solar spectrum. They also separate photogenerated charges by forming electron traps. Though, high concentration of the metal dopant may result in the creation of recombination centers which leads to increased recombination rate.

Heterojunction is an interface between two photocatalysts materials with different band gaps to result in a more enhanced optical and photocatalytic properties towards pollutant removal by probing the limitations of the pristine photocatalysts. Heterojunctions reported so far with enhanced optical and photocatalytic properties include $BiVO_4/WO_3$ (Chae et al. 2017), CdS/ZnO (Velanganni et al. 2018) and TiO_2/SnO_2 (Afuyoni et al. 2011; Shaposhnik et al. 2011).

The formation of heterojunction using a different photocatalyst is sufficient to reduce recombination rate of photogenerated charges. This occurs by accumulation of photoexcited electrons in the conduction band (CB) of one semiconductor while photogenerated holes accumulate in the valence band (VB) of another semiconductor in the heterojunction system which effectively lead to charge separation.

Therefore, photo-oxidation and photo-reduction occur on different semiconductor surface of the heterojunction system due to different migration points of the photogenerated charges (Tang et al. 2015). The photogenerated charges move across the interface due to contact established for charge transfer netween the two photocatalysts.

Tungsten trioxide (WO_3) is a visible light photocatalyst with band gap energy of 2.5-2.8 eV (Simelane et al. 2017). It is classified as *n*-type semiconductor whereby electrons are the major carriers. Due to its narrow bandgap, WO_3 absorbs light

radiation in the visible range, and it has been used in wide range of applications such as fuel production, and combating water pollutants (Georgaki et al. 2015; Székely et al. 2016). This semiconductor exists in different polymorphs, which include monoclinic, triclinic, tetragonal and orthorhombic. The monoclinic phase of WO$_3$ is the most stable, easily obtained and most photocatalytic than all the other phases. The VB potential of WO$_3$ is more positive to oxidize a wide variety of organic pollutants.

Tungsten trioxide (WO$_3$) suffers from limitations such as high electron-hole charge recombination. To overcome the intrinsic limitation of pristine WO$_3$, different ways have been used including metal doping and another semiconductor photocatalyst to form a heterojunction (Chae et al. 2017; Joshi et al. 2011; Cai et al. 2016).

However, this chapter reports the synthesis and characterization of WO$_3$ photocatalyst material that fuses metal doping and heterojunction (Mn-WO$_3$/SnS$_2$) that exhibit improved optical properties and minimized electron-hole recombination compared to the current/individual photocatalysts.

Owing to tin (IV) disulfide (SnS$_2$) high electron mobility through Sn-S bond, it will effectively facilitate electron transfer to WO$_3$ CB upon illumination. Therefore, separation of electrons and holes will be established. The Mn^{2+} ion will be placed on the fermi level of WO$_3$ therefore separate charges by trapping electrons from returning to the VB in WO$_3$ thereby increasing their lifetime. Metal dopants can also act as reaction centers. This photocatalyst can be applied in water remediation, energy production and sensing. In this work, the photocatalytic efficiency of Mn-WO$_3$/SnS$_2$ was tested for photodegradation of organophosphate pesticide called chlorpyrifos in water and the photocatalytic activity was reported in **Chapter 5**.

To the best of our knowledge no work has been reported that focused on metal doped WO$_3$ nanoparticles fused heterojunction (Mn-WO$_3$/SnS$_2$) photocatalysts so far.

## 4.2 Characterization of nanomaterials

4.2.1 X-Ray Diffraction

The phase and crystallographic properties of the nanomaterials were elucidated using XRD and Raman spectroscopy.

Figure 4.1(a) shows the XRD pattern of WO$_3$ which confirm a monoclinic nature of the WO$_3$ (*m*-WO$_3$). The *m*-WO$_3$ was indexed and matched to the indices (002), (020), (200), (120), (112), (022), (202), (122), (222), (004), (040), (400), (042), (420) (JCPDs no.00-043-1035).

Doping the *m*-WO$_3$ with Mn^{2+} did not distort the phase of WO$_3$, which infers it had been intrinsically inserted into WO$_3$ crystal lattice as depicted in **Figure 4.1(b)**. There was a slight decrease in crystallite size due to the insertion of manganese in the lattice and no additional peaks corresponding to Mn due to low doping concentration (**Appendix 1**). The heterojunction between WO$_3$/SnS$_2$ was successfully confirmed as the hexagonal phase (ICDD no.00-023-0677) of SnS$_2$ could be indexed in **Figure 4.1(c),** indices represented by harsh (**#**).

Again, the structural integrity of manganese fused WO$_3$/SnS$_2$ heterojunction (**Figure 4.1(d)**) was not distorted by the incorporation of Mn^{2+} in the system as the indices corresponding to WO$_3$(*) and SnS$_2$(**#**) were observed. The pristine hexagonal phase of SnS$_2$ was successfully formed confirmed by a high intensity characteristic peak 001 at 15.01º.

The average crystallite sizes of the nanomaterials were obtained using Debye-Scherrer's equation and are tabulated in (**Appendix 1)**, all with an average of 40 nm, with SnS$_2$ having a crystallite size less than 20 nm.
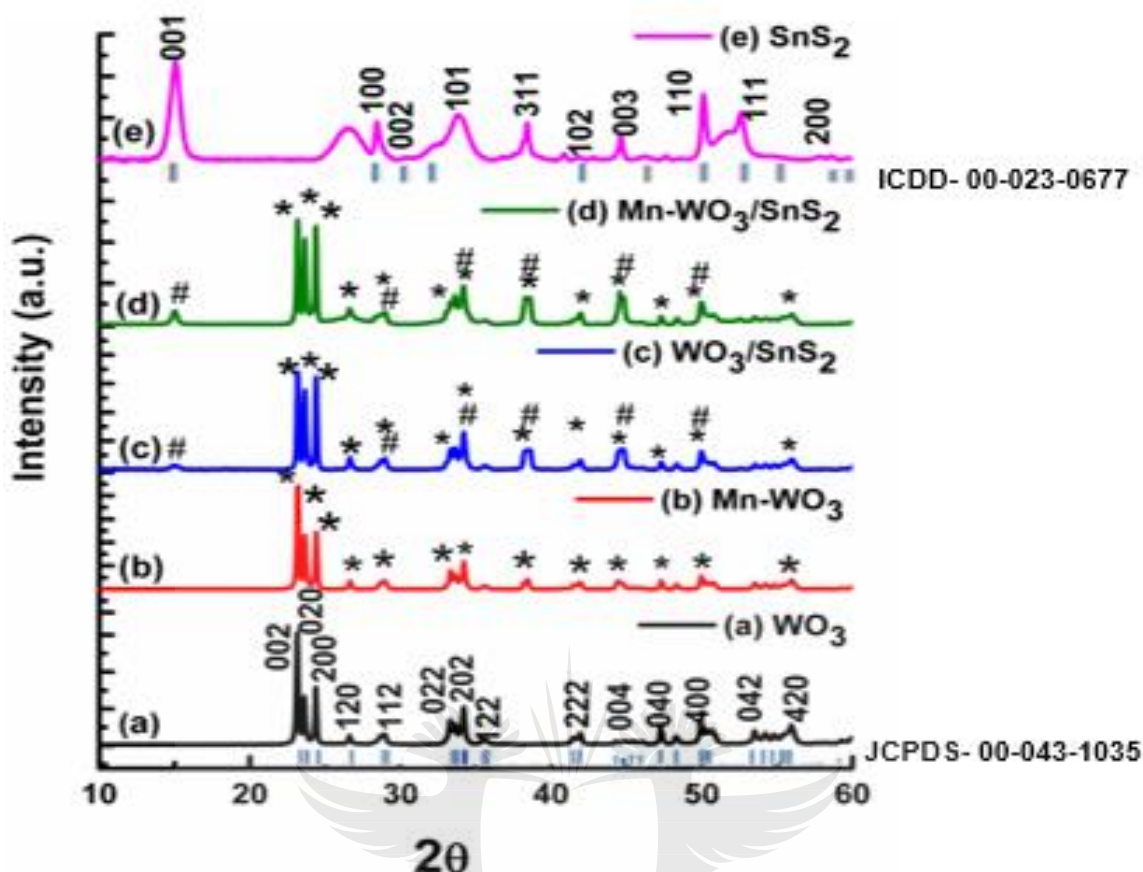
Figure 4.1: XRD patterns of **(a)** WO₃, **(b)** Mn-WO₃, **(c)** WO₃/SnS₂, **(d)** Mn-WO₃/SnS₂, and **(e)** SnS₂.

4.2.2 Raman analysis

The nature of the phases was further confirmed with Raman analysis. **Figure 4.2(a)** illustrates Raman bands at 717 and 818 cm^{-1} and less intense 212 and 313 cm^{-1} corresponding to O-W-O stretching and bending in the molecule, respectively, which confirms a monoclinic WO₃. As in XRD analyses, the doping of Mn^{2+} had no effect on the phase of WO₃ as depicted in **Figure 4.2(b).** No secondary bands resulting from Mn-oxides were observed which implies that the Mn ion was intrinsically inserted into the lattice of WO₃ at low concentration.

The heterojunction (WO₃/SnS₂) was successfully formed as confirmed by Raman band at 317 cm^{-1} corresponding to A$_{1g}$ mode of nanosized hexagonal phase SnS₂ and bands corresponding to WO₃ (**Figure 4.2(c)**). **Figure 4.2(d)** displays Raman

band of Mn-WO$_3$/SnS$_2$ with no distortion due to Mn^{2+} and SnS$_2$. Therefore, **Figure 4.2(e)** corresponds to the pristine hexagonal phase of SnS$_2$ due to the A$_{1g}$ band at 317 cm^{-1}.
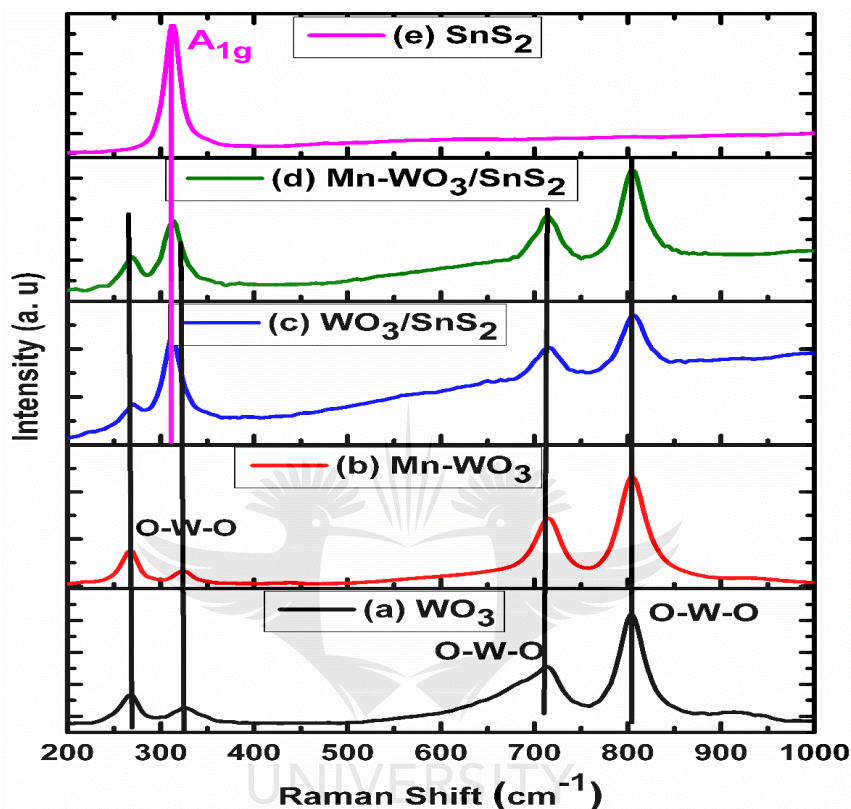
Figure 4.2: Raman spectra of **(a)** WO$_3$, **(b)** Mn-WO$_3$, **(c)** WO$_3$/SnS$_2$, **(d)** Mn-WO$_3$/SnS$_2$, and **(e)** SnS$_2$.

4.2.3 Morphological studies

The morphological studies were conducted using microscopic techniques such as FESEM and HRTEM. **Figure 4.3(a)** is the FESEM image of pristine *m*-WO$_3$ with rectangular sheets, rods and cubes, and the composition was confirmed by EDS (**Figure 4.3 (b)**). This morphology was also observed by Xie et al. 2012 for materials synthesized using the same synthetic route. The HRTEM image (**Figure 4.3(c)**) confirmed the rectangular sheets and rods, and the corresponding SAED image displays spots obtained through 1-10 zone axis corresponding to 002, 112, 220 and 11-2 indices (**Figure 4.3(d)**) also observed in XRD spectrum for *m*-WO$_3$.
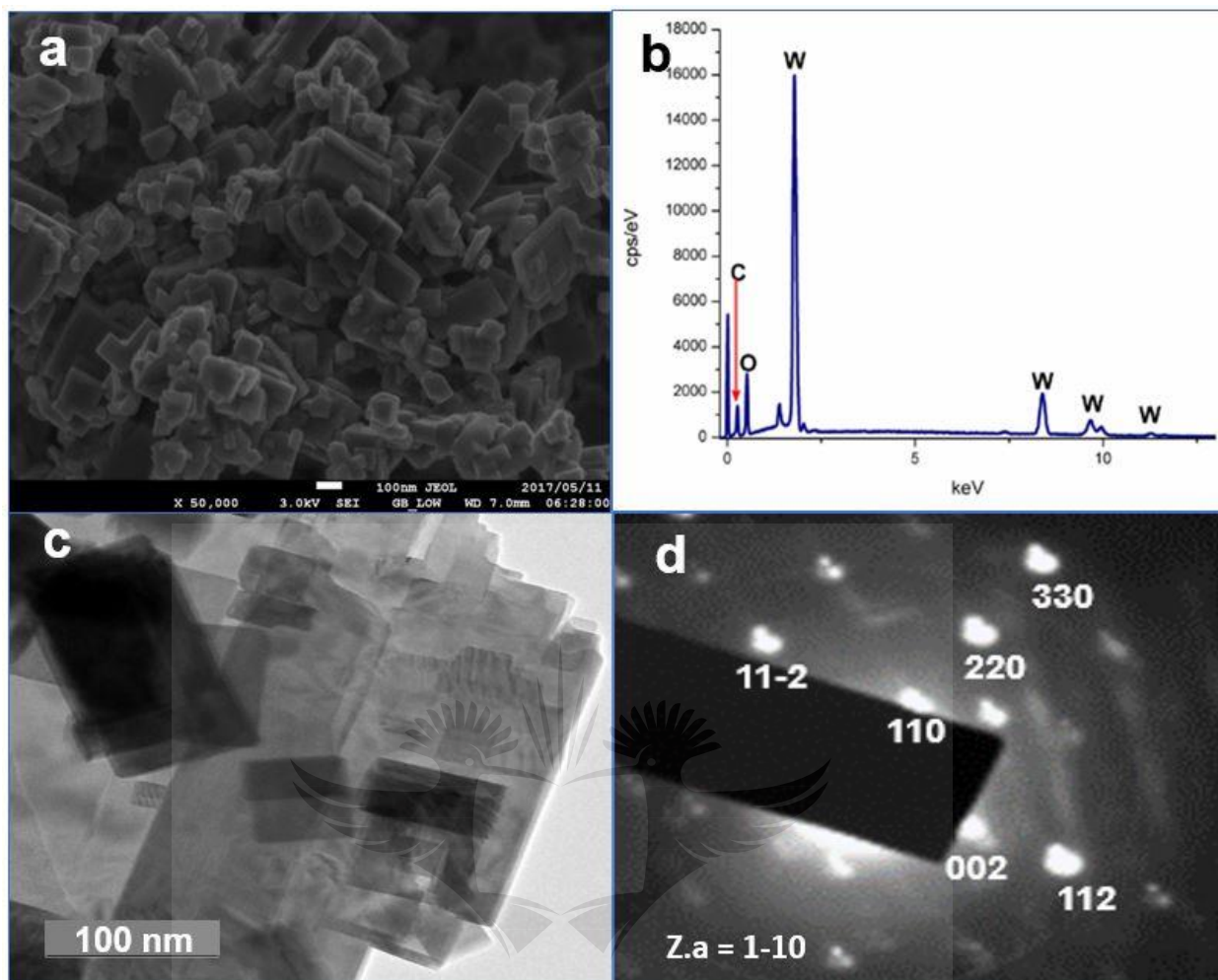
Figure 4.3: **(a)** FESEM image, **(b)** EDS spectrum, **(c)** HRTEM image and **(d)** SAED image of pristine WO₃.

The pristine SnS₂ morphological analysis shows rod-like structures as seen on FESEM and HRTEM images (**Figure 4.4 (a)** and **(c)**). The EDS spectrum shows Sn and S in the material composition (**Figure 4.4 (b)**). Furthermore, the SAED image (**Figure 4.4 (d)**) obtained through 002 zone axis illustrates ring indices corresponding to 110, 014, 012 and 004 planes like indices observed on XRD. This result supports the data obtained in **Figure 4.1 (e).**
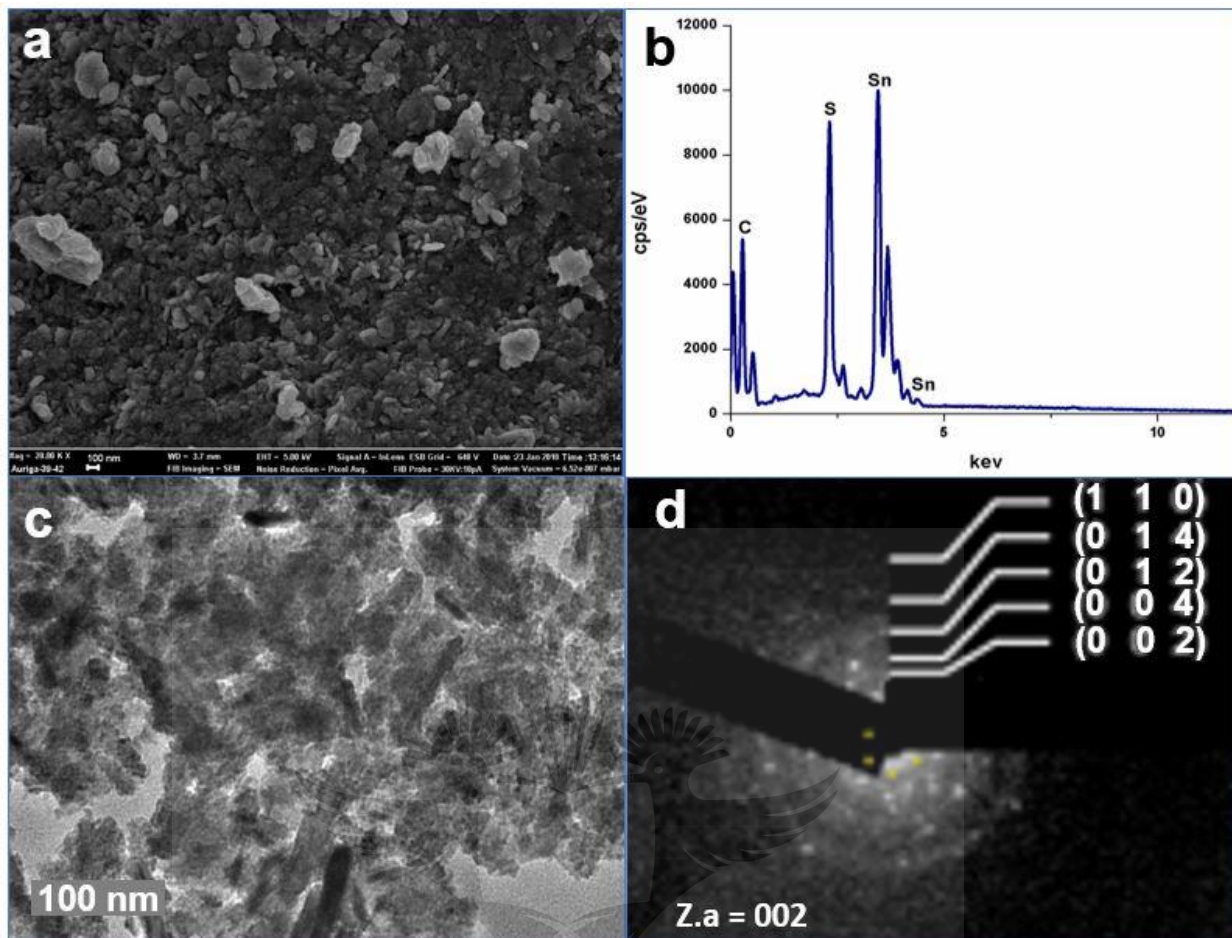
Figure 4.4: **(a)** FESEM image, **(b)** EDS spectrum, **(c)** HRTEM image and **(d)** SAED image of pristine SnS$_2$.

Furthermore, the shapes of the nanomaterials did not change upon insertion of Mn^{2+} and the formation of the heterojunction as illustrated in **Figure 4.5(a)-4.6(a)**. The EDS spectra displayed the elemental composition of the respective heterojunctions (WO$_3$/SnS$_2$) and Mn-WO$_3$/SnS$_2$ (**Figure 4.5(b)-4.6(b)**). All atoms were present at appropriate quantities and proportion.

The HRTEM images (**Figure 4.5(c)-4.6(c)**) displayed rectangular rods and sheets in reference to **Figure 4.3(c)** which implies that no shape distortion through metal doping and formation of heterojunction occurred.

The SAED image (**Figure 4.5(d)-4.6(d)**) displays rings and spots characteristic to monoclinic and hexagonal phase WO$_3$ and SnS$_2$ respectively. Furthermore, SAED

image illustrates spots (202, 200) and ring (101, -103) indices corresponding to WO_3 monoclinic phase and SnS_2 hexagonal phase respectively, captured through 0-10 zone axis using Crystbox software (Klinger 2017) (**Figure 4.6(d)**). This further support the formation of heterojunction as XRD and raman agrees.

All the SAED indices corresponds to the reported XRD patterns which further confirms the successful formation of our respective nanomaterial.
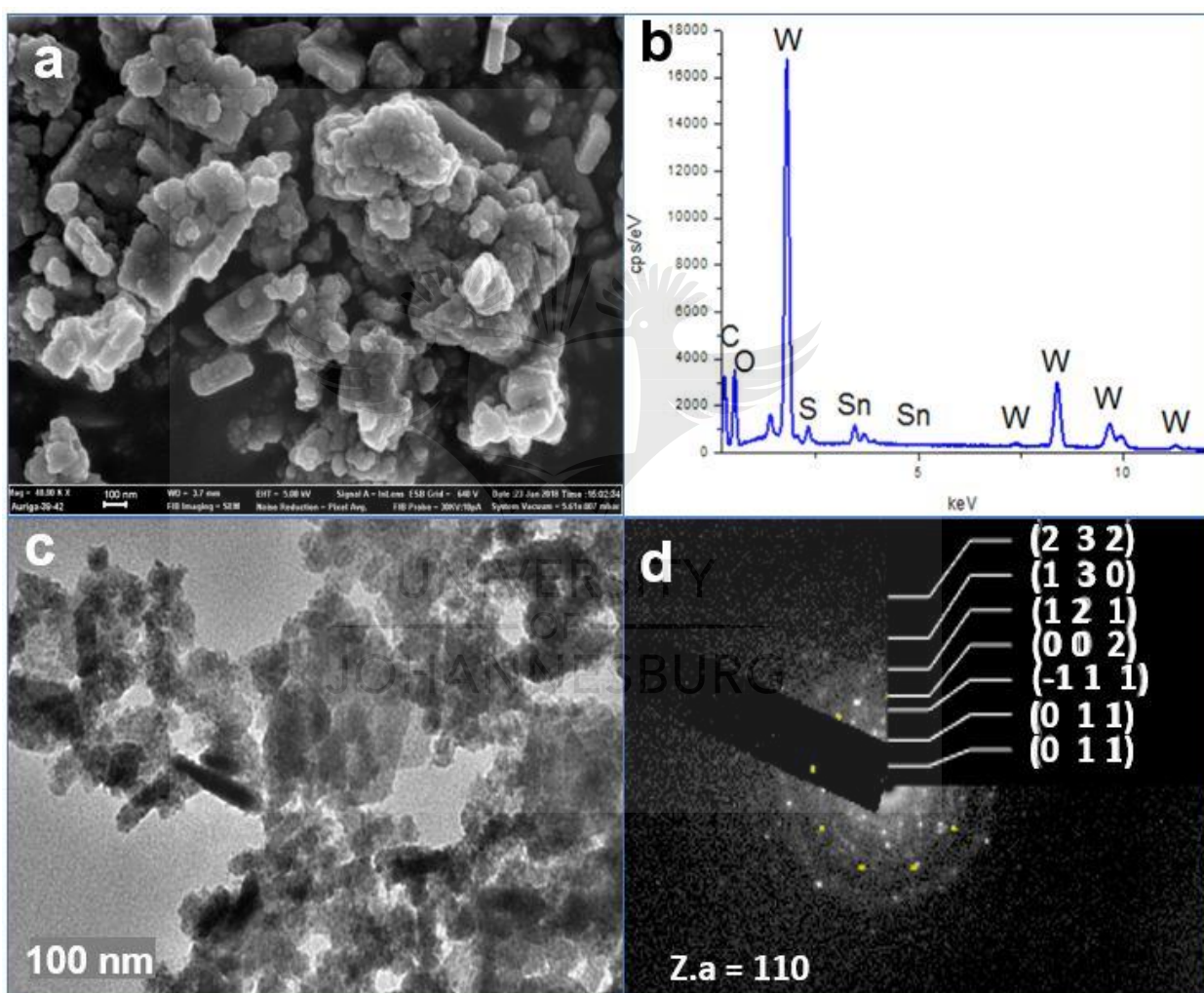
Figure 4.5: **(a)** FESEM image, **(b)** EDS spectrum, **(c)** HRTEM image and **(d)** SAED image of WO_3/SnS_2.
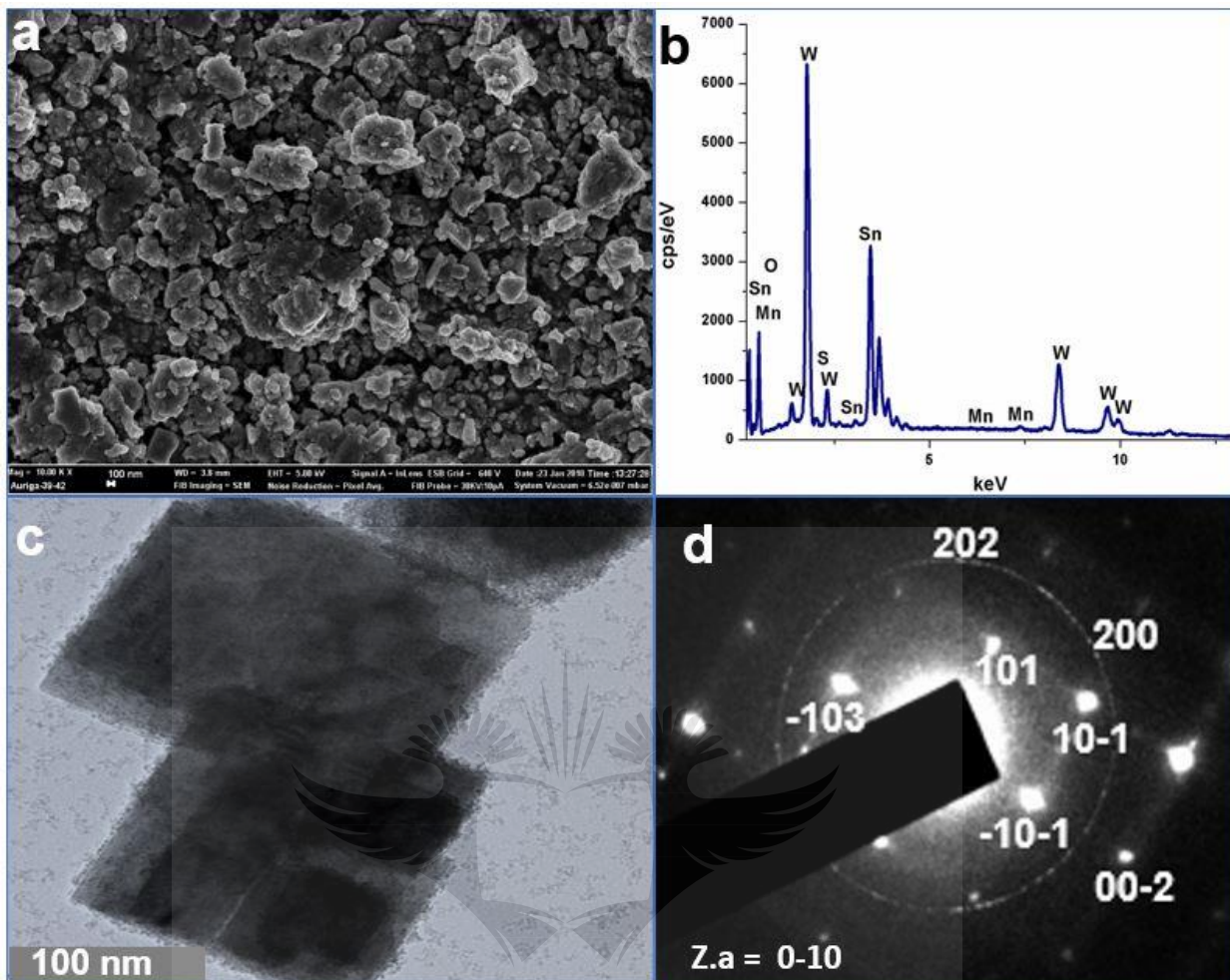
Figure 4.6: **(a)** FESEM image, **(b)** EDS spectrum, **(c)** HRTEM image and **(d)** SAED image of Mn-WO$_3$/SnS$_2$.

4.2.4 Optical properties

The ultraviolet-visible spectroscopy in diffuse reflectance mode was used to determine the optical properties of the synthesized nanoparticles.

All the synthesized nanomaterials showed absorption in the visible region which is in abundance. Pristine m-WO$_3$ displayed a band gap of 2.71 eV with a corresponding absorption wavelength of 466 nm as showed in **Figure 4.7(a)**. The value obtained agrees with the value reported by Simelane et al, 2016.

The insertion of Mn^{2+} in the *m*-WO$_3$ lattice introduced impurities in the fermi level below the conduction band promoting the WO$_3$ to red-shift on the spectrum (**Figure 4.7(b)**). The band gap of WO$_3$ was reduced upon the insertion of Mn and further after the formation of a heterojunction with SnS$_2$ (**Figure 4.7(a-e)**). This result was also observed by Abhudhahir & Kandasamy 2015.

The Mn fused heterojunction (Mn-WO$_3$/SnS$_2$) had the lowest band gaps (2.08 eV and 2.34 eV) amongst other nanomaterials (WO$_3$, SnS$_2$, Mn-WO$_3$ and WO$_3$/SnS$_2$) which corresponds to high light absorption wavelength (red-shift) (Li et al. 2014) (**Figure 4.7(e)**). This was due to visible light absorption enhancement by both Mn ion and SnS$_2$. The two smoothly connected peaks indicate a continuous optical absorption between two interfaced photocatalysts in the heterojunction.
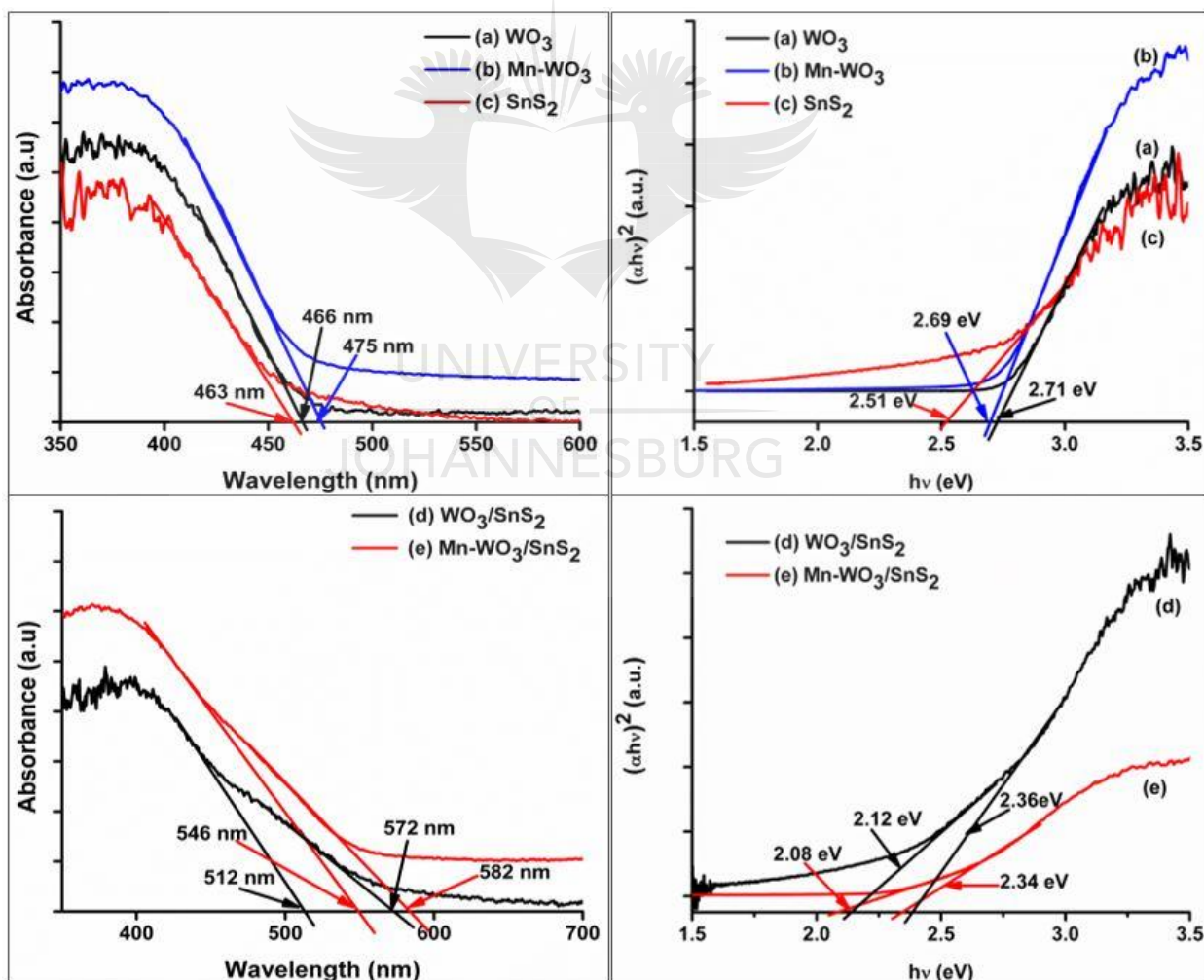
Figure 4.7: Absorption edge and the corresponding tauc plot (band gap) of **(a)** WO$_3$, **(b)** Mn-WO$_3$, **(c)** SnS$_2$, **(d)** WO$_3$/SnS$_2$ and **(e)** Mn-WO$_3$/SnS$_2$.

Figure 4.8 diagram illustrates the change in band edge potentials of the synthesized semiconductor photocatalysts. The calculated band edges were obtained using equations **3** and **4**.

There was a small decrease in band edges (E_{cb} and E_{vb}) during the introduction of Mn and fusion with SnS$_2$ (Mn-WO$_3$/SnS$_2$) due to the lattice strain induced by Mn ion and SnS$_2$. The E_{cb} shifted to more positive (by 0.2 eV) and the E_{vb} moved to less positive potential (by 0.2 eV). This was due to the insertion of an ion with high ionic radius which reduces the band gap by pulling the band edges closer by electrostatic forces. The change in the band edges enhance the absorption wavelength of the material.

The heterojunction (Mn-WO$_3$/SnS$_2$) enhance charge separation by the movement of electrons from SnS$_2$ CB to WO$_3$ CB through the interface, thereby leaving holes in the VB of SnS$_2$. This effectively separate the electrons and holes as they accumulate in CB of WO$_3$ and VB of SnS$_2$ respectively.
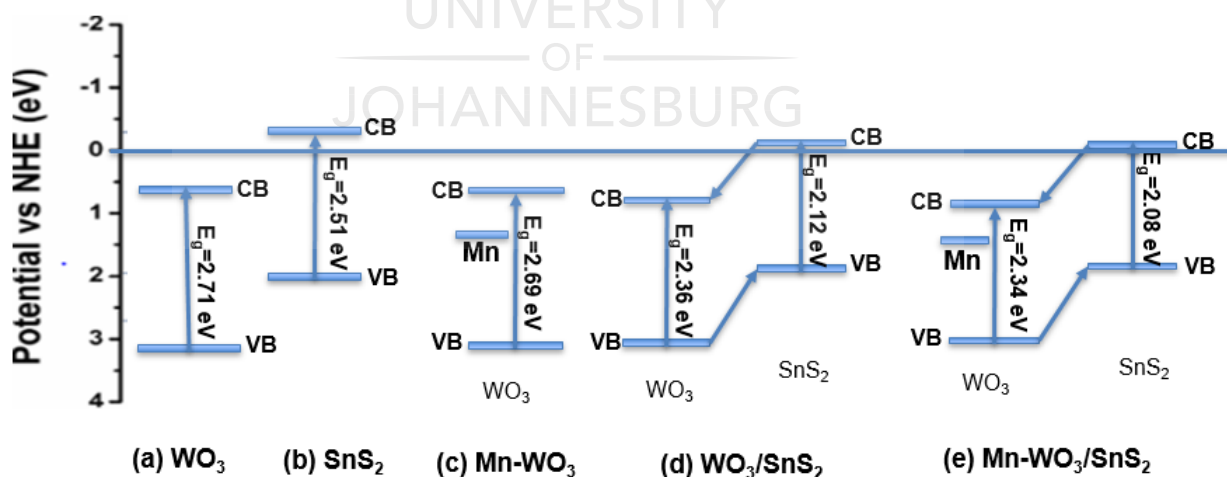
Figure 4.8: Diagram showing band edges of **(a)** WO$_3$, **(b)** SnS$_2$, **(c)** Mn-WO$_3$, **(d)** WO$_3$/SnS$_2$, and **(e)** Mn-WO$_3$/SnS$_2$ photocatalysts.

4.2.5 Electrochemical measurements

The electrochemical impedance measurements were conducted to study the interfacial reactions occurring between the photo electrode and the electrolyte. **Figure 4.9(a)** illustrates the EIS spectrum with a suppressed semicircle with a large diameter. At low frequency, the current density is in phase with the potential deviation of the system resulting in a straight line at an angle of 45° to the x-axis. The semicircle at high frequency corresponds to the high charge transfer impedance of WO$_3$. This implies high electrode-electrolyte charge transfer impedance which relate to high charge recombination rate as observed in **Figure 4.9(a)**.

The charge transfer impedance was reduced after WO$_3$ was doped with Mn^{2+} ion (**Figure 4.9(b)**) due to reduced charge recombination rate. This was alluded to Mn^{2+} ion acting as charge collection site thereby serving as electrical conductive pathway allowing ion/electron mobility on the electrode (Parthibavarman & Prabhakaran 2017).

The small diameter of the semicircle of Mn-WO$_3$/SnS$_2$ spectrum indicate decreased electrode-electrolyte charge-transfer resistance/impedance compared to WO$_3$/SnS$_2$, Mn-WO$_3$, SnS$_2$ and WO$_3$ in the 0.1 M Na$_2$SO$_4$ electrolyte. The sloping straight line in the low-frequency region corresponds to oxygen diffusion within the electrode (**Figure 4.9(a)**).

The low charge resistance of Mn-WO$_3$/SnS$_2$ arises from the enhanced charge carrier separation brought by the Mn^{2+} ion dopant and SnS$_2$ semiconductor heterojunction with WO$_3$. The charge resistance and recombination rate decreased from WO$_3$, Mn-WO$_3$, SnS$_2$, WO$_3$/SnS$_2$ up to Mn-WO$_3$/SnS$_2$ (**Figure 4.9(a) - (e)**).
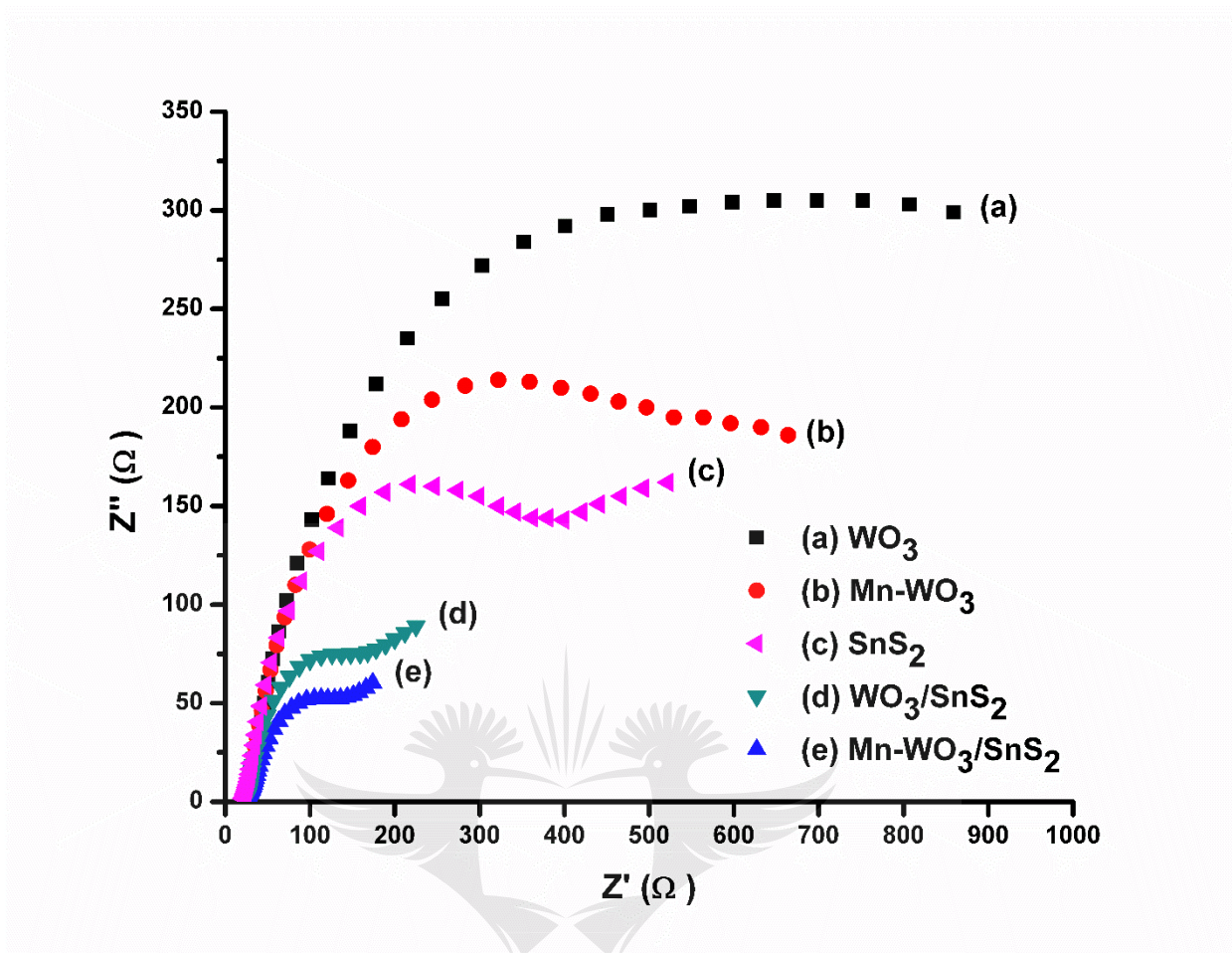
Figure 4.9: The Electrochemical impedance spectra (Nyquist plot) of **(a)** WO₃, **(b)** Mn-WO₃, **(c)** SnS₂, **(d)** WO₃/SnS₂ and **(e)** Mn-WO₃/SnS₂ vs. (Ag/AgCl).

The equivalent circuit models (**Figure 4.10**) corresponding to the graphs show that the impedance was a contribution of three forms of resistance. The solution and electrode resistance are due to the film compost of the nanomaterials, and charge-transfer resistance occur at the electrolyte-electrode interface.

The Warburg impedance is due to solid-state ion diffusion during the electrochemical reaction. It is usually apparent by the 45° angle at low frequencies. Different slopes of the straight line part at low frequency indicates that the electrodes have different Warburg impedances and solid-state ion diffusion behaviors.
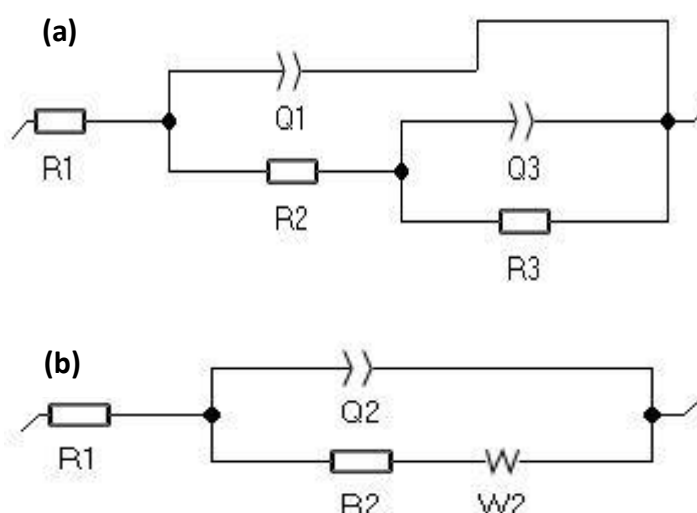
Figure 4.10: Randles circuit models corresponding to **(a)** WO$_3$ and Mn-WO$_3$, **(b)** SnS$_2$, WO$_3$/SnS$_2$ and Mn-WO$_3$/SnS$_2$.

R1 is the solution resistance, R2 is the thin layer resistance, R3 is the charge transfer resistance, W2 is the Warburg resistance and Q1, Q2 and Q3 are the constant phase elements (**Figure 4.10**). The Warburg impedance relates to electrode surface reactivity towards reactive species present in the solution, which favors photocatalytic activity by utilizing the separated charges during the reaction and consequently, reduce charge recombination. The Warburg impedance slope also indicate the reactivity of the nanoparticles, which favors photocatalytic activity. The charge transfer impedance was 631.80, 498.50, 310.55, 173.65 and 157.16 Ω for WO$_3$, Mn-WO$_3$, SnS$_2$, WO$_3$/SnS$_2$ and Mn-WO$_3$/SnS$_2$ respectively. This implies that Mn-WO$_3$/SnS$_2$ will have high charge mobility, low charge recombination and high photocatalytic activity amongst other photocatalysts.
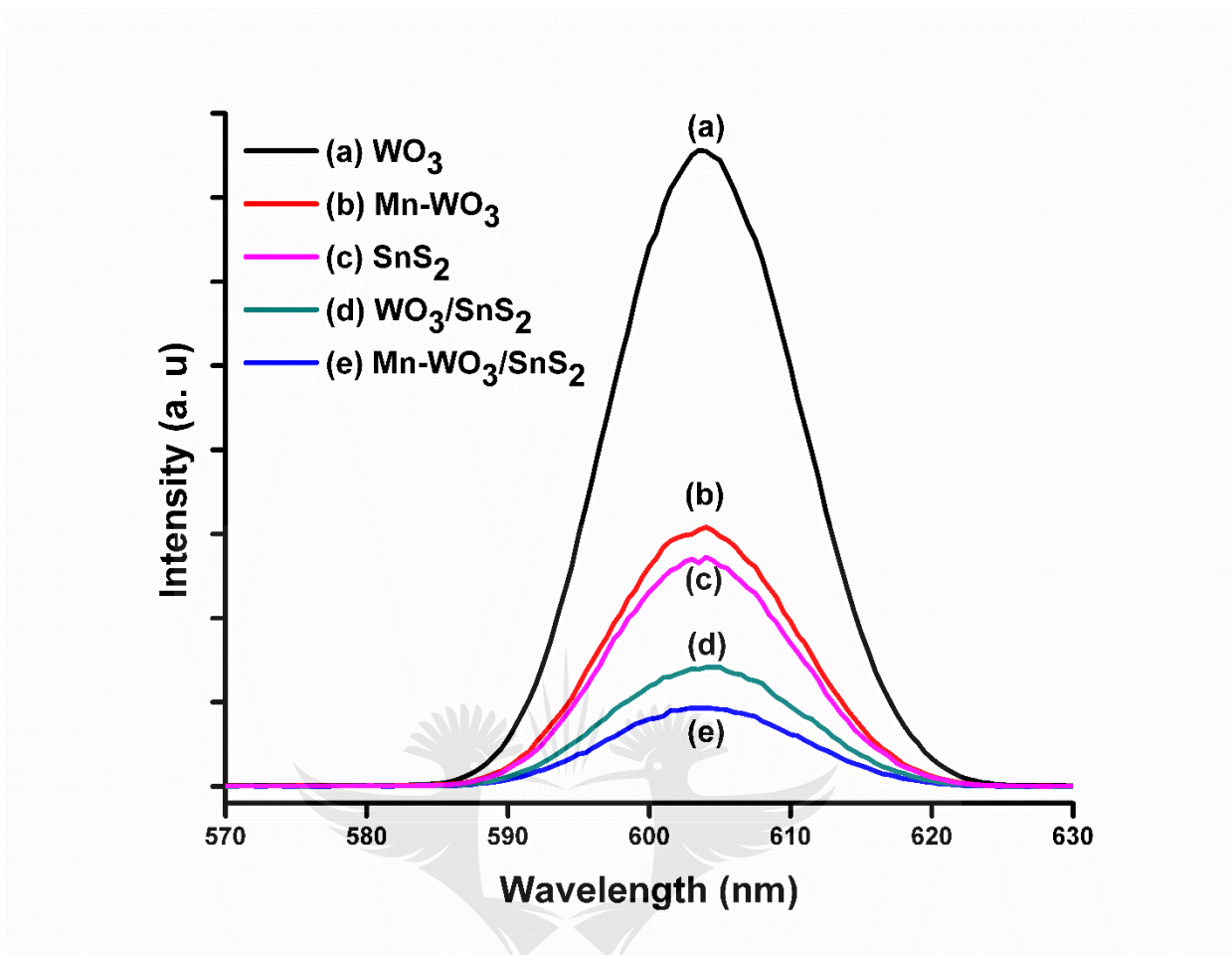

4.2.6 Photoluminescence Spectroscopy (PL)

Photoluminescence spectroscopy (PL) measure the energy distribution of emitted photons intensity of the electrons to understand charge recombination rate of the material. The emission intensity was obtained by firstly exposing the nanoparticles to radiation at excitation wavelength of 319 nm at room temperature (**Figure 4.11**) (Abhudhahir & Kandasamy, 2015). The emission peaks between 585-625 nm are

due to oxygen vacancies for WO$_3$ and different luminescent centers such as defect energy levels arising from manganese interstitials (**Figure 4.11(a)-(b)**). High value of emission intensity corresponds to high charge recombination rate and low emission intensity correspond to low charge recombination rate. The pure (WO$_3$ and SnS$_2$) and doped WO$_3$ have strong and wide emission spectrum in the wavelength range of 585-625 nm with the excitation wavelength of 319 nm.

The findings in **section 4.2.5** are supported by photoluminescence (PL) measurements (**Figure 4.11(b)**) whereby WO$_3$ have high emission peak which corresponds to high charge recombination and it was reduced by the introduction of Mn and fusion with SnS$_2$ (**Figure 4.11(e)**) (Govindan et al. 2018). The Mn ion acts as electron trap/sink which assist with separation of photogenerated charges. The SnS$_2$ forms an interface with WO$_3$ which further assist in separation of the photogenerated charges by movement from one photocatalyst to another through the interface contact.

The Mn-WO$_3$/SnS$_2$ had low emission peak on PL corresponding to low charge recombination which implied that charges will be effectively separated for utilization during photocatalytic applications. This is alluded to longer charge lifetime on the surface of the photocatalyst thereby minimizing the electron-hole recombination.

Figure 4.11: Photoluminescence spectra of **(a)** WO_3, **(b)** $Mn\text{-}WO_3$, **(c)** SnS_2, **(d)** WO_3/SnS_2, **(e)** $Mn\text{-}WO_3/SnS_2$ at excitation wavelength of 319 nm.

4.2.7 Linear Sweep Voltammetry (LSV)

The photocurrent density of WO_3 observed was improved upon introduction of Mn^{2+} and SnS_2 up to 0.030 mA/cm^2 for $Mn\text{-}WO_3/SnS_2$ NPs (**Figure 4.12(c)**). This implied that there was high electron flow between the photocatalyst and the electrolyte produced from the photocatalyst upon light irradiation. Mn^{2+} acts as an electron sink and reaction side which in turn supplies electrons for interfacial reactions and SnS_2 helps in the production of electrons and their separation from holes which increases the current density. The composite ($Mn\text{-}WO_3/SnS_2$) showed high current density which implies that photogenerated charges are found on the surface of the catalyst

94

and are easily accessible for photocatalytic activity, therefore, recombination is reduced.
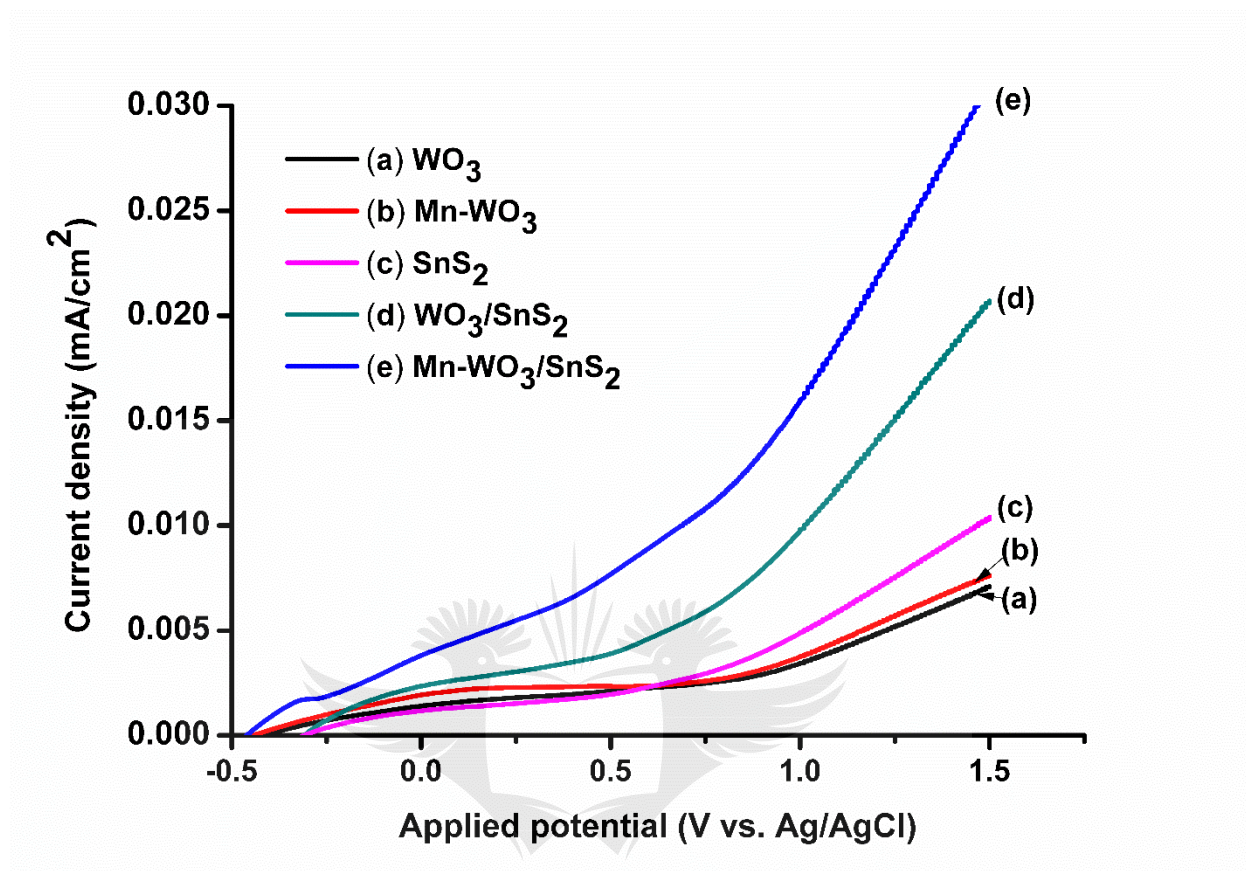
Figure 4.12: Linear sweep voltammetry of **(a)** WO_3, **(b)** $Mn-WO_3$, **(c)** SnS_2, **(d)** WO_3/SnS_2 and **(e)** $Mn-WO_3/SnS_2$ vs. (Ag/AgCl).

4.2.8 Mott-Schottky analysis (M-S)

Mott-Schottky plots was used to study the interfacial capacitance of the nanomaterials. The positive slopes obtained from **Figure 4.13** confirmed that the nanomaterials are all *n-type* semiconductors which uses electrons as major charge carriers. The positive slope for the heterojunctions WO_3/SnS_2 and $Mn-WO_3/SnS_2$ NPs further inferred the formation of *n-n type* heterojunction system. Upon introduction of Mn^{2+} and formation of heterojunction, there was no significant change on the slope of the curves.
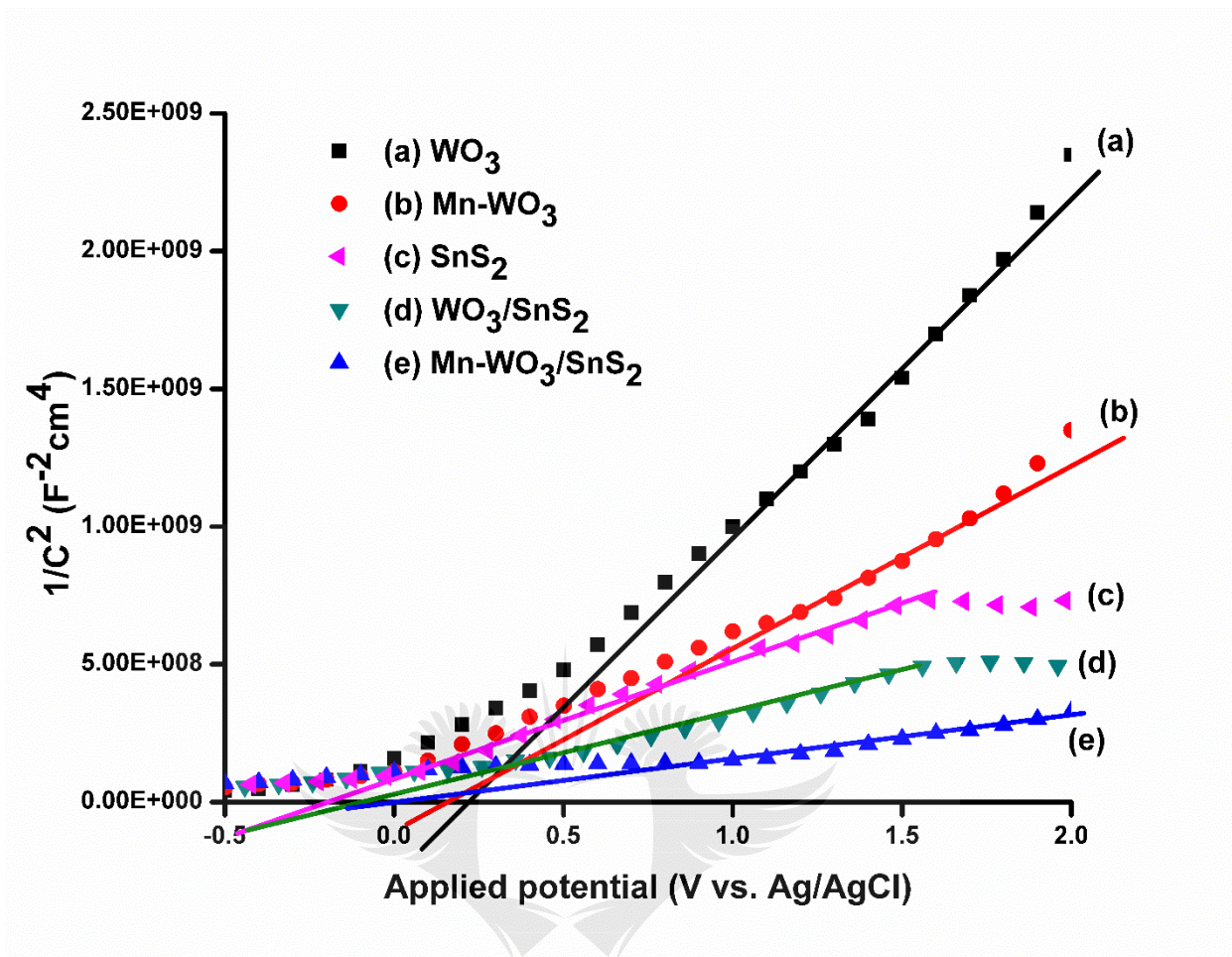
Figure 4.13: Mott-Schottky plots of **(a)** WO$_3$, **(b)** Mn-WO$_3$, **(c)** SnS$_2$, **(d)** WO$_3$/SnS$_2$ and **(e)** Mn-WO$_3$/SnS$_2$ vs. (Ag/AgCl).

The flat-band potential (V_{fb}) was obtained by extrapolating a line on the slope of the graph to the *x*-intercept (1/C^2=0). The flat-band potentials were found to be 0.214 V, 0.159 V, -0.209 V, -0.103 V and -0.039 V corresponding to WO$_3$, Mn-WO$_3$, SnS$_2$, WO$_3$/SnS$_2$ and Mn-WO$_3$/SnS$_2$ respectively.

The flat-band potential in *n-type* semiconductors correspond to the bottom of the conduction band of the semiconductor photocatalyst, which were observed to decrease upon doping and formation of heterojunction (**Figure 4.13(a)-(e)**). The obtained flat-band potential values correspond to the calculated conduction band edges potentials from UV-Vis DRS (**Figure 4.8**).

96

4.2.9 FTIR analysis

This technique was employed to investigate the impurities and functional groups present in the nanomaterials and those brought by doping on the crystalline quality structure of the semiconductor material. Structural changes and functional groups can be observed when Mn^{2+} ion and SnS$_2$ are introduced in the lattice and as a heterojunction, respectively.

The infrared region of 1400-600 cm^{-1} in **Figure 4.14(a)** spectrum correspond to W-O stretching, bending and lattice mode of WO$_3$. **Figure 4.14(a)** shows WO$_3$ spectrum with peaks at wavenumbers around 709, 814, 947 and 1051 cm^{-1} corresponding to O-W-O bridging mode (Abhudhahir & Kandasamy, 2015). Furthermore, the peak at 1637 cm^{-1} correspond to W-OH vibrations.

In Mn doped WO$_3$, the peak at 711 cm^{-1} and 816 cm^{-1} observed on **Figure 4.14(b)** slightly shifted to a higher wavenumber, this was due to crystalline size reduction when Mn^{2+} was intrinsically doped in the WO$_3$ lattice structure. The formed heterojunction between the two photocatalysts was analyzed and **Figure 4.14(d)** spectrum display peaks arising from both WO$_3$ and SnS$_2$ with a shoulder peak at 688 cm^{-1} corresponding to Sn-S vibrations.

Furthermore, the Mn doped WO$_3$/SnS$_2$ spectrum in **Figure 4.14(c)** shows peaks corresponding to WO$_3$ and SnS$_2$ peaks with a Sn-S vibration demonstrated as a shoulder peak at 688 cm^{-1} and slight peak shift to higher wavenumber which were ascribed to the effects imposed by Mn^{2+} ion and the formation of a heterojunction with SnS$_2$ as showed in **Figure 4.14(a)** and **4.14(e)**.

Moreover, **Figure 4.14(e)** illustrates FTIR spectrum corresponding to SnS$_2$ hexagonal phase with peak at 685 cm^{-1}, 1620 cm^{-1} and 3398 cm^{-1} corresponding to Sn-S, Sn-OH and O-H groups, respectively.
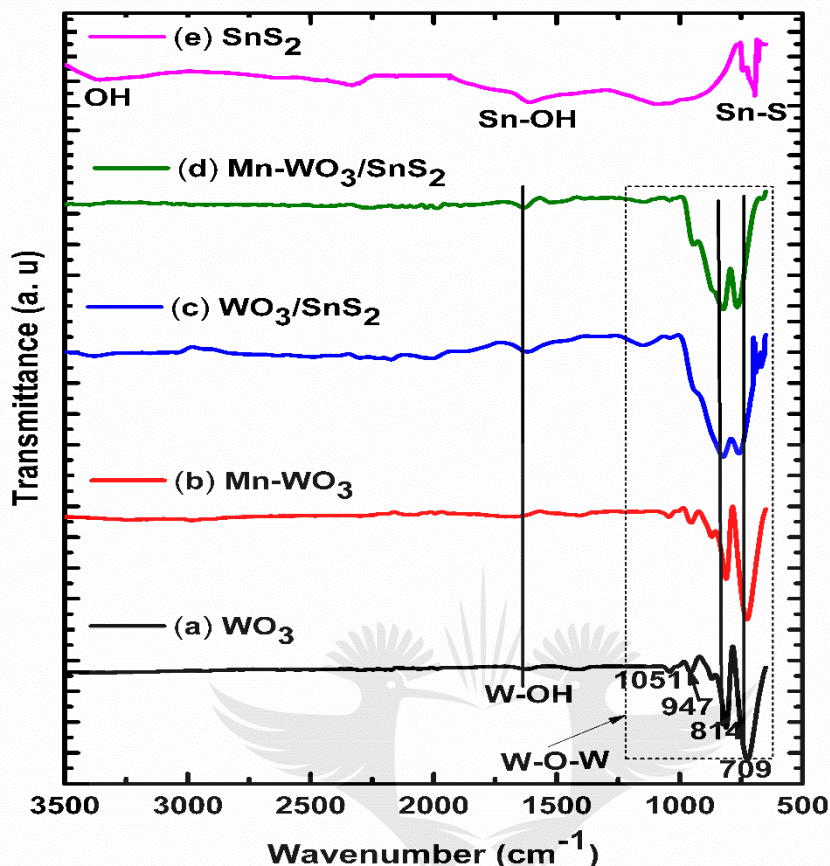
Figure 4.14: FTIR spectra of **(a)** WO$_3$, **(b)** Mn-WO$_3$, **(c)** WO$_3$/SnS$_2$, **(d)** Mn-WO$_3$/SnS$_2$, and **(e)** SnS$_2$.

4.2.10 Thermal Gravimetric Analysis (TGA)

The thermal stability of the nanomaterials was studied using thermal gravimetric analysis coupled to differential scanning calorimetry under constant gas supply. **Figure 4.15** depicts the TGA curves and their derivatives for our nanomaterials. In **Figure 4.15(a)** indicates the TGA curve for WO$_3$ showing weight loss of 1.3wt% at temperature range from 100ºC to 300ºC corresponding to loss of surface adsorbed water molecules. Furthermore, 1.5wt% weight loss was observed at range of temperatures from 350ºC to 550ºC corresponding to evolution of intercalated oxygen molecules.

The observed 4% weight loss between 200 – 290°C for pristine SnS$_2$ was suggestive of the loss of adsorbed water molecules as depicted in (**Figure 4.15(b)**). Further weight loss at temperatures from 300°C to 650°C corresponding to oxidation of Sn-S bond to Sn-O bond.

Upon Mn^{2+} ion introduction in **Figure 4.15(c)**, the weight loss of 0.8wt% (chemically bonded water molecules) was observed in temperature range from 100°C to 250°C. Later observed 2.4wt% weight loss corresponding to oxygen molecules evolution from 300°C to 550°C.

Figure 4.15(d) illustrates the TGA curve of WO$_3$/SnS$_2$ and its derivative. The TGA displays a 52% weight loss corresponding to chemically bonded water molecules from 100°C to 280°C temperature range. A smooth weight loss is observed at temperature ranges from 300°C to 550°C corresponding to oxidation of SnS$_2$ to SnO$_2$.

Figure 4.15(e) depicts a TGA curve and its derivative for Mn-WO$_3$/SnS$_2$. Mn-WO$_3$/SnS$_2$ had weight loss of 8% corresponding to chemically bonded water molecules. Further weight loss is observed at temperatures ranging from 200°C to 400°C. The peak between 500°C to 600°C correspond to further oxidation of Sn-S, by evolving 30% Sulphur molecules. Furthermore, at 600°C is the WO$_3$ onset temperature, which indicates the breaking down or loss of W-O oxygen which amount to 12% weight loss.
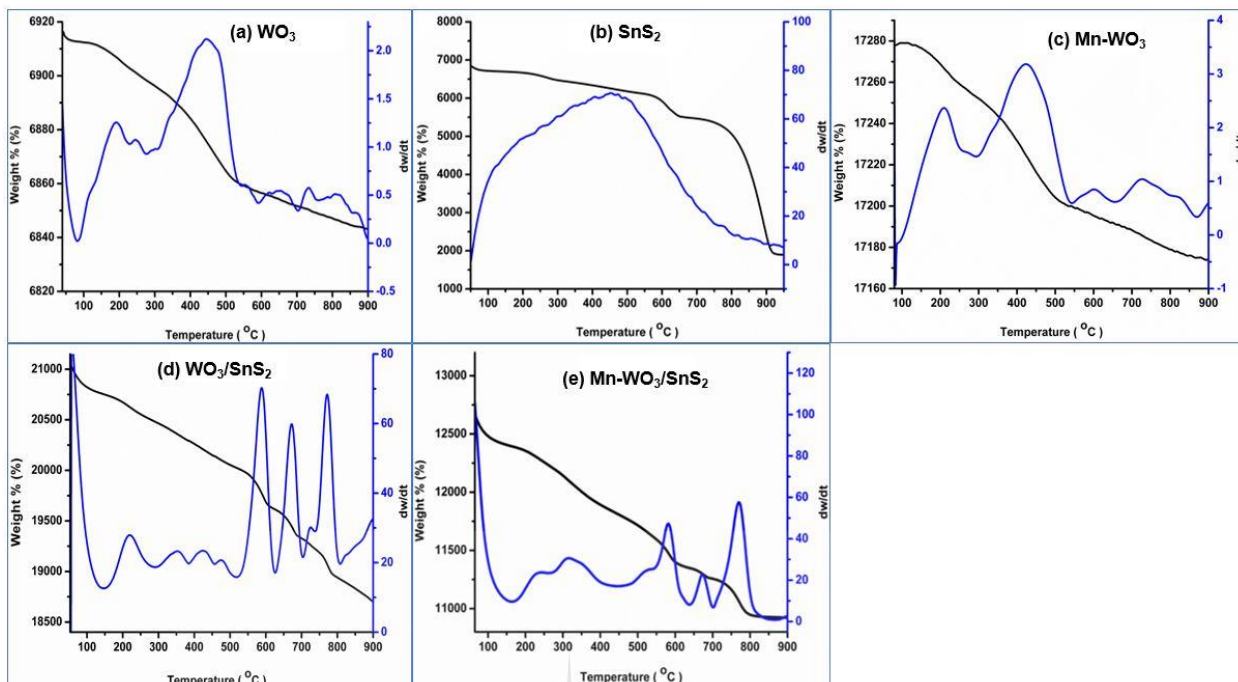
Figure 4.15: Thermal stability spectra of **(a)** WO₃, **(b)** SnS₂, **(c)** Mn-WO₃, **(d)** WO₃/SnS₂, and **(e)** Mn-WO₃/SnS₂.

4.2.11 Surface area and pore volume Analysis

The surface area and pore volume measurements suggest that the nanomaterials could be characterized as type IV isotherm as illustrated in **Figure 4.16(a)**. A type IV isotherm with H1 hysteresis loop is mesoporous, suggesting that the nanomaterials consist of agglomerates.

The surface area of WO₃ was 6.01 m^2/g, which was reduced by doping with Mn^{2+} to 4.41 m^2/g. The reduced surface area was due to the stress induced by larger size atom (Mn) on the unit cell, therefore, the cell reduces its size to compensate the stress, thus reducing the surface area.

The Mn-WO₃/SnS₂ nanoparticles had the highest surface area (77.14 m^2/g) and pore volume (0.0641 cm^3/g) compared to all WO₃ containing nanomaterials (**Table 2**) and (**Appendix 2-4**). The surface area enhancement was due to the incorporation

100

of SnS$_2$ during the formation of the heterojunction. This is because SnS$_2$ NPs are porous adsorbents illustrated by H2 hysteresis loop (**Appendix 5**).
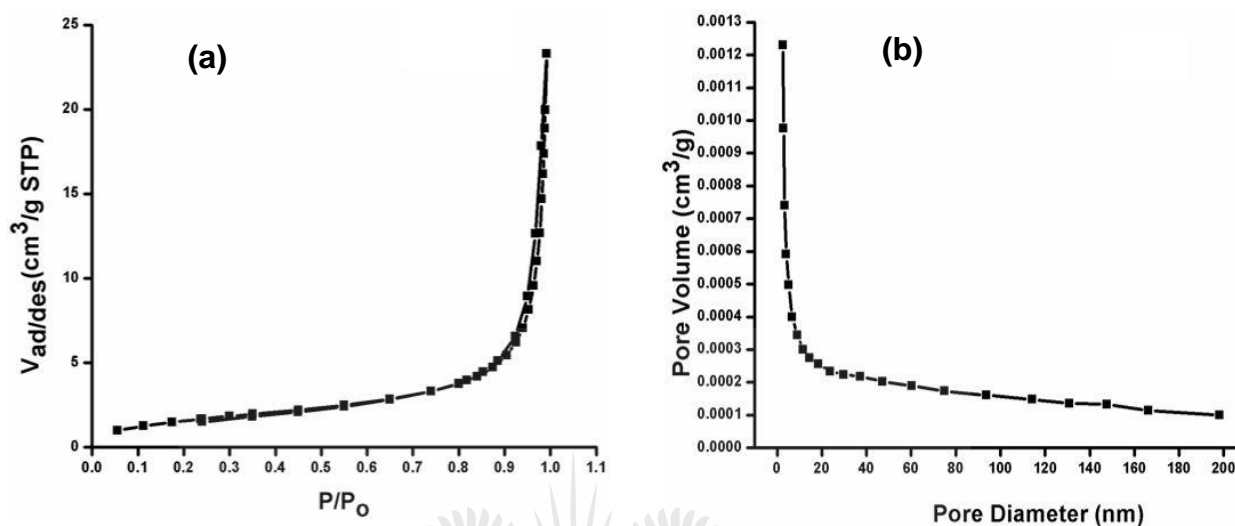
Figure 4.16: **(a)** N$_2$ adsorption-desorption isotherm and **(b)** pore volume graph of WO$_3$.

The high surface area was due to Mn ion reducing the crystalline size and SnS$_2$ which will lead to improved photocatalytic activity of Mn-WO$_3$/SnS$_2$. This is due to adsorption capacity provided by its high surface area and large pore volume which amount to efficient pollutant trapping during adsorption for degradation to take place. Furthermore, high surface area allows the nanomaterials to interact with pollutants at very low concentration.

Table 4.1: The Surface area and Pore Volume of NPs.

Material	S$_{BET}$ (m^2/g)	Pore Volume (cm^3/g)
WO$_3$	6.01	0.0276
Mn-WO$_3$	4.41	0.0294
WO$_3$/SnS$_2$	44.36	0.0514
Mn-WO$_3$/SnS$_2$	77.14	0.0641
Pristine SnS$_2$	99.72	0.0748

4.3 Conclusion

The Mn doped WO$_3$/SnS$_2$ was successfully synthesized resulting in a high crystalline structure. The composite shown rectangular rods and sheets like shapes for both heterojunction photocatalysts. The composite comprises of both hexagonal and monoclinic phases that corresponds to SnS$_2$ and WO$_3$ respectively as confirmed by XRD patterns and Raman spectra. The band gap shifts were displayed in the composite using UV-Vis and red-shift was observed more in the visible region compared to the pristine photocatalysts. The surface area of the WO$_3$ was improved more than 10 times by intrinsic doping with Mn^{2+} ion and formation of the heterojunction with SnS$_2$ to form Mn-doped WO$_3$/SnS$_2$ photocatalyst. The Mn doped composite was fully characterized using microscopic and spectroscopic techniques which confirmed the synthesized composite to be Mn-WO$_3$/SnS$_2$. The Mn-doped WO$_3$/SnS$_2$ showed good electrochemical performance ascribed to its high current density and less interfacial charge resistance observed using electrochemical measurements, which correspond to high charge separation and low photogenerated charge recombination rate observed using photoluminescence measurements.

4.4 References

Abhudhahir, M. H. S & Kandasamy, J. 2015. Photocatalytic effect of manganese doped WO₃ and the effect of dopants on degradation of methylene blue. *Journal of Materials Science: Material Electronics,* 26, pp. 8307-8314.

Afuyoni, M., Nashed, G. & Mohammed, I. 2011. TiO₂ doped with SnO₂ and studing its structurail and electrical properties. *Energy procedia*, 6, pp.11–20.

Batzill, M. 2011. Fundamental aspects of surface engineering of transition metal oxide photocatalysts. *Energy & Environmental Science*, 4(9), pp.3275.

Cai, J., Wu, X., Li, S. & Zheng, F. 2016. Synthesis of TiO₂@WO₃/Au Nanocomposite Hollow Spheres with Controllable Size and High Visible-Light-Driven Photocatalytic Activity. *ACS Sustainable Chemistry and Engineering*, 4(3), pp.1581–1590.

Chae, S. Y., Lee, C. S., Jung, H., Min, B. K., Kim, J. H. & Hwang, Y. J. 2017. Insight into charge separation in WO₃/BiVO₄ heterojunction for solar water splitting. *Applied Materials Interfaces*, 9(23), pp.19780-19790.

Dong, P., Hou, G., Xi, X., Shao, R. & Dong, F. 2017. WO₃-based photocatalysts: morphology control, activity enhancement and multifunctional applications . *Environmental Science: Nano*, 4(3), pp.539–557.

Georgaki, I. V. I., Kenanakis, D. V. G. & Katsarakis, N. 2015. Synthesis of WO₃ catalytic powders : evaluation of photocatalytic activity under NUV/visible light irradiation and alkaline reaction pH. *Journal of Sol-Gel Science and Technology,* 76(1), pp.120-128.

Govindan, V., Imran, H., Dharuman, V. & Sankaranarayanan, K. 2018. Microwave assisted synthesis of Ce-doped SnS₂ nano-flowers with enhanced vitamin-B sensing and photocatalytic activity. *Journal of Materials Science: Materials in Electronics*, 29, pp. 17670-17680.

Harshulkhan, S. M. & Velraj, K. J. G. 2017. Structural and Optical properties of Mg doped Tungsten oxide prepared by Microwave irradiation method. *Journal of Materials Science: Materials in Electronics*, 28(16), pp.11794–11799.

Joshi, U. A., Darwent, J. R., Yiu, H. H. P. & Rosseinsky, M. J. 2011. The effect of platinum on the performance of WO₃ nanocrystal photocatalysts for the oxidation of Methyl Orange and iso-propanol. *Journal of Chemical Technology*

& *Biotechnology*, 86(8), pp.1018–1023.

Klinger, M. 2017. More features, more tools, more CrysTBox. *Journal of Applied Crystallography*, 50, pp.1-9.

Li, J., Du, X., Yao, L. & Zhang, Y. 2014. Synthesis of SnS₂/WO₃ nanocomposite with enhanced photocatalytic activity. *Materials Letters*, 121, pp. 44-46.

Lu, M. W., Wang, Q. F., Miao, J. & Huang, Y. 2016. Synthesis and electrochemical performances of cotton ball-like SnS₂ compound as anode material for lithium ion batteries. *Journal o Materials Technology*, 31(5), pp.281-285.

Mahlalela, L. C., Ngila, J. C. & Dlamini, L. N. 2017. Characterization and stability of TiO₂ nanoparticles in industrial dye stuff effluent. *Journal of Dispersion Science and Technology*, 38(4), pp.584–593.

Marschall, R. 2014. Semiconductor composites: Strategies for enhancing charge carrier separation to improve photocatalytic activity. *Advanced Functional Materials,* 24(17), pp.2421–2440.

Parthibavarman, M. K. M. & Prabhakaran, A. K. S. 2017. One-step microwave synthesis of pure and Mn doped nanoparticles and its structural, optical and electrochemical properties. *Journal of Materials Science: Materials in Electronics*, 28(9), pp.6635–6642.

Shaposhnik, D., Pavelko, R., Llobet, E., Gispert-guirado, F. & Vilanova, X. 2011. Hydrogen sensors on the basis of SnO₂-TiO₂ systems. *Procedia Engineering,* 25, pp.1133–1136.

Simelane, S., Ngila, J. C. & Dlamini, L. N. 2017. The effect of humic acid on the stability and aggregation kinetics of WO₃ nanoparticles. *Particulate Science and Technology*, 35(6), pp.632–642.

Székely, I., Kovács, G., Baia, L., Danciu, V. & Pap, Z. 2016. Synthesis of shape-tailored WO₃ micro-/nanocrystals and the photocatalytic activity of WO₃/TiO₂ composites. *Materials (Basel)*, 9(4), pp.1-14.

Tang, S. J., Moniz, S. J. A., Shevlin, S. A., Martin, D. J., Guo, Z. X. & Tang, J. 2015. Visible-light driven heterojunction photocatalysts for water splitting – a critical review. *Energy Environmental Sciences*, 8, pp.731–759.

Velanganni, S., Pravinraj, S., Immanuel, P. & Thiruneelakandan, R. 2018. Nanostructure CdS/ZnO heterojunction configuration for photocatalytic degradation of Methylene blue. *Physica B: Physics of Condensed Matter*, 534,

pp.56–62.

Xie, Y. P., Liu, G., Yin, L. & Cheng, H. M. 2012. Crystal facet-dependent photocatalytic oxidation and reduction reactivity of monoclinic WO$_3$ for solar energy conversion. *Journal of Materials Chemistry*, 22(14), pp.6746.

Yamamoto, T., Teramachi, A., Orita, A., Kurimoto, A., Motoi, T. & Tanaka, T. 2016. Generation of strong acid sites on yttrium-doped tetragonal ZrO$_2$-supported tungsten oxides: Effects of dopant amounts on acidity, crystalline phase, kinds of tungsten species, and their dispersion. *Journal of Physical Chemistry C*, 120(35), pp.19705-19713.

CHAPTER 5

PHOTODEGRADATION OF CHLORPYRIFOS USING Mn-DOPED MULTI-COMPONENT WO$_3$/SnS$_2$ HETEROJUCTION PHOTOCATALYST IN WATER.

5.1. Introduction

Organophosphate pesticides have been used extensively in South Africa and the world at large due to their ability to combat a vast spectrum of pests. Chlorpyrifos is an organophosphate compound which is used widely as pest control in agriculture and domestically for termites (Glynnis et al. 2012).

Chlorpyrifos (O,O-diethyl O-[3,5,6, -trichloro-2-pyridyl] phosphorothionate) (CPF) is an organophosphorus pesticide extensively used in agricultural and domestic applications (Gao et al. 2017). Chlorpyrifos agricultural application occurs throughout the year to variety of fruits and vegetables. It however, does not readily dissolve in water yet adsorb strongly to soil particles.

It is an enzyme acetylcholinesterase inhibitor and persistent pesticide pollutant. It is class II (moderately hazardous pesticide) pollutant, with half-life of 60 days (Ismail et al. 2013). The pesticide is toxic to humans and other animals when ingested or inhaled, these is attributed to its lipophilic nature. Chlorpyrifos causes delayed peripheral neuropathy in humans, and badly affect the neuro-development in children at high dose (Silvia & Barceló, D. 2006).

The most vulnerable people to chlorpyrifos toxicity are children because of their affection to play and eat everything (Silvia & Barcelo, D. 2006). Various ways children may be exposed to chlorpyrifos include unsafe use in homes by parents in quest to protect them from mosquitos, cockroaches or rodents and in schools and playgrounds, green areas to destroy weeds.

Signs of chlorpyrifos toxicity include headache, nausea, vomiting, diarrhea, abdominal cramps and tumor together with reproductive system disturbance in humans (Sharma et al. 2016).

Due to numerous human and environmental effects caused by chlorpyrifos, different ways to remove this pesticide in the environment were implemented. Those include advanced oxidation processes, biological treatment (fungal and bacterial strains) (Chen et al. 2012, Gupta, et al. 2015).

Bacterial strain such as displayed high chlorpyrifos removal in water of up to 98% (Chen et al. 2012). Though as efficient as it is, the method is strenuous as bacteria require controlled specific conditions such as pH, temperature and a host for optimal function. On the other hand, Ismail et al. 2013 reported the use of advanced oxidation processes (AOPs) that yield 100% removal of chlorpyrifos by using ^{60}Co γ-rays of 30-575 Gy (Ismail et al. 2013).

Although γ-rays are harmful for human health, therefore, this led to implementation of a better and safer method requiring the use of photocatalyst to degrade chlorpyrifos under visible light. So far, zinc and titanium oxides have been used to degrade chlorpyrifos. The results were satisfying with up to 95% for TiO$_2$ and 85% for ZnO chlorpyrifos removal under UV light (Fadaei & Kargar 2013). The photocatalysts suffer from charge recombination and the use of UV light is not viable due to insufficient amount of UV available (4%).

This chapter present the use of metal doped heterojunction with high charge transfer and separation, created to combat the charge recombination, an enemy of effective photocatalytic activity. The composite also absorbs visible light, the naturally abundant light in the solar spectrum. It is to the best of our knowledge, degradation of chlorpyrifos using Mn-WO$_3$/SnS$_2$ has not been reported elsewhere.

5.2. Results and Discussion

5.2.1 Surface charge of nanoparticles

The stability of the nanomaterials in suspensions was studied using electrophoretic light scattering technique. The zeta potentials of the nanomaterials are illustrated in **Figure 5.1**. A steady but gradual change of zeta potential was observed from positive to negative as pH increased from 2 to 11 for all photocatalysts (**Figure 5.1**).

The point of zero charge (pzc) for pristine WO_3 was observed at pH_{pzc} 2.51 which agrees to what is reported by Simelane et al. 2016.

A slight shift of the pzc to higher pH was observed for Mn-WO_3 (pH_{pzc}=3.15). The shift is due to the substitution of W^{6+} by Mn^{2+} metal ions, consequently changing the overall charge of the material. Therefore, adsorbed species onto the surface of the photocatalyst change the surface charge and shift the point of zero charge of the suspended nanoparticles. The point of zero charge for pristine SnS_2 was found to be at pH 5.53 as reported in literature.

Furthermore, the heterojunction (WO_3/SnS_2) displayed point of zero charge (2.67) at lower pH than SnS_2 but higher than WO_3, this was attributed to synergistic effects by both counterparts (WO_3 and SnS_2) in the heterojunction.

Furthermore, introduction of Mn in the heterojunction (Mn-WO_3/SnS_2) shifted the point of zero charge to 2.13, way lower than all other photocatalysts.
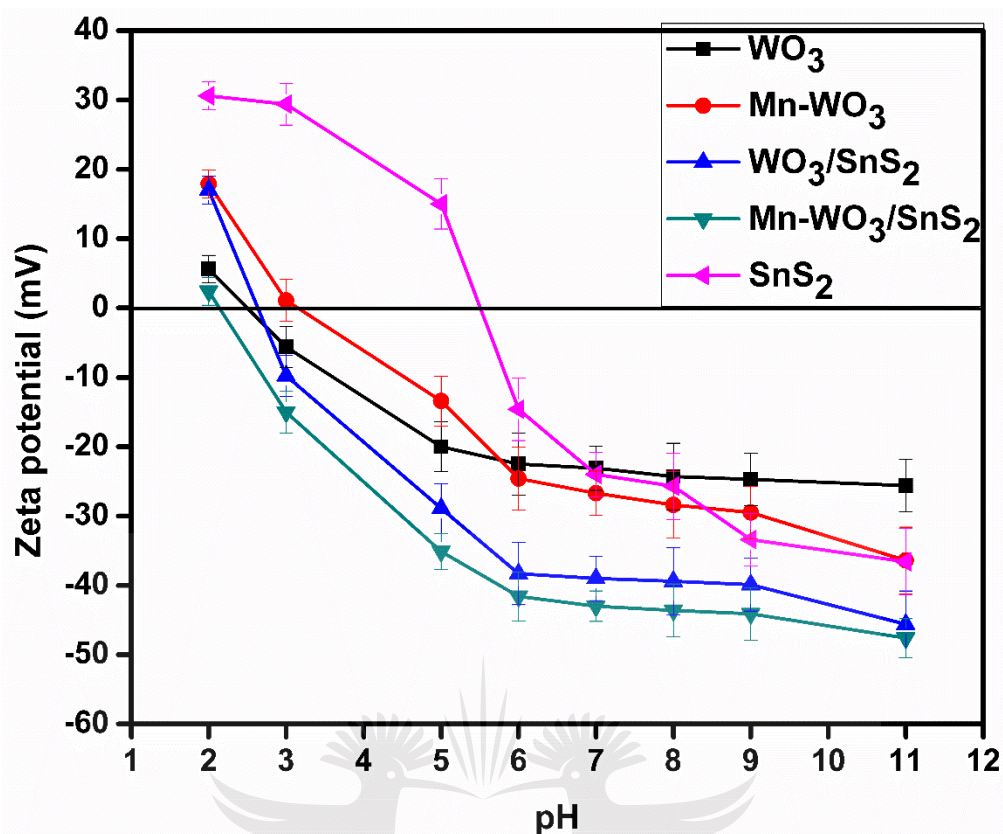
Figure 5.1: Surface charge of the nanoparticles

5.2 Photodegradation of chlorpyrifos in synthetic samples

5.2.1 Photocatalytic degradation of chlorpyrifos

Photodegradation of chlorpyrifos using the synthesized nanoparticles is showed in **Figure 5.2**. The degradation profile of chlorpyrifos indicated an increase in removal by the nanoparticles from WO$_3$ to Mn-WO$_3$/SnS$_2$ photocatalysts. Degradation using pristine WO$_3$ and SnS$_2$ was alluded to more positive VB than chlorpyrifos and more charge mobility respectively. The increased chlorpyrifos removal in doped and heterojunction materials was due to charge separation and more reactive sites provided by SnS$_2$ and Mn respectively. The Mn-WO$_3$/SnS$_2$ nanoparticles showed high removal of chlorpyrifos due to high charge separation and less charge impedance. Therefore, Mn-WO$_3$/SnS$_2$ displayed the best performing photocatalyst with up to 95.90% chlorpyrifos removal calculated using **Equation 3.5**.
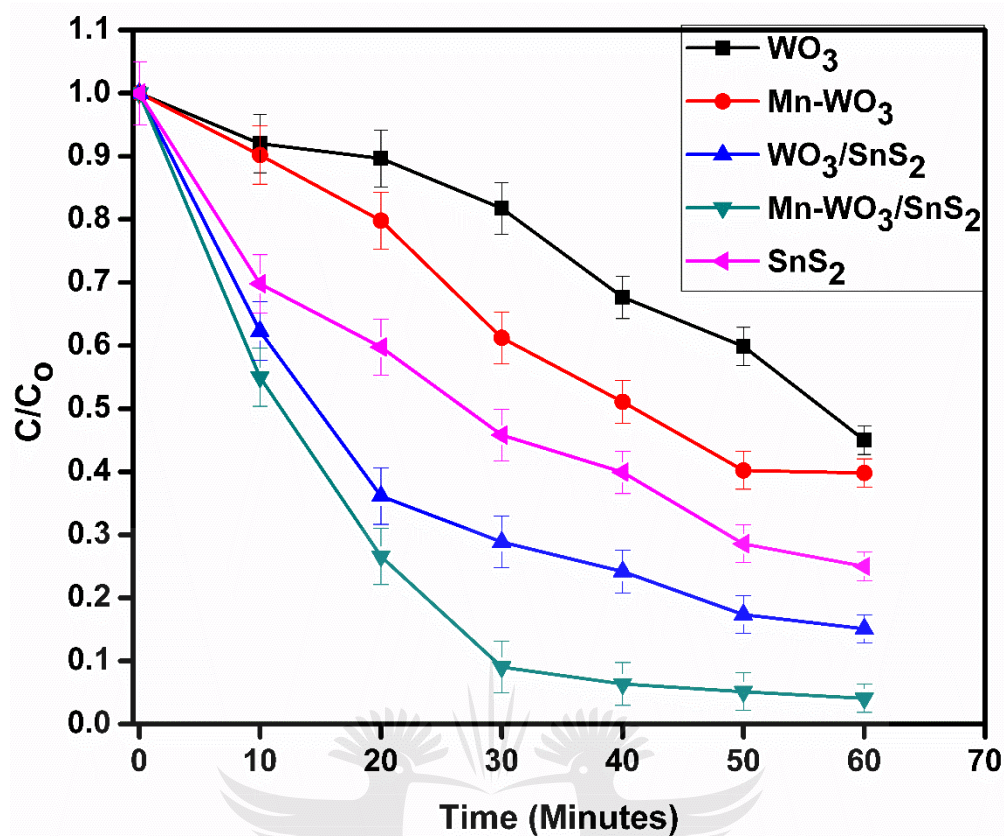
Figure 5.2: Degradation of chlorpyrifos (1000 ppb) using the different photocatalysts at pH=5.8 and 0.1 g photocatalyst.

Figure 5.3 display the percentage removal of chlorpyrifos in water within a period of 60 minutes. The removal efficiency of chlorpyrifos by using the nanoparticles resulted in 56.80%, 60.20%, 75.00%, 84.88% and 95.90% for WO_3, Mn-WO_3, SnS_2, WO_3/SnS_2 and Mn-WO_3/SnS_2 respectively.

Corresponding to percentage chlorpyrifos removal is the reaction kinetics presenting the rate constant (K) of the reaction using the respective photocatalysts (**Figure 5.4**) was 9.3×10^{-3} $M^{-1}min^{-1}$ to 209×10^{-3} $M^{-1}min^{-1}$ for WO_3 and Mn-WO_3/SnS_2 respectively.

The photodegradation reaction was fitted to **Equation 3.6** from which the rate constant $k(M^{-1}min^{-1})$ was calculated from the gradient of the plot of 1/[C] against time (t). The reaction kinetics which lead to determination of rate constant followed a second order reaction pathway.
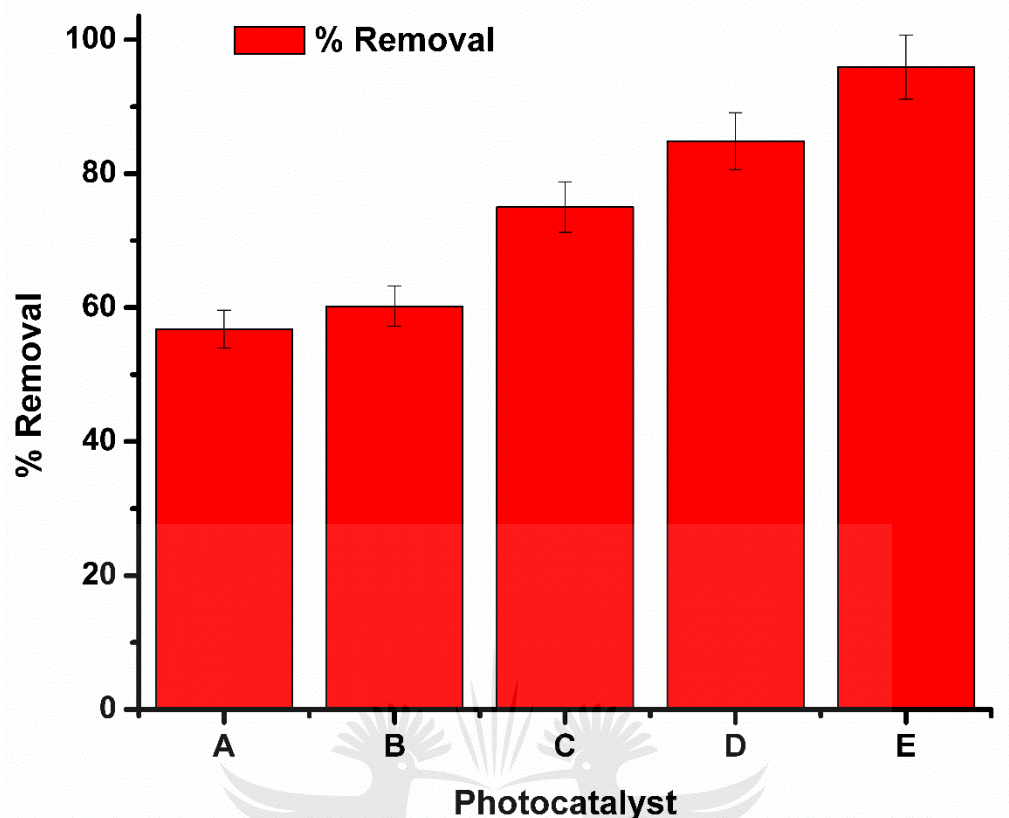
Figure 5.3: Percentage removal of chlorpyrifos (1000 ppb) using 0.1 g of (**A**) WO_3, (**B**) Mn-WO_3, (**C**) SnS_2, (**D**) WO_3/SnS_2 and (**E**) Mn-WO_3/SnS_2.

The rate constants were 9.3×10^{-3} $M^{-1}min^{-1}$, 14.3×10^{-3} $M^{-1}min^{-1}$, 25.0×10^{-3} $M^{-1}min^{-1}$, 47.4×10^{-3} $M^{-1}min^{-1}$ and 209.5×10^{-3} $M^{-1}min^{-1}$ corresponding to WO_3, Mn-WO_3, SnS_2, WO_3/SnS_2 and Mn-WO_3/SnS_2 respectively (**Figure 5.4**).
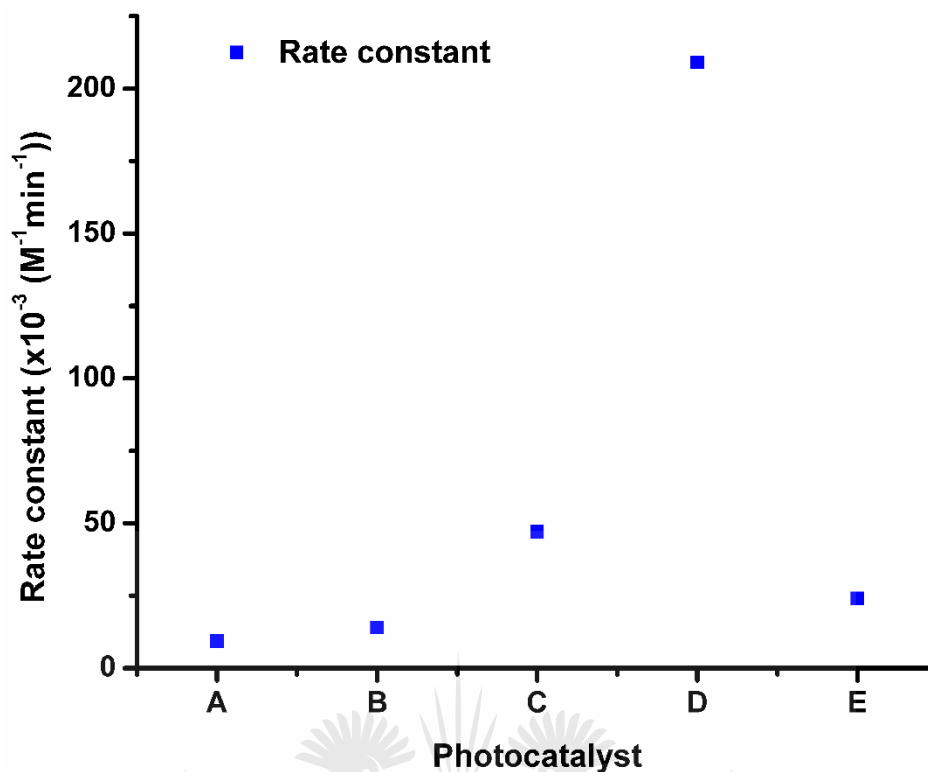
Figure 5.4: Rate constants of (**A**) WO_3, (**B**) Mn-WO_3, (**C**) WO_3/SnS_2, (**D**) Mn-WO_3/SnS_2 and (**E**) SnS_2.

The linear plot for Mn-WO_3/SnS_2 nanoparticles kinetic studies is illustrated in **Figure 5.5**. The rate constant is 209.5×10^{-3} $M^{-1}min^{-1}$ and R^2 is 0.9656.
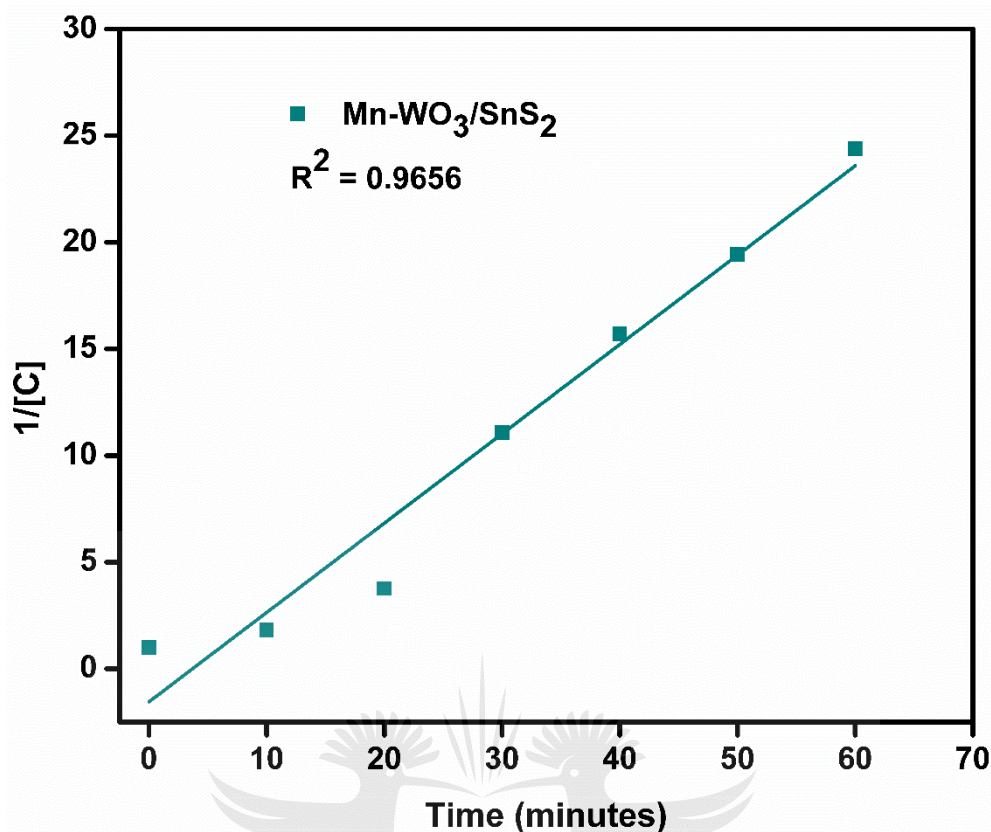
Figure 5.5: Photodegradation kinetics of chlorpyrifos using Mn-WO₃/SnS₂.

5.2.2.2 Effect of pH on photocatalytic activity of Mn-WO₃/SnS₂ on the degradation of chlorpyrifos

Surface charge of the nanoparticles in a suspension is influenced by the pH of the solution. Photodegradation of chlorpyrifos using Mn-WO₃/SnS₂ nanoparticles increased with an increase in the pH of the initial solution as illustrated in **Figure 5.6**. The point of zero charge for Mn-WO₃/SnS₂ is at pH_{pzc}= 2.13 and above that is increasingly negative displayed by **Equation 5.2**.

$M\text{-}OH + H^+ = M\text{-}OH_2^+$ (pH<PZC)   **5.1**

$M\text{-}OH = M\text{-}O^- + H^+$ (pH>PZC)   **5.2**

The increase in the removal was also caused by the increase in level of deprotonation of the nanoparticles at high pH that influence the negative charge on the surface of the photocatalyst, consequently leading to high chlorpyrifos

adsorption. That was also favored by positive charge of chlorpyrifos in alkaline solutions from pH 5.8 as reported in literature. There is a transfer of holes from the inner part of the nanoparticles to the surface, whereby OH^- scavenge photogenerated holes and therefore yield very oxidative species such as $^{\cdot}OH$ radicals. The percentage removal of chlorpyrifos obtained in 60 minutes was 85.6%, 94.3%, 99.8% and 99.0% at pH 3, pH 5.8, pH 7 and pH 9 respectively (**Figure 5.6**). Therefore, pH 7 was the optimum pH for chlorpyrifos removal using Mn-WO₃/SnS₂ nanoparticles and was used in the next sections. Hou at al. 2018 also reported pH 7 for optimum chlorpyrifos removal (Hou et al. 2018).

The increase in the removal was due to the increased electrostatic attraction between the photocatalyst and the chlorpyrifos that occurs when pH was increased (Fadaei & Kargar 2013). This causes an easy surface attachment which implies that holes can oxidize chlorpyrifos directly and creates hydroxyl and superoxide radicals for further oxidation. As pH increased also the surface charge of the nanoparticles became more negative, which caused increased electrostatic attraction between the nanoparticles and chlorpyrifos.
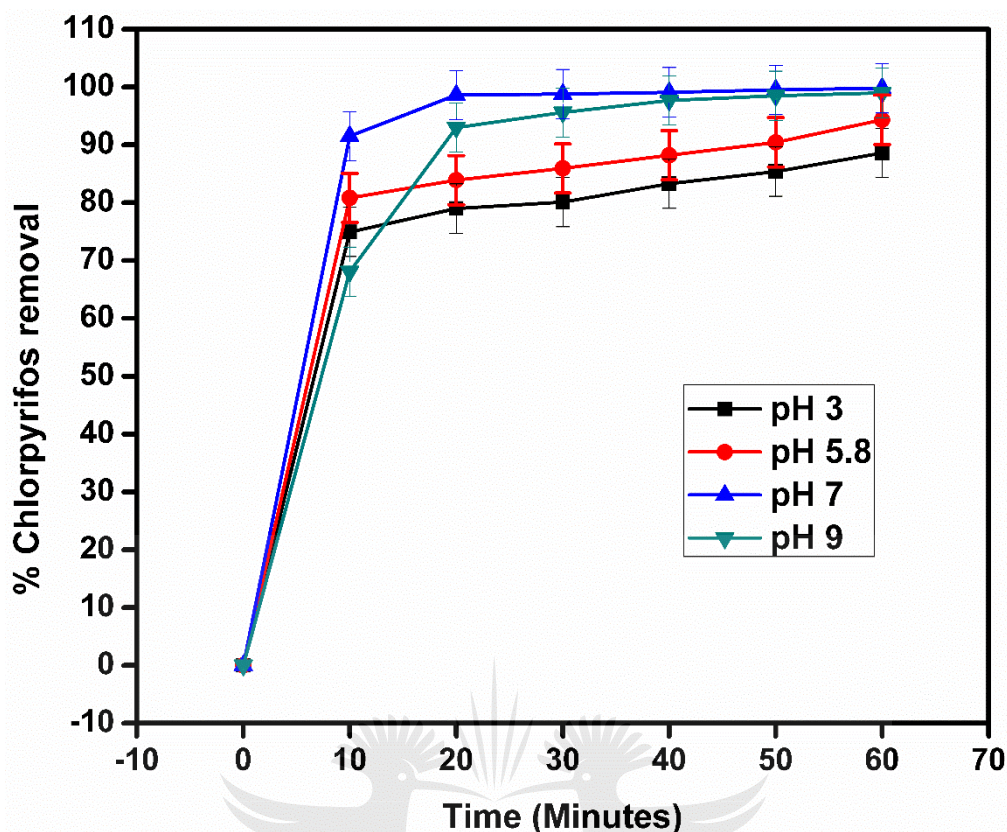
Figure 5.6: Degradation of 1000 ppb chlorpyrifos using 0.1 g of Mn-WO_3/SnS_2 at different pH values.

5.2.2.3 Effect of initial CPF concentration on the removal of chlorpyrifos

The effect of initial chlorpyrifos concentration on the photocatalytic removal was studied and results showed in **Figure 5.7**. The highest removal of 99.99% was achieved at 100 ppb of chlorpyrifos concentration, followed by 1000 ppb at 99.95% compared to 94.40, 87.51 and 84.38% of 5 ppm, 10 ppm and 20 ppm respectively. the 1000 ppb was chosen as the best, because it is the highest concentration that achieved high percentage removal.

The decrease in the removal of chlorpyrifos was alluded to opacity caused by the high chlorpyrifos concentration, which unable the photocatalyst from utilizing the irradiated light to produce reactive species for degradation. Again, the high concentration scatters the light, therefore inducing the screening effects (Fadaei & Kargar 2013).
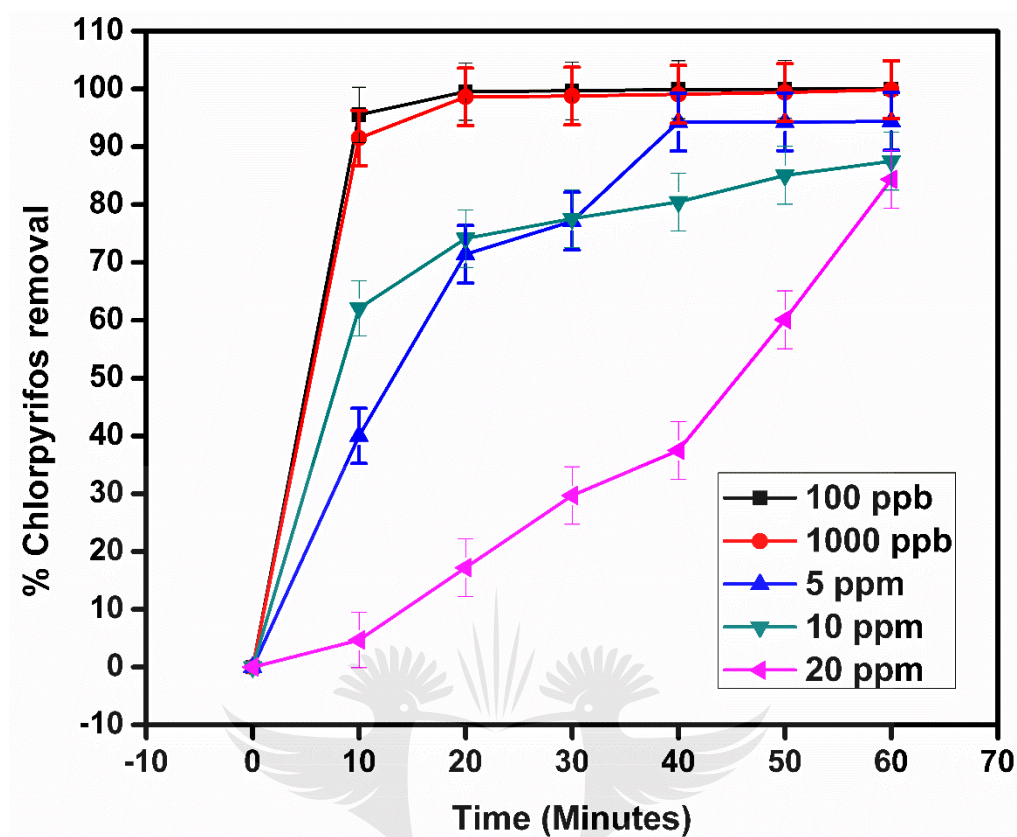
Figure 5.7: Effect of initial concentration on the removal of chlorpyrifos (1000 ppb) at pH 7 using 0.1 g Mn-WO₃/SnS₂.

5.2.2.4 Effect of initial photocatalyst loading on the removal of chlorpyrifos

Initial photocatalyst loading effect on the photoactivity was studied and the results are presented in **Figure 5.8**. The photoactivity of Mn-WO₃/SnS₂ increased when 0.5 g photocatalyst was used, then decreased when the photocatalyst loading was 1 g. The decrease is a result of particle aggregation caused by high amount of the photocatalyst (Fadaei & Kargar 2013).

Therefore, the nanoparticles caused light scattering and screening effects which reduce the specific activity of the photocatalyst. High concentration of nanoparticles also cause opacity, which prevents further illumination of the photocatalyst. This resulted in a decrease in chlorpyrifos removal when 2 g of Mn-WO₃/SnS₂ was used reaching up to 85%. Compared to 0.1 g, 0.5 g, and 1 g removing up to 99.95%,

99.98% and 99.99% respectively. 1 g was the best performing as it reached 98% removal within 30 minutes of reaction time.
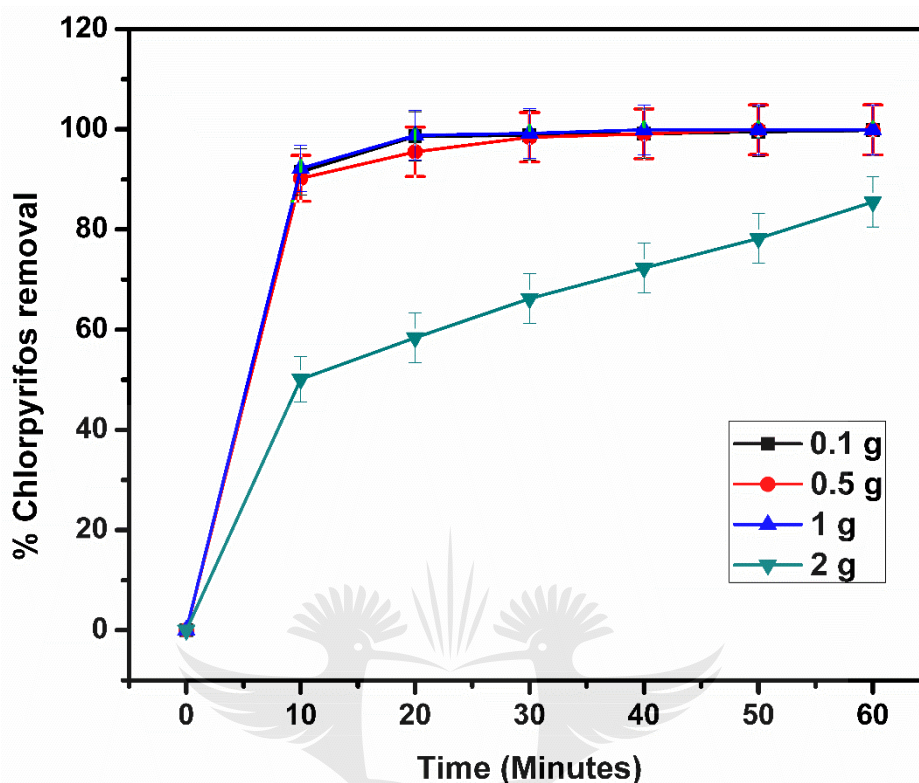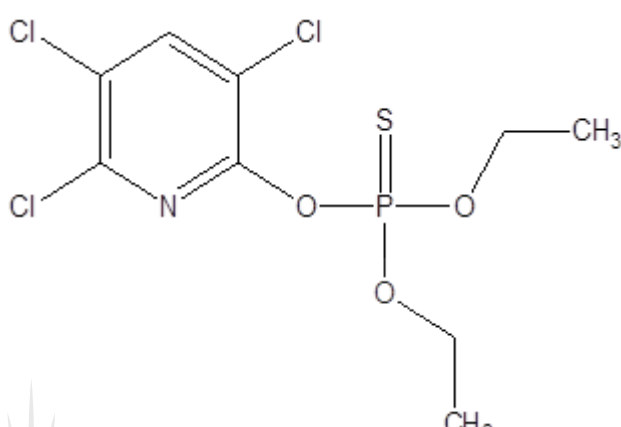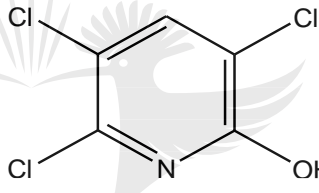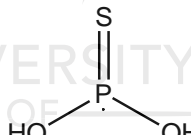

**Figure 5.8**: Effect of initial photocatalyst loading on the photodegradation of chlorpyrifos.

5.2.2.5 Degradation and mechanistic pathway

The mechanistic and proposed degradation pathway was evaluated, and the results were tabulated in **Table 5.1** and **Figure 5.9**. The products obtained were 3,5,6-trichloropyridin-2-ol (TCP) and O,O-dihydrogen phosphorothioite. Chlorpyrifos peak disappear after 30 minutes of the reaction, leaving its major degradation by-product (TCP) and O,O-dihydrogen phosphorothioite.

After 60 minutes the chlorpyrifos and TCP peaks do not appear, only O,O-dihydrogen phosphorothioite peak and no other by-product, which implies that there is a complete degradation of chlorpyrifos TCP in the synthetic water.

117

Table 5.1: Major photodegradation by products of chlorpyrifos obtained in 60 minutes.

Degradation product	Product m/z	Structure of product
Chlorpyrifos	351.70	
3,5,6-Trichloropyridin-2-ol	199.85	
O,O-dihydrogen phosphorothioite	97.00	
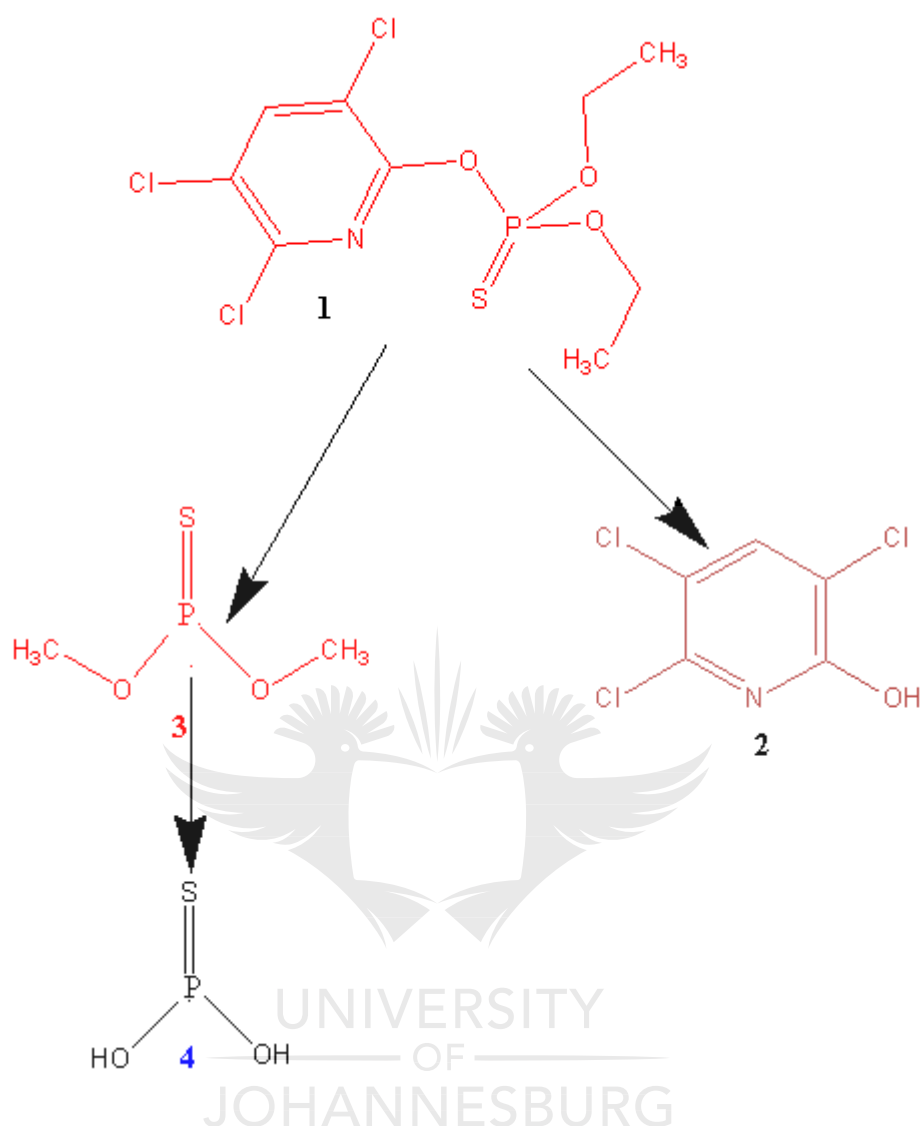
Figure 5.9: Proposed degradation pathway of chlorpyrifos

5.3 Conclusion

Chlorpyrifos have been applied extensively in agriculture, both in South Africa and other parts of the world to fight against pests, therefore, find its way into water systems. Chlorpyrifos removal in synthetic water was investigated using Mn-WO_3/SnS_2 nanoparticles. The removal was due to enhanced charge separation, high charge transfers and high electrostatic attraction between the nanoparticles and chlorpyrifos.

Mn-WO$_3$/SnS$_2$ nanoparticles resulted in 94% removal whereas, WO$_3$, SnS$_2$, Mn-WO$_3$ and WO$_3$/SnS$_2$ resulted in 56.8%, 75%, 60.2% and 84.9%. Factors which may impact on the degradation of chlorpyrifos were also studied such as pH, initial photocatalyst loading and initial chlorpyrifos concentration. From the results obtained, pH 7, 1 g Mn-WO$_3$/SnS$_2$ and 1000 ppb were the optimum conditions which resulted in 99.99% chlorpyrifos removal.

The degradation pathway was also investigated, whereby 3,5,6-trichloropyridin-2-ol and O,O-dihydrogen phosphorothioite were observed. Furthermore, after 6o minutes of the reaction, only O,O-dihydrogen phosphorothioite was detected. This implies that both chlorpyrifos and TCP were completely degraded. The results suggest that our material, Mn-WO$_3$/SnS$_2$ can completely degrade chlorpyrifos and its major degradation product.

5.4. References

Chen, S., Liu, C., Peng, C., Liu, H., Hu, M. & Zhong, G. 2012. Biodegradation of chlorpyrifos and its hydrolysis product 3,5,6-Trichloro-2-pyridinol by a new fungal strain *cladosporium cladosporioides* Hu-01. *PLoS ONE*, 7(10), pp.1–12.

Fadaei, A. & Kargar, M. 2013. Photocatalytic degradation of chlorpyrifos in water using titanium dioxide and zinc oxide. *Fresenius Environmental Bulletin*, 22(8), pp.2442–2447.

Gao, J., Naughton, S. X., Beck, W. D., Hernandez, C. M., Wu, G., Wei, Z., Yang, X., Bartlett, M. G. & Terry, A. V, Jr. 2017. Chlorpyrifos and chlorpyrifos oxon impair the transport of membrane bound organelles in rat cortical axons. *Neurotoxicology*, 62, pp.111–123.

Glynnis, R., Perry, M., Lee, M. M., Hoffman, E., Delport, S. & Dalvie, M. A. 2012. Farm residence and reproductive health among boys in rural South Africa. *Environment International*, 47, pp.73–79.

Gupta, V. K., Eren, T., Atar, N., Yola, M. L., Parlak, C. & Karimi-Maleh, H. 2015. $CoFe_2O_4@TiO_2$ decorated reduced graphene oxide nanocomposite for photocatalytic degradation of chlorpyrifos. *Journal of Molecular Liquids*, 208, pp. 122-129.

Hou, J., Zhang, F., Wang, P., Wang, C., Chen, J., Xu, Y., You, G., Zhou, Q. & Li, Z. 2018. Enhanced anaerobic biological treatment of chlorpyrifos in farmland drainage with zero valent iron. *Chemical Engineering Journal*, 336, pp.352–360.

Ismail, M., Khan, H. M., Sayed, M. & Cooper, W. J. 2013. Advanced oxidation for the treatment of chlorpyrifos in aqueous solution. *Chemosphere*, 93(4), pp.645–651.

Sharma, B., Saxena, S., Datta, A. & Arora, S. 2016. Spectrophotometric analysis of degradation of chlorpyrifos pesticide by indigenous microorganisms isolated from affected soil. *International Journal of Current Microbiology and Applied Sciences*, 5(9), pp.742–749.

Silvia, M.D. & Barceló, D. 2006. Highly selective sample preparation and gas chromatographic – mass spectrometric analysis of chlorpyrifos, diazinon and their major metabolites in sludge and sludge-fertilized agricultural soils. *Journal*

of Chromatography A, 1132, pp.21–27.

CHAPTER 6

CONCLUSION AND RECOMMENDATIONS

6.1. Conclusion

Conclusions were made based on the aim and objectives followed in this study that it was successful. The following conclusions were drawn:

The nanoparticles were successfully prepared via a hydrothermal method and characterized using XRD, HRTEM, Raman to be WO_3, SnS_2, Mn-WO_3, WO_3/SnS_2 and Mn-WO_3/SnS_2. Their optical and electrochemical properties were also studied using UV-Vis-DRS, EIS and PL.

A manganese-doped tungsten trioxide/tin disulphide (Mn-WO_3/SnS_2) heterojunction composite obtained as a mixture of monoclinic and hexagonal phases and average crystallite size of 40 nm. It also displayed improved/enhanced visible light absorption (582 nm from 466 nm of WO_3) and low emission peak corresponding to low charge recombination.

Furthermore, EIS spectra illustrated small semi-circle diameter corresponding to less electrode-electrolyte charge transfer resistance of Mn-WO_3/SnS_2 compared to other nanoparticles. This was alluded to Mn doping acting as electron sink and formation of heterojunction with SnS_2 which further assisting in charge separation.

The crystalline rectangular sheets and rods morphology of the nanoparticles was revealed by FESEM and HRTEM. Doping with Mn and SnS_2 did not distort the nanoparticles morphology. The surface area increased from 6 m^2/g of WO_3 to 77 m^2/g. The nanoparticles were found to be mesoporous with pore volumes ranging from 0.0276 to 0.0748 observed through BET analysis.

Zeta potential measurements showed point of zero charge in the pH range of 2.21 to 5.53. $Mn-WO_3/SnS_2$ had the lowest point of zero charge of pH 2.21, due to the contributing charge effects brought by Mn and SnS_2. In all the nanoparticles, the surface charge gradually increased to more negative with an increase in pH from 2 to 11.

The photocatalytic activity of the nanomaterials was evaluated through photodegradation of organophosphate pesticide in synthetic water samples. $Mn-WO_3/SnS_2$ displayed high photodegradation of chlorpyrifos achieving 95% removal within 60 minutes. This was outstanding compared to the 56% removal achieved using WO_3 nanoparticles. Other nanoparticles achieved 65, 75 and 85% for $Mn-WO_3$, SnS_2 and WO_3/SnS_2.

Therefore, the best performing $Mn-WO_3/SnS_2$ nanoparticles was used to optimize conditions such as pH, initial chlorpyrifos concentration and initial photocatalyst loading. The optimized conditions were as follows: pH 7, initial chlorpyrifos concentration of 1000 ppb and initial photocatalyst loading of 1 g. The percentage removal of chlorpyrifos under optimum conditions using $Mn-WO_3/SnS_2$ achieved 100% within 60 minutes.

Furthermore, the reaction kinetics illustrated a second order kinetics with reaction rate of 0.209 $M^{-1}s^{-1}$. The degradation pathway deduced from the results showed that TCP is the major degradation by product which further degrade to innocuous substances. This resulted in a complete degradation of chlorpyrifos and its major degradation by product TCP within 60 minutes.

6.2. Recommendations

From the study, gaps have been identified for future research and development such as:

Identifying the major degradation species responsible for oxidation of chlorpyrifos using scavengers.

Degradation of chlorpyrifos in a more complex matrix (real samples) such as river water and/or wastewater should be conducted to evaluate the nanoparticles efficiency in removing chlorpyrifos. Furthermore, this heterojunction photocatalyst system can be used especially by people in the Western Cape where water is scarce. However, factors such as colloidal matter, bacterial strains, other organic pollutants competition and water opacity must be investigated because they may hinder the photocatalytic degradation of chlorpyrifos using the heterojunction photocatalyst. After all conditions optimized, the heterojunction photocatalyst can be incorporated into the chemical process chamber of the wastewater treatment plant to assist in water treatment.

A study should be conducted to evaluate the effect of the ratio of the heterojunction components in the efficiency of $Mn-WO_3/SnS_2$ when the amount of SnS_2 or $Mn-WO_3$ ratio is varied from 10, 20, 30, 40 and 50% m/m in $Mn-WO_3:SnS_2$.

The recyclability and reusability studies to be conducted to check on how long the nanoparticles remain efficient.

Studying the degradation of TCP alone is important due to its high toxicity compared to chlorpyrifos. This will specifically determine the fragments leading to a complete mineralization.
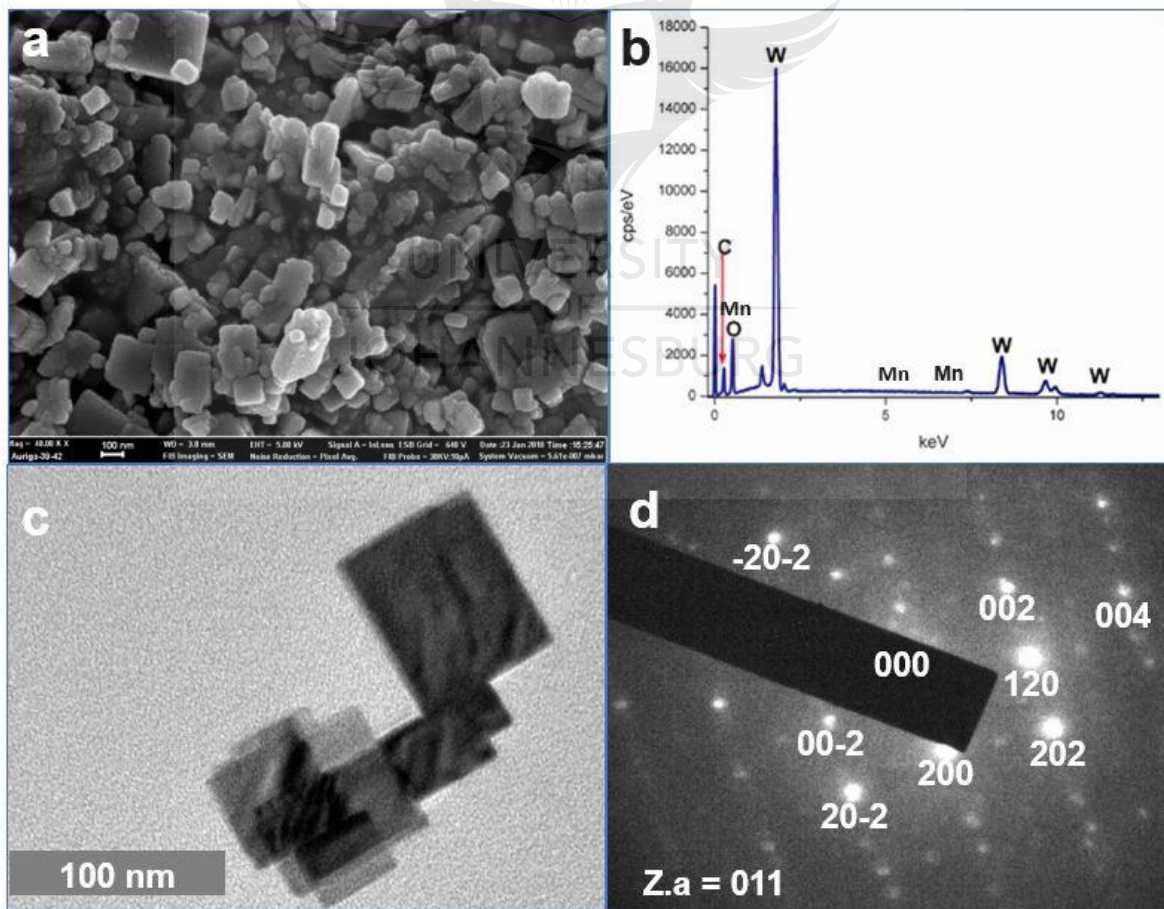
APPENDICES

Appendix A: Average crystallite size of the materials.

Table A1 displays the average crystallite sizes of the nanoparticles.

Material	Average Crystallite Size (nm)
Pristine WO_3	43
Mn-WO_3	40
Mn-WO_3/SnS_2	40
WO_3/SnS_2	40
Pristine SnS_2	17

Appendix B: Morphology of Mn-WO_3.

Figure (a) FESEM image, **(b)** EDS spectrum, **(c)** HRTEM image and **(d)** SAED image of Mn-WO_3.

Appendix C: STEM images of Mn doped WO₃ nanoparticles showing distribution of atoms.
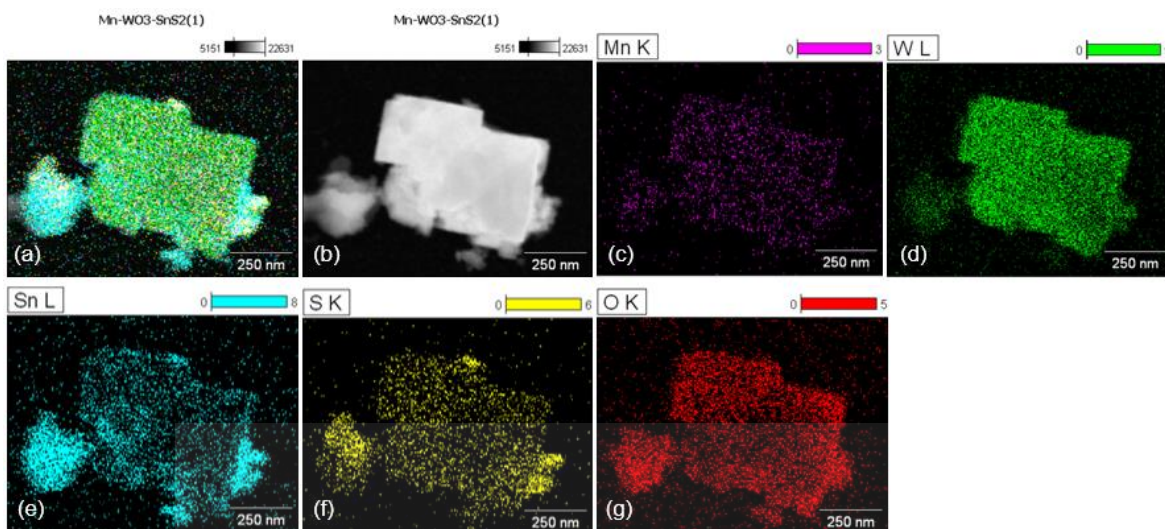
Figure displays the mapping image for Mn doped WO₃ nanoparticles: (a) overall mapping, (b) STEM image of Mn-WO₃/SnS₂, (c) Mn content in the nanoparticles, (d) W content, (e) Sn content, (f) S content and (g) O content of in the nanoparticles.

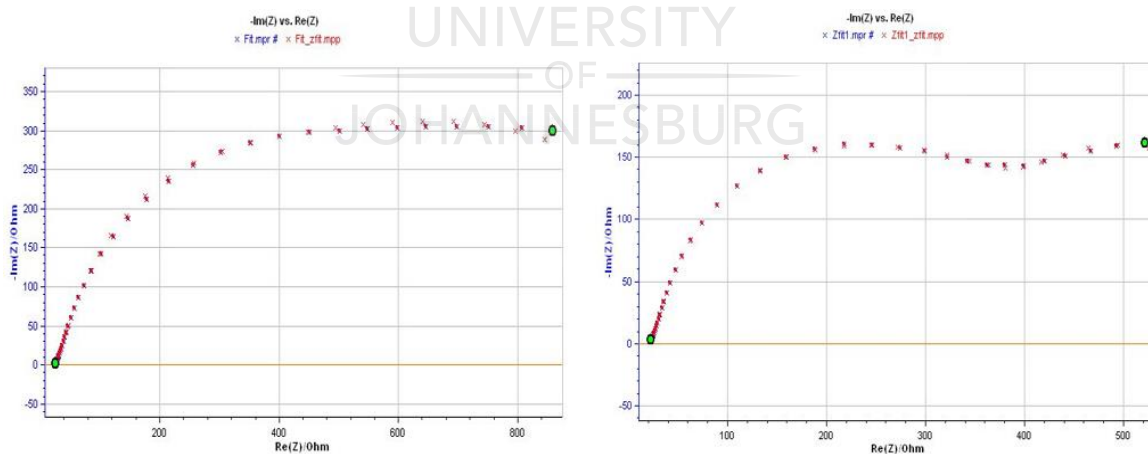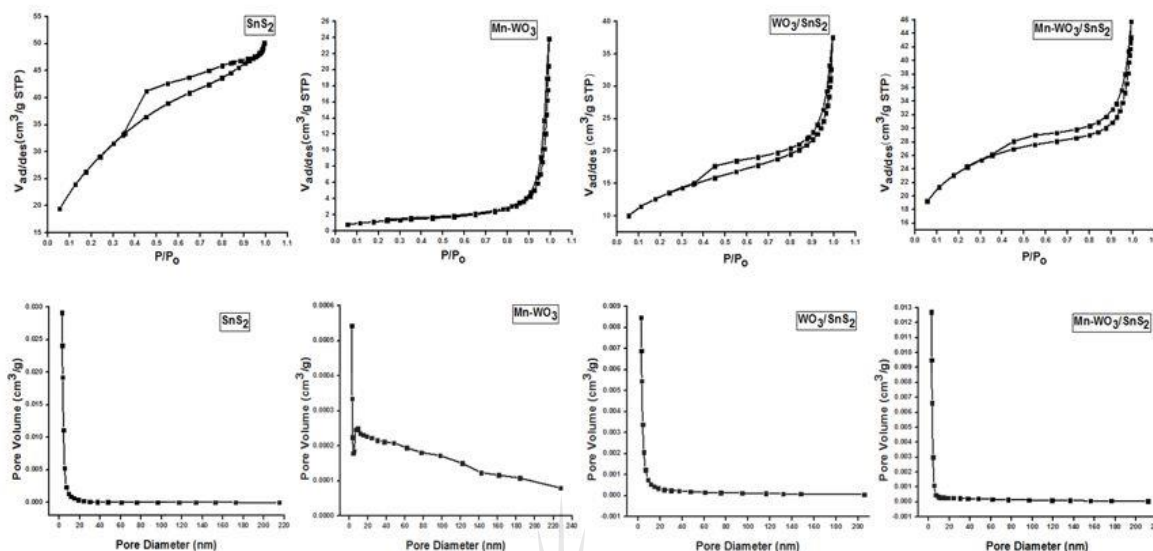## Appendix D: The fitted EIS spectra obtained through EC-lab software.

Figure displays the EIS spectra showing the fitted spectra when obtaining the Randles circuit for (a) WO₃ and Mn-WO₃ (b) SnS₂, WO₃/SnS₂ and Mn-WO₃/SnS₂.

Appendix E: BET surface area of the nanoparticles with their respective pore volume graphs.

Figures ((a)-(d)) represent graphs of BET surface area and ((e)-(h)) represents the respective pore volume graphs of SnS$_2$, Mn-WO$_3$, WO$_3$/SnS$_2$ and Mn-WO$_3$/SnS$_2$.

Appendix F: Chlorpyrifos calibration curve.
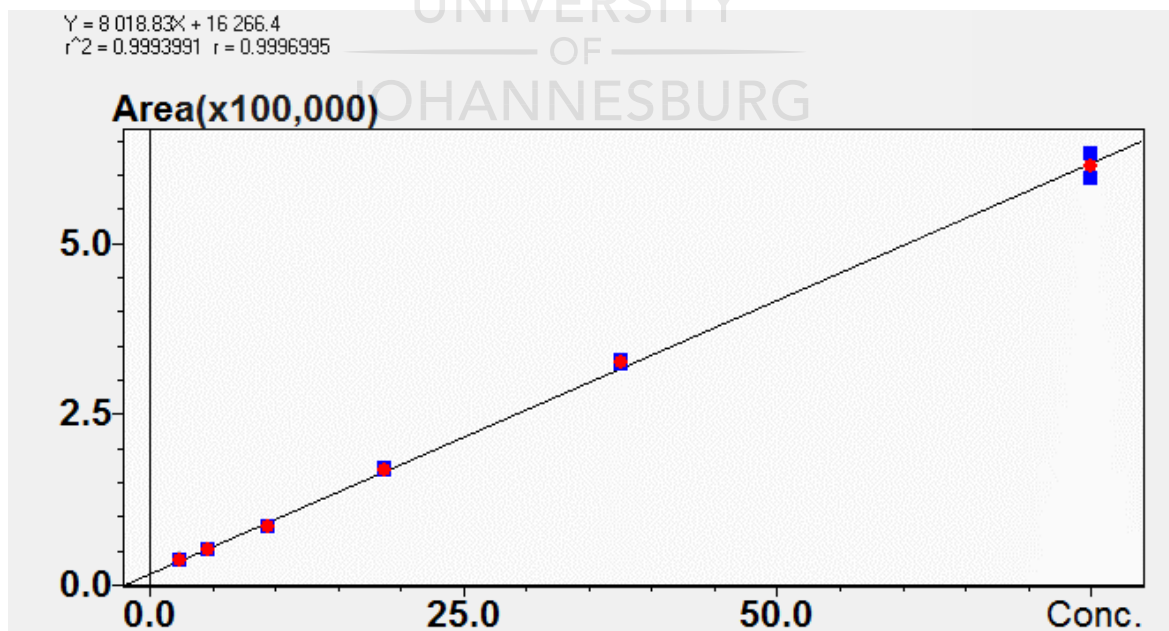
The figure displays the calibration curve of chlorpyrifos from 3.125 to 75 ppb.

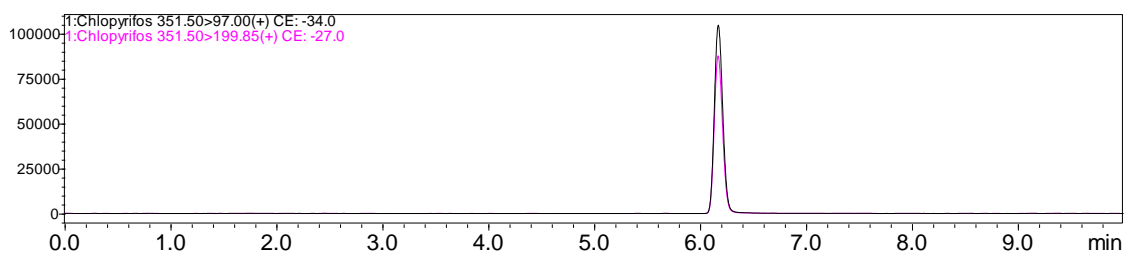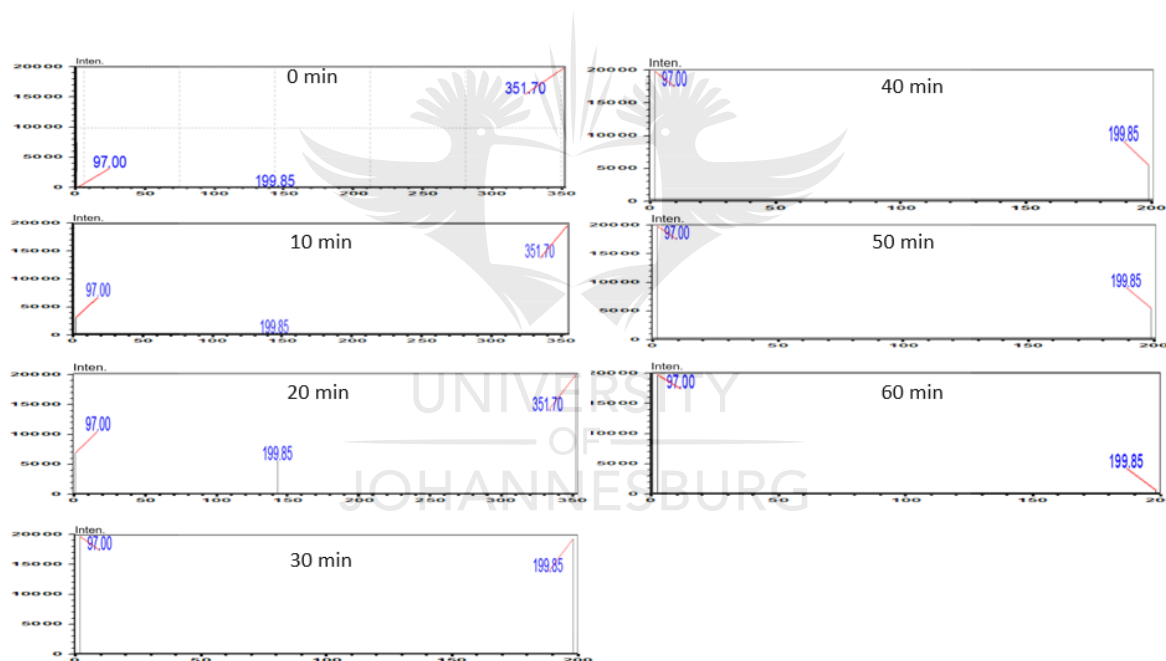## Appendix G: Chlorpyrifos chromatogram.

Figure illustrates chlorpyrifos chromatogram with retention time of 6.25 minutes in formic acid.

Appendix H: Mass spectra showing by-products and their respective m/z values during the reaction period.

This figure displays mass spectra showing m/z ratios from 0 to 60 minutes.

Appendix I: Reaction kinetics graphs of the photocatalysts.
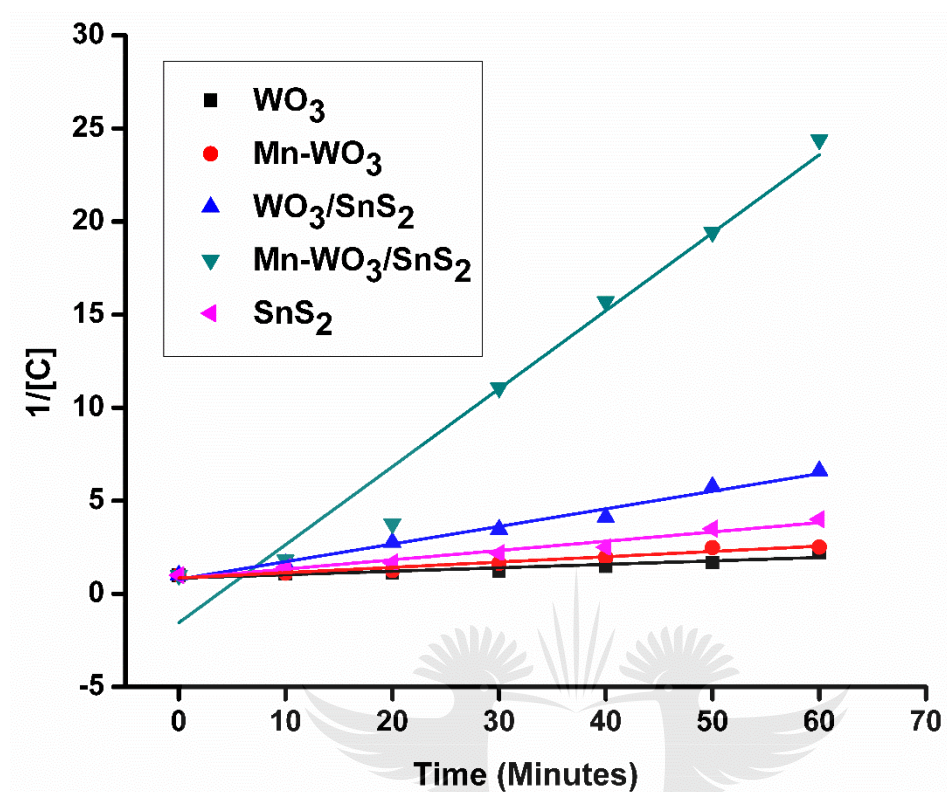
This graph shows the fitted second order kinetics graph for the nanoparticles.